First-Principles Investigation of Entropy-stabilized and Double Half-Heusler Alloys for Thermoelectric Applications

विद्या वाचस्पति की
उपाधि की अपेक्षाओं की आंशिक पूर्ति में प्रस्तुत शोध प्रबंध

A thesis submitted in partial fulfillment of the requirements of the degree of Doctor of Philosophy

द्वारा / By
राजीव रंजन / Rajeev Ranjan
पंजीकरण सं. / Registration No.: 20193703

शोध प्रबंध पर्यवेक्षक / Thesis Supervisor:
डा. प्रसेंजीत घोष / Dr. Prasenjit Ghosh

भारतीय विज्ञान शिक्षा एवं अनुसंधान संस्थान पुणे
INDIAN INSTITUTE OF SCIENCE EDUCATION AND RESEARCH PUNE

2026

In gratitude to my parents and brother, whose unwavering support and shared values reflect the timeless spirit of an Indian family - a heritage that shapes my every step.

CERTIFICATE

Certified that the work incorporated in the thesis entitled **"First-Principles Investigation of Entropy-stabilized and Double Half-Heusler Alloys for Thermoelectric Applications"** submitted by **Rajeev Ranjan** was carried out by the candidate, under my supervision. The work presented here or any part of it has not been included in any other thesis submitted previously for the award of any degree or diploma from any other university or institution.

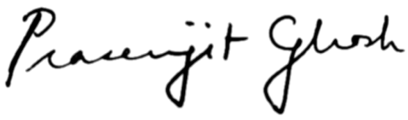

Date: 27-02-2026

(Dr. Prasenjit Ghosh)
Thesis Supervisor

Declaration

I declare that this written submission represents my ideas in my own words (sometimes paraphrased with online AI tools), and where others' ideas have been included, I have adequately cited and referenced the original sources. I also declare that I have adhered to all principles of academic honesty and integrity and have not misrepresented, fabricated or falsified any idea/data/fact/source in my submission. I understand that violation of the above will be cause for disciplinary action by the Institute and can also evoke penal action from the sources that have thus not been properly cited or from whom proper permission has not been taken when needed.

Date: 27-02-2026 (Rajeev Ranjan)

Acknowledgements

I am sincerely grateful to everyone who has supported and guided me during my doctoral journey. The completion of this thesis would not have been possible without the encouragement and contributions of many.

I would like to express my sincere gratitude to my Research Advisory Committee members, Prof. Mukul Kabir and Prof. Surjeet singh, for their insightful advice and constructive comments that significantly strengthened my research.

I am grateful to Dr. Gautam Sharma for all the research-related discussions. I would like to acknowledge my other labmates Dr. Aarti Shukla, Dr. Vineet Kumar Pandey, Dr. Aswathi Mohan, Dr. Unmesh Mondal, Sarika Lohkna, Pallavi Chame, Dr. Ankit Kumar, Prakash Khatri and Pankaj Gupta for (un)scientific discussions and being there with me in tough time. I extend my gratitude to my friends Subhash Ranjan Choudhary and Dr. Sudipta Roy for political and social discussions. I thank my childhood friend Anjani Srivastava for his never ending friendship. I thank my IISER Pune friends Dr. Deepak Kumar Roy, Ritam Pal, Dr. Dipanshu Garg, Dr. Jitendra Joshi, Aakash, and Mayank Sharma for making my time at IISER Pune enjoyable. I thank my cousins Medha Mayank, and Mausam Anand for all your support during the struggle time. I thank my lovely niece Sanaya Ranjan for all the love. I am extremely lucky to have you in my life.

I am grateful to Prof. Sunil S. Bhagwat, Prof. Jayant B. Udgaonkar and Dr. K. N. Ganesh, Director of IISER Pune, for providing an excellent research environment. I also thank the IISER Pune library for providing access to research journals and books.

I am thankful to IISER Pune for access to the computing facilities *Athena* and *Fermi*, and to the Centre for Development of Advanced Computing (C-DAC), Pune, for the use of *PARAM Utkarsh*. I gratefully acknowledge the National Supercomputing Mission (NSM) for providing access to the *PARAM Brahma* facility at IISER Pune, implemented by C-DAC and supported by the Ministry of Electronics and Information Technology (MeitY) and the Department of Science and Technology (DST), Government of India. I also acknowledge Center for Computational Materials Science, Institute for Materials Research, Tohoku University, Japan, for providing computational facilities through access to the Masamune-IMR Supercomputer. I express my sincere gratitude to IISER Pune for the fellowship. I thank Mr. Subhash Patankar for providing me with the Patankar Dissertation Fellowship in Physics at the last stage of my PhD.

I would like to acknowledge my wonderful brother, Kumud Ranjan Malviya, for his uncon-

ditional love, care, and constant support, being my backbone throughout my life from the very beginning. I could not have completed my PhD without his unwavering support in the background. I wish to convey my deepest gratitude to my beloved parents, Mrs. Ratna Ranjan and Mr. Arun Kumar Malviya, whose unwavering love, sacrifices, and constant support have shaped me into the person I am today. From the very beginning of my journey, they have been my pillars of strength, offering encouragement, guidance, and invaluable life lessons. Since my birth, they have sacrificed even the smallest luxuries and devoted their entire youth in shaping my future, ensuring not only my success in life but also my growth into a good human being.

Contents

List of Publications

List of publications resulting from work presented in this thesis

1. Rajeev Ranjan "Thermoelectric properties of Nb_2Co_2InSb and Nb_2Co_2GaSb double half-Heuslers", *manuscript under preparation*

2. Rajeev Ranjan "Entropy-stabilized ZrHfCoNiSnSb half-Heusler alloy for thermoelectric applications: a theoretical prediction", *Physical Chemistry Chemical Physics*, **2025**, 27, 15622-15634.

Synopsis

This thesis presents two projects centered on the computational design and analysis of thermoelectric materials derived from half-Heusler and double half-Heusler compounds. The research is motivated by the growing need to harvest waste heat from diverse sources such as automobile exhausts, industrial furnaces, and domestic heating systems through thermoelectric energy conversion. While half-Heusler alloys offer advantages including mechanical robustness, high-temperature stability, and favorable Seebeck coefficients, their performance is significantly hindered by inherently high lattice thermal conductivity, which limits overall thermoelectric efficiency. To address this limitation, the first project explores entropy stabilization (chapter 3), whereas the second investigates double half-Heusler engineering (chapter 4) as potential pathways for performance enhancement.

In chapter 1, the performance of thermoelectric devices is examined in detail. The chapter also includes a review of the literature on various classes of thermoelectric materials, highlighting their thermoelectric performance.

Major part of chapter 2 describes Density Functional Theory (DFT), a fundamental and widely adopted computational framework in contemporary materials science for addressing the many-electron problem. The discussion covers the theoretical underpinnings of DFT, outlining its formalism as well as the approximations typically applied in practical simulations. The chapter also talks about the Boltzmann transport theory, which forms the theoretical foundation for the analysis of electronic transport properties presented in this work. Finally, the Debye–Callaway model is described as a tool for estimating lattice thermal conductivity, offering insights into phonon-mediated heat transport.

In chapter 3, the mixed half-Heusler compound ZrHfCoNiSnSb is proposed and investigated through first-principles calculations. The study is motivated by the idea of combining two parent HH alloys to introduce mass disorder, thereby lowering lattice thermal conductivity while preserving favorable electronic transport characteristics. This chapter systematically examines the structural, electronic, thermodynamic, and transport properties of the mixed compound. The contribution of configurational entropy to stabilizing the

mixed phase at elevated temperatures is highlighted, and the thermoelectric performance of the proposed material is compared with that of its parent alloys.

In chapter 4, the thermoelectric properties of two quaternary double half-Heusler compounds, Nb_2Co_2InSb and Nb_2Co_2GaSb, are examined through theoretical calculations. These materials are designed by modifying the parent ternary half-Heusler NbCoSn, replacing Sn with In/Ga and Sb, with the goal of maintaining advantageous electronic characteristics while markedly lowering the lattice thermal conductivity (k_L) via mass disorder. The investigation considers multiple structural arrangements, including two ordered phases and two Special Quasi-random Structures (SQSs), and assesses their structural, dynamical, electronic, and thermoelectric properties. Findings reveal a pronounced decrease in k_L, nearly fivefold compared to NbCoSn, resulting in enhanced figures of merit (zT) reaching up to 2.0 at 1000 K. The study reveals that Nb_2Co_2GaSb achieves optimal performance in its ordered configuration, whereas Nb_2Co_2InSb attains superior thermoelectric efficiency in the disordered SQS phase.

The final summary and outlook chapter of this thesis presents a consolidated overview of the key findings and the broader significance of the research carried out on these thermoelectric materials. It recaps the principal outcomes achieved in the course of this work and provides a forward-looking view on potential future research directions aimed at advancing the field of thermoelectric materials.

List of symbols

ZT	Device figure of merit
zT	Material figure of merit
$\mathbf{M}$	Nuclear mass
$\mathbf{m}_e$	Electron mass
α	Seebeck coefficient
η	Efficiency of thermoelectric device
σ	Electrical conductivity
κ_e	Electronic part of thermal conductivity
$\mathbf{R}$	Nuclear coordinates
$\mathbf{r}$	Electronic coordinates
$n(\mathbf{r})$	Charge density
$V_{\text{ext}}(\mathbf{r})$	External potential
$T_s[n]$	Kinetic energy
$E_{\text{XC}}[n]$	Exchange correlation energy
$E_H[n]$	Hartree energy
$\mathbf{k}$	Wave vector
Ω	Volume of the unit cell
$\mathbf{G}$	Reciprocal lattice vector
$\mathbf{F}_I$	Force on the I^{th} atom
DFT	Density Functional Theory
$\sigma^s_{\alpha\beta}$	Stress tensor
ω	Phonon frequency
PBE	Perdew, Burke and Ernzerhof
T	Temperature
KS	Kohn-Sham
XC	Echange Correlation
LDA	Local density approximation

GGA	Generalized gradient approximation
μ	Chemical potential
DOS	Density of States
HF	Hartree-Fock
$f(T;\mu)$	Distribution function of electrons
$v_{\mathbf{k}}$	Group velocity of the electron
$\mathbf{E}$	Electric field
$\mathbf{J}_e$	Electronic current density
$\mathbf{J}_q$	Heat current density
$\varepsilon_{\mathbf{k}}$	Electronic eigenstate
τ_{av}	Average electronic relaxation time
Ξ	Deformation potential
C	Elastic constant
k_B	Boltzmann constant
Θ_D^i	Debye temperature of the i^{th} mode
τ_N^i	Relaxation time of the i^{th} mode for normal process
τ_i^U	Relaxation time of the i^{th} mode for Umklapp process
γ	Gruneissen parameter
k_L	Lattice thermal conductivity

List of Figures

List of Tables

Chapter 1

Introduction

A substantial amount of waste heat is produced in automotive exhaust systems, residential heating, and various industrial operations. One effective approach to harness this otherwise lost energy is through thermoelectricity, which enables the direct conversion of heat into electrical energy. Thermoelectricity refers to the phenomenon in which a temperature difference between two ends of a material, typically a metal or semiconductor, leads to the generation of electricity due to the material's intrinsic properties.
When one end of the material is heated while the other is kept cool, charge carriers (electrons or holes) migrate from the hot side to the cold side. This movement results in a buildup of positive charge at one end and negative charge at the other, thereby creating a potential difference across the material. Eventually, a balance is established between the diffusion-driven chemical potential and the opposing electrostatic force generated by the charge separation. This mechanism forms the basis of the thermoelectric effect responsible for power generation [3].
Thermoelectricity involves three key effects: the Seebeck effect, the Peltier effect, and the Thomson effect.

1.1 Seebeck effect

In 1821, Thomas Seebeck discovered that when a temperature gradient ΔT is applied across a metal or semiconductor, charge carriers move from the hot side to the cold side, leading to the development of a voltage difference ΔV across the material. This voltage is directly proportional to the temperature difference. The constant of proportionality, denoted by α, is known as the Seebeck coefficient [3, 8]. It depends on the material's microscopic properties, such as the density of states, Fermi level, bandgap, and carrier

concentration. This relationship is expressed as:

$$\Delta V = - \alpha \Delta T \tag{1.1}$$

1.2 Peltier effect

In 1834, Jean Peltier discovered a phenomenon opposite to the Seebeck effect. He observed that when an electric current flows through the junction of two different materials, heat is either absorbed or released at the junction. This effect is known as the *Peltier effect* [9]. The rate of heat transfer $\dot{Q}$ at the junction is directly proportional to the electric current I flowing through the material. Similar to the Seebeck coefficient, the proportionality constant depends on the material's microscopic characteristics and is called the *Peltier coefficient* Π. The relationship is given by:

$$\dot{Q} = \Pi I \tag{1.2}$$

A schematic diagram of the Seebeck and Peltier coefficients is shown in the Figure 1.1.

1.3 Thomson effect

In certain materials, the Seebeck coefficient is not constant but varies significantly with temperature. As a result, a temperature gradient in such materials also leads to a gradient in the Seebeck coefficient. When an electric current flows through these materials, this variation causes a continuous Peltier-like effect along the material. This phenomenon, discovered by William Thomson in 1851, is known as the *Thomson effect* [10]. The rate of heat generation per unit volume due to the Thomson effect, denoted by $\dot{q}$, is given by:

$$\dot{q} = - \mathscr{K} \mathbf{J} \cdot \nabla T \tag{1.3}$$

where $\mathscr{K}$ is Thomson coefficient, and $\mathbf{J}$ is the current density.

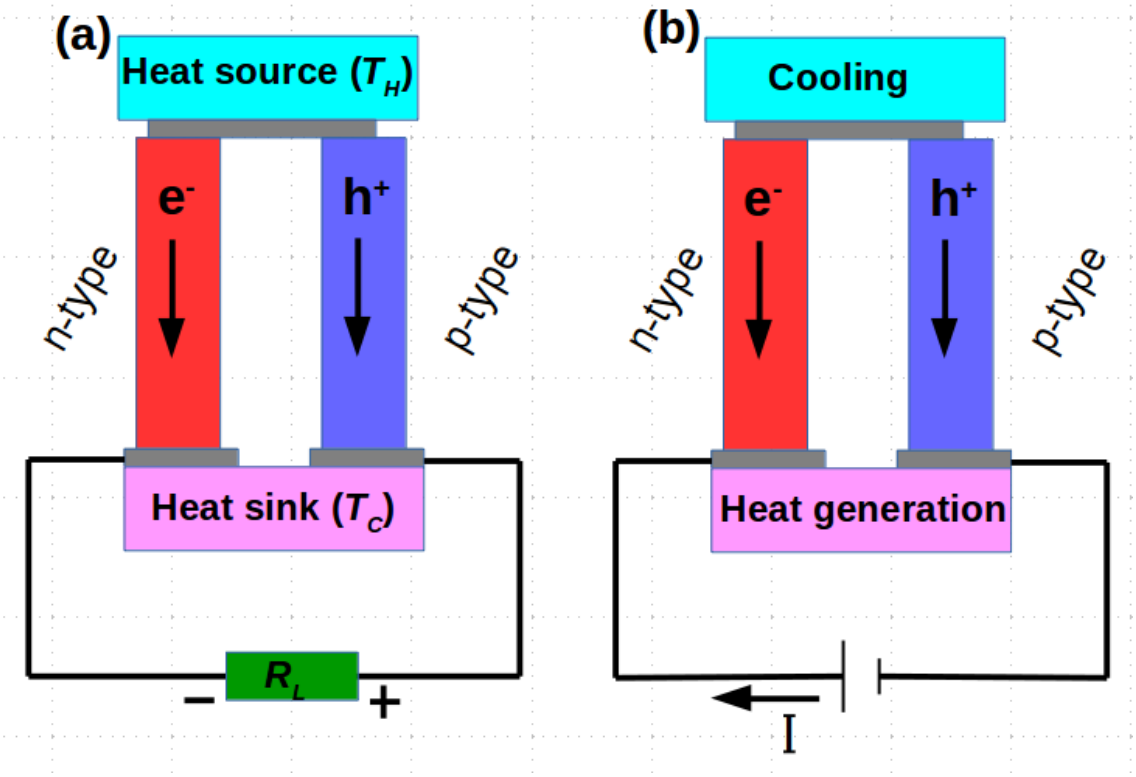

Figure 1.1: Diagram of thermocouple demonstrating (a)Seebeck effect (b) Peltier cooling [3]

1.4 Efficiency and figure of merit of a thermoelectric material [1]

When the two ends of a thermoelectric material are maintained at different temperatures, the charge carriers absorb energy from the hotter end and move towards the colder end. In a thermoelectric device comprising an n-type leg and a p-type leg, electrons(holes) in the n-type (p-type) segment flow from the hotter side to the colder side. This carrier motion establishes a potential difference across both legs: for the n-type leg, the hotter end attains a higher potential than the colder end, whereas for the p-type leg, the colder end attains a higher potential than the hotter end. The combined potential difference across the n-type and p-type legs can be used to generate electrical power, as illustrated in Figure 1.1. Similar to the Carnot engine, not all of the heat absorbed at the hotter end can be converted into electrical energy. The efficiency of a thermoelectric device is defined as the ratio of the electrical power delivered to the external circuit to the thermal energy absorbed at the hotter end.

Let the Seebeck coefficient, electrical resistance, and thermal conductivity of the p-type leg of a thermoelectric material be denoted by α_h, R_h, and κ_h, respectively. Similarly, let the corresponding values for the n-type leg be α_n, R_n, and κ_n, and the load resistance be R_L. The total Seebeck coefficient α, total thermal conductivity κ, and total resistance R of the thermoelectric module are then given by:

$$\alpha = \alpha_h + |\alpha_n|, \quad \kappa = \kappa_h + \kappa_n, \quad R = R_h + R_n + R_L \tag{1.4}$$

The potential difference ΔV generated across the junction due to the Seebeck effect, in terms of the temperature difference $\Delta T = T_H$ - T_C, is given by:

$$\Delta V = \text{ - } \alpha \Delta T \tag{1.5}$$

This potential difference drives a current $I = \frac{\Delta V}{R}$ through the circuit, resulting in power dissipation in the load resistance given by $w = I^2 R_L$. In steady-state operation, part of the heat drawn from the hot source is used to balance the Peltier cooling. Thus, the total heat absorbed from the source, Q_s, is given by [1]:

$$Q_s = \alpha I T_H + \kappa \nabla T \tag{1.6}$$

Therefore, the efficiency η of the thermoelectric device is given by [1]:

$$\eta = \frac{w}{Q_s} = \frac{I^2 R_L}{\alpha I T_H + \kappa \nabla T} \tag{1.7}$$

By optimizing the load resistance R_L, the maximum efficiency η_{max} can be achieved, which is expressed as:

$$\eta_{\text{max}} = \eta_{\text{Carnot}} \cdot \frac{\sqrt{ZT+1} \text{ - } 1}{\sqrt{ZT+1} + \frac{T_C}{T_H}} \tag{1.8}$$

Here, η_{Carnot} is the efficiency of a Carnot engine operating between T_H and T_C, and is given by:

$$\eta_{\text{Carnot}} = \frac{T_H \text{ - } T_C}{T_H} \tag{1.9}$$

The dimensionless figure of merit ZT, evaluated at the average temperature $T = \frac{T_H + T_C}{2}$, is defined as:

$$ZT = \frac{\alpha^2 \sigma}{\kappa} T, \quad \sigma = \frac{\sigma_h \sigma_n}{\sigma_h + \sigma_n} \tag{1.10}$$

where σ_h and σ_n are the electrical conductivities of the p-type and n-type legs, respectively. A plot of $\eta_{\max}$ as a function of ZT for a thermoelectric device operating between 900 K and 300 K is shown in the Figure 1.2:

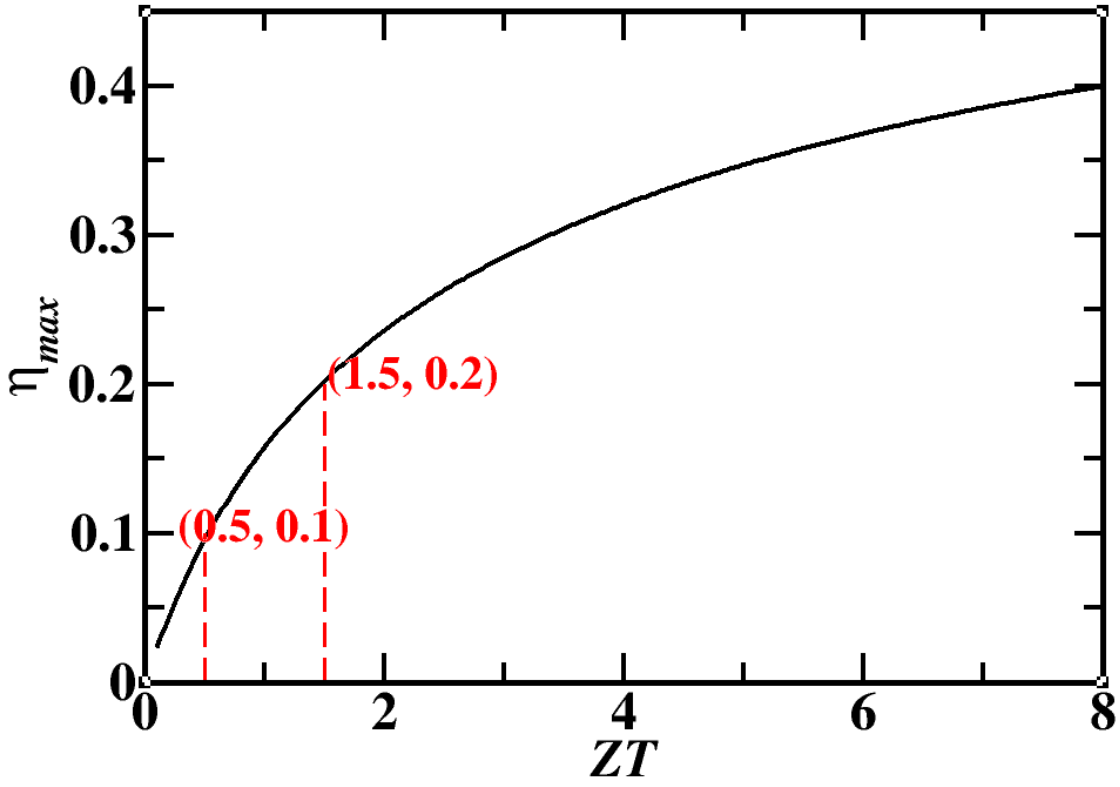

Figure 1.2: Maximum efficiency as a function of ZT for $T_H = 900$ K and $T_C = 300$ K

As shown in the above plot 1.2, even high-performance thermoelectric materials with $ZT = 1$ achieve only about 15% efficiency when operating between 900 K and 300 K. This is significantly lower than the efficiency of a Carnot engine working over the same temperature range ($\eta_{carnot} = 0.66$ for a carnot engine working between the same temperatures). Therefore, much of the research in thermoelectricity focuses on discovering materials with a high figure of merit ZT that can operate efficiently at elevated temperatures.

1.5 Key Parameters Influencing Thermoelectric Performance

As illustrated in Figure 1.2, achieving high thermoelectric efficiency requires a large figure of merit. According to Equation 1.10, a high ZT can be obtained by simultaneously

maximizing the Seebeck coefficient α, maximizing the electrical conductivity σ, and minimizing the thermal conductivity κ. However, these thermoelectric transport coefficients are interdependent and often exhibit competing behavior due to their common origin in the electronic structure of materials. This trade-off can be understood using simplified expressions for degenerate semiconductors or metals. In such systems, the Seebeck coefficient and electrical conductivity can be expressed in terms of the Boltzmann constant k_B, density-of-states effective mass m_d, band effective mass m_b, temperature T, Planck's constant h, and carrier concentration n, as follows [11]:

$$\alpha = \frac{8\pi^2 k_B^2}{3eh^2} m_d T \left(\frac{\pi}{3n}\right)^{2/3} \tag{1.11}$$

$$\sigma = ne\mu = \frac{ne^2\tau}{m_b} \tag{1.12}$$

Here, μ is the carrier mobility, and τ is the relaxation time. From these expressions, it is clear that the Seebeck coefficient α is inversely related to carrier concentration n, whereas electrical conductivity σ is directly proportional to n. Therefore, increasing the carrier concentration enhances σ but reduces α, as illustrated in Figure 1.3. To maximize the power factor $\alpha^2\sigma$, an optimal value of carrier concentration must be chosen. Additionally, the electronic contribution to thermal conductivity κ_e increases with carrier concentration, as described by the Wiedemann–Franz law [12]:

$$\kappa_e = L\sigma T = Lne\mu T \tag{1.13}$$

where L is the Lorenz number. Since κ_e also rises with increasing n, the optimal carrier concentration for maximizing ZT differs from that for maximizing the power factor. This is also shown in Figure 1.3. Likewise, increasing the effective mass enhances the Seebeck coefficient but reduces both electrical conductivity and κ_e. Therefore, achieving a high ZT requires careful tuning of the electronic properties to balance these interdependent factors.

Similar to electronic thermal conductivity, lattice thermal conductivity, κ_{L}, represents the component of a material's total thermal conductivity that arises from the transport of heat via quantized lattice vibrations, or phonons. It is governed by the phonon spectrum, group velocity, and scattering mechanisms such as phonon-phonon interactions, phonon-impurity scattering, and phonon-boundary scattering.

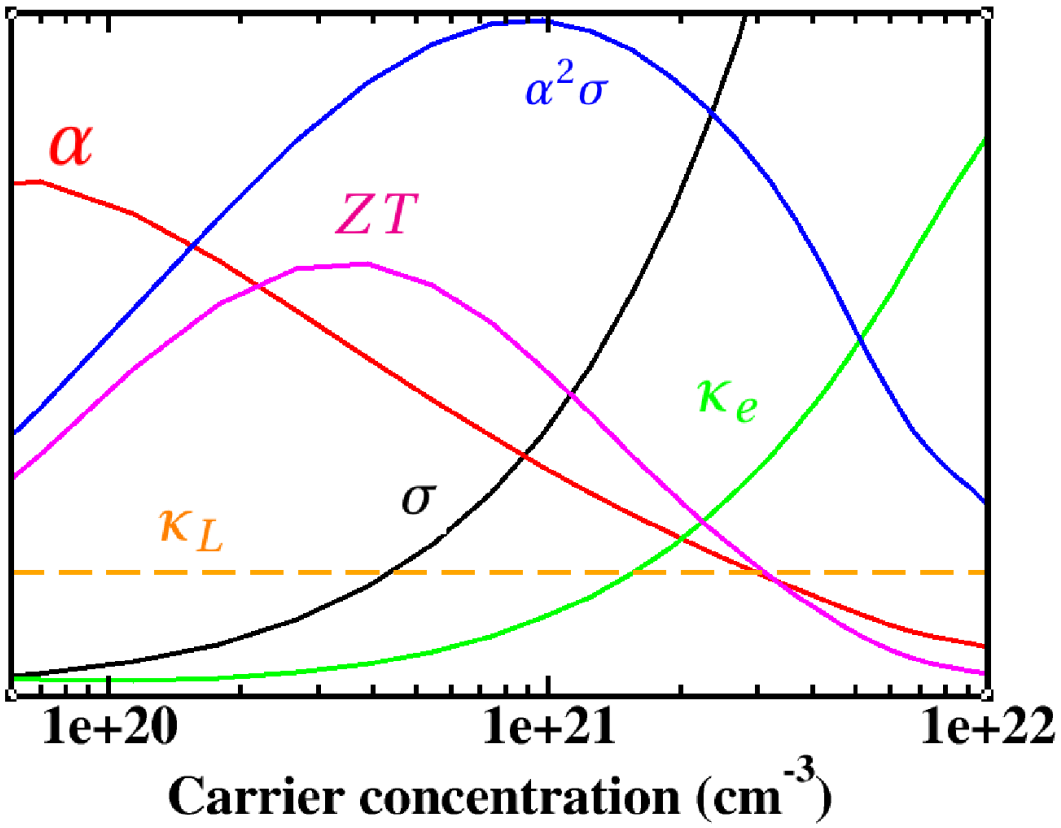

Figure 1.3: Schematic representation of the variation of thermoelectric transport properties as a function of carrier concentration. [3]

1.6 Types of thermoelectric materials

There are many classes of thermoelectric materials. In this section, I describe a few of them.

1.6.1 Skutterudites

Skutterudites are a class of thermoelectric materials with a cubic crystal structure belonging to the space group $Im\bar{3}$, and each unit cell contains 32 atoms [13]. The structure consists of eight sub-cubes of transition metals Co, Rh, or Ir, which occupy the Wyckoff position 8c $(0.25, 0.25, 0.25)$. Out of these eight sub-cubes, six are filled with square-planar rings formed by pnictogen atoms (P, As, or Sb), while the remaining two contain voids that can

accommodate smaller atoms [13].

These materials are generally represented by the formula $\square_2T_8Pn_{32}$, where $\square$ denotes the voids that can be filled with rare-earth or alkaline-earth elements, T represents the transition metals (Co, Rh, or Ir), and Pn refers to the pnictogen atoms [13]. Skutterudites are known for their high Seebeck coefficients; however, they also possess high lattice thermal conductivity, which limits their thermoelectric performance by reducing the figure of merit zT. For instance, $CoSb_3$ exhibits a high Seebeck coefficient of about $200\ \mu V\ K^{-1}$, but its lattice thermal conductivity of $8.9\ Wm^{-1}K^{-1}$ at 300 K [14] results in a low figure of merit of only 0.17 at 610 K [15].

To overcome this limitation, the voids in $CoSb_3$ can be partially filled with rare-earth elements, which act as "rattlers" and effectively scatter low-frequency phonons. This reduces lattice thermal conductivity and improves thermoelectric performance. For example, $Yb_{0.4}Co_8Sb_{24.6}$ achieves a high zT value of 1.26 at 800 K due to its reduced lattice thermal conductivity of $1.8\ Wm^{-1}K^{-1}$ at 300 K, attributed to strong scattering of acoustic phonons by Yb atoms [16, 17]. Similarly, doping with alkali metals (Na, K, or Li) [18–20], and alkaline-earth metals (Ba, Ca, or Sr) [21–23] has also led to significantly enhanced zT values.

1.6.2 Chalcogenides

Chalcogenides are effective thermoelectric materials for low (below 500 K) and mid-temperature (500–900 K) applications. Common examples include SnSe, SnTe, Cu_2Se, Cu_2S, Ag_2Te, and Bi_2Te_3. These compounds generally follow the formula M_xC_y, where M represents a metal and C denotes a chalcogen element (S, Se, or Te). In particular, mid-temperature chalcogenides, especially those based on lead and tin, have emerged as state-of-the-art thermoelectric materials. This is largely due to their favourable electronic structures and intrinsic ability to suppress lattice thermal conductivity. Lead chalcogenides such as PbTe, PbSe, and PbS, which crystallize in the rocksalt structure, demonstrate excellent thermoelectric performance in the 600 to 800 K range. Among them, PbTe has exhibited outstanding figure of merit values (zT), reaching 1.4 for both p- and n-type carriers [24, 25], and as high as 2.2 at 915 K when lattice thermal conductivity is effectively reduced [26].

Various doping strategies (e.g., with Na, Sn, I, Ti, or Bi) have been employed to enhance carrier concentration, increase the Seebeck coefficient, and boost phonon scattering [27]. These approaches have led to significant zT improvements: up to 2 in PbSe [28] , 1.5 in

doped PbTe [24, 29], and 0.89 in Bi-doped PbS [30].

1.6.3 Half-Heusler

Half-Heusler (HH) alloys, typically described by the chemical formula XYZ, where X and Y are transition metals and Z is a p-block element, crystallize in the space group $F\bar{4}3m$. Their structure comprises three interpenetrating sublattices formed by X, Y, and Z atoms. Among them, valence electron count (VEC) 18 HH compounds exhibit remarkable thermal stability at elevated temperatures, making them excellent candidates for high-temperature thermoelectric applications. These materials exhibit Seebeck coefficients comparable to leading chalcogenides; however, a major limitation is their inherently high lattice thermal conductivity, which suppresses the overall thermoelectric figure of merit (zT).

For instance, well-known HH compounds like ZrNiSn and HfNiSn show Seebeck coefficients of approximately 490 μV K^{-1} and 450 μV K^{-1} at 300 K, respectively, at a carrier concentration of 10^{19} cm^{-3} (n-type). This is much higher than n-type PbTe for which the Seebeck coefficient is 110 μV K^{-1} at 300 K for the same value of the carrier concentration [24]. Despite their high Seebeck coefficient, high lattice thermal conductivity of approximately 15 Wm^{-1}K^{-1} at room temperature limits their thermoelectric performance, resulting in a low zT of around 0.04 [6].

Despite this challenge, several HH alloys have demonstrated promising thermoelectric performance, with zT values approaching or exceeding unity. Notably, p-type compositions such as FeNb$_{1-x}$Ti$_x$Sb and TaFeSb-based systems have achieved zT values of approximately 1.1 at 1100 K and 1.52 at 973 K, respectively [31, 32]. Likewise, n-type materials like Nb$_{0.83}$CoSb have exhibited peak zT values of around 0.9 at 1123 K [33].

One effective strategy to mitigate the high lattice thermal conductivity in HH materials is to introduce mass disorder at a specific lattice site by partially substituting one of the X, Y, or Z atoms with neighbouring elements. This leads to the formation of quaternary or "double" half-Heusler compounds, which are combinations of VEC 17 and VEC 19 HH phases that retain the average VEC of 18. For example, replacing the Y atom in a ternary XYZ compound with two different atoms, Y′ and Y″, results in a double HH structure of the form X$_2$Y′Y″Z$_2$.

Anand *et al.* [34] reported that the lattice thermal conductivity of Ti$_2$FeNiSb$_2$ (a double HH) is significantly reduced to 7.5 Wm^{-1}K^{-1}, compared to 25 Wm^{-1}K^{-1} for the parent ternary compound TiCoSb. Another approach to reduce lattice thermal conductivity is through high-entropy engineering in HH systems as explained in section 1.6.2. Recently,

Chen *et al.* [35] demonstrated ultralow lattice thermal conductivity in high-entropy MCoSb compounds, where M is an equimolar mixture of Ti, Zr, Hf, V, Nb, and Ta. This system showed a thermal conductivity as low as 1.8 $Wm^{-1}K^{-1}$ at room temperature. The stability of the MCoSb compound arises from the contribution of configurational entropy to the total Gibbs free energy. Similarly, in the first part of my thesis, I propose a mixed high-entropy alloy, ZrHfCoNiSnSb, which is an equimolar combination of four stable half-Heusler compounds: ZrNiSn, HfCoSb, HfNiSn, and ZrCoSb. In this alloy, the enhanced stability relative to its parent half-Heusler systems also originates from the configurational entropy contribution to the Gibbs free energy. Like MCoSb, there are significant mass variations in this mixed half-Heusler system, leading to reduced lattice thermal conductivity of 5.40 $Wm^{-1}K^{-1}$ at room temperature.

1.7 Strategies to improve zT

From Equation 1.10, it is clear that achieving a high thermoelectric figure of merit, zT, requires both a high power factor, $\alpha^2\sigma$, and a low lattice thermal conductivity. While the power factor is primarily governed by the electronic structure of the material, the lattice thermal conductivity is determined by phonon dynamics. As a result, strategies for improving the power factor and reducing lattice thermal conductivity are largely independent of each other.

In the following sections, we briefly outline two such approaches: (1) band engineering to enhance the power factor, and (2) entropy engineering and aliovalent substitution to lower the lattice thermal conductivity. These techniques have been employed in this thesis to improve the overall thermoelectric performance.

1.7.1 Band engineering

Band engineering primarily refers to the deliberate modification of the electronic band structure through doping, elemental substitution, or alloying. This technique aims to shift the bands near the valence band maximum (VBM) or conduction band minimum (CBM) closer to their respective band edges, often leading to the formation of additional energy valleys [36]. The presence of these extra valleys increases the density-of-states effective mass, which in turn enhances the Seebeck coefficient. As a result, the power factor—and consequently the thermoelectric figure of merit—can be significantly improved.

1.7.2 Entropy engineering and aliovalent substitution

In recent years, entropy engineering has emerged as an effective strategy for reducing lattice thermal conductivity while preserving the power factor. This approach relies on stabilizing a single-phase crystal structure at elevated temperatures by lowering the Gibbs free energy through an increase in configurational entropy (ΔS_{conf}). This is achieved by substituting multiple elements at the same Wyckoff position, ensuring that the configurational entropy exceeds $1.5R$, where R is the universal gas constant. The high entropy promotes the formation of a stable, single-phase crystal.

The presence of a single-phase structure weakens electron scattering at phase boundaries, thereby maintaining favorable electronic transport properties. Simultaneously, the mass and atomic size mismatch among substituted atoms causes significant lattice distortion and mass fluctuations, which enhance phonon scattering and thus reduce the lattice thermal conductivity [36].

Additional phonon scattering can also be introduced through aliovalent substitution, such as in double half-Heusler systems discussed earlier. This type of substitution decreases the group velocity of acoustic phonons, leading to the softening of these modes and reduced heat transport. Moreover, the mass disorder introduced at aliovalently substituted sites increases anharmonicity, further promoting phonon scattering and contributing to a lower lattice thermal conductivity.

1.7.3 Phonon engineering

In the last few years, phonon engineering has emerged as a powerful and complementary strategy to band engineering for enhancing the thermoelectric performance of half-Heusler and related compounds. Phonon engineering specifically targets the reduction of lattice thermal conductivity (κ_{L}), which is a major component of the total thermal conductivity and a key factor limiting the figure of merit, ZT. Unlike electronic optimization strategies that focus on optimizing carrier concentration and band convergence, phonon engineering seeks to disrupt the efficient propagation of heat-carrying phonons through enhanced scattering mechanisms without significantly degrading the electronic transport properties. In complex multi-component systems such as mixed half-Heuslers and double half-Heuslers, a variety of intrinsic phonon-scattering mechanisms can be activated. The introduction of atoms with large mass contrast and disparate force constants in the crystal lattice leads to strong

point-defect scattering, which is particularly effective at scattering high-frequency phonons. Additionally, strain-field fluctuations arising from size mismatch between constituent atoms further enhance phonon scattering. The structural complexity inherent in double half-Heuslers, characterized by larger unit cells and a greater number of optical phonon branches, promotes increased acoustic–optical phonon scattering, thereby reducing the group velocity of acoustic phonons that contribute most to heat transport. Moreover, alloying and site disorder in mixed half-Heuslers introduce configurational complexity that can give rise to resonant phonon scattering and flattening of phonon dispersion curves, which both act to shorten phonon lifetimes.

An important strategy in phonon engineering for improving thermoelectric performance is the phonon-glass electron-crystal (PGEC) concept. This idea describes an ideal thermoelectric material in which phonons exhibit glass-like transport while electrons retain crystal-like mobility. In such systems, strong phonon scattering suppresses the lattice thermal conductivity, whereas charge carriers can still move efficiently through the periodic lattice. As a result, the thermoelectric figure of merit can be enhanced by reducing heat transport without significantly affecting electrical conductivity. Materials such as Na_xCoO_2 and $Ca_xYb_{1-x}Zn_2Sb_2$ provide examples of this behavior, where ordered layers are separated by disordered cation monolayers, giving rise to PGEC characteristics [3].

Grain boundary scattering and interface effects in nanostructured or multiphase samples can also play a significant role at length scales comparable to phonon mean free paths, further suppressing κ_L. Studies on Bi_2Te_3–Sb_2Te_3 and PbTe–PbSe thin films have demonstrated that enhanced phonon scattering can significantly suppress lattice thermal conductivity, reducing it to values close to 0.5 $Wm^{-1}K^{-1}$ at room temperature [37–39].

Therefore, integrating phonon engineering into the design of mixed and double half-Heusler thermoelectrics provides a systematic route to minimize lattice thermal conductivity through controlled disorder, mass fluctuation, and structural complexity, complementing existing strategies that primarily enhance the electronic contribution to thermoelectric performance.

1.8 Thesis outline

The rest of the thesis is structured as follows:

In Chapter 2, Density Functional Theory (DFT) is introduced as a basic and widely

used computational method in modern materials science that helps to solve the complex problem of many interacting electrons. The chapter discusses the theoretical foundations of DFT, including its formal structure and the approximations commonly employed in practical calculations. In addition, the chapter provides an overview of the Boltzmann transport theory, which serves as the basis for evaluating the electronic transport properties explored in this thesis. The chapter also explains the Debye-Callaway model, which is used to calculate lattice thermal conductivity, and shows how it helps in understanding heat transport through phonons. Together, these theoretical tools provide the foundation for the methods and results discussed in the later chapters.

In Chapter 3, a new mixed half-Heusler compound, ZrHfCoNiSnSb, is proposed and studied using first-principles calculations. This chapter presents the motivation behind designing the compound by mixing two parent HH alloys to reduce lattice thermal conductivity through mass disorder while maintaining desirable electronic transport properties. The structural, electronic, thermodynamic, and transport properties of the mixed compound are systematically analyzed. The role of configurational entropy in stabilizing the mixed phase at high temperatures is discussed, and the thermoelectric performance of the proposed compound is compared with that of its parent materials.

In Chapter 4, a theoretical investigation of the thermoelectric performance of two quaternary double half-Heusler compounds, Nb_2Co_2InSb and Nb_2Co_2GaSb, is presented. These systems are derived from the parent ternary half-Heusler NbCoSn by replacing Sn with In/Ga and Sb, aiming to retain favorable electronic properties while significantly reducing lattice thermal conductivity (k_L) through mass disorder. The study explores multiple structural phases, including two ordered configurations and two Special Quasi-random Structures (SQSs), and analyzes their structural, dynamical, electronic, and thermoelectric properties. The results indicate a substantial reduction in k_L, nearly five times lower than NbCoSn, which leads to enhanced figures of merit (zT), with values up to 2.0 at 1000 K. The chapter highlights how the interplay between atomic disorder and structural ordering influences transport behavior, showing that Nb_2Co_2GaSb performs best in its ordered form, while Nb_2Co_2InSb shows superior thermoelectric efficiency in the disordered SQS phase.

Chapter 2

Theoretical methods

The fundamental properties of any material, such as its electronic, magnetic, optical, or structural characteristics, are governed by the behaviour of its electrons and nuclei. In theory, one can determine these properties accurately by solving the many-body Schrödinger equation, which describes how a system of interacting particles evolves and behaves at the quantum level. However, this equation becomes highly complicated when applied to systems containing more than a few particles, due to the exponential increase in computational cost with the number of electrons involved. As a result, solving the full many-body Schrödinger equation for real, complex materials is not feasible using exact methods. This challenge has led scientists to develop various approximate methods that can capture the essential physics without requiring impractical computational resources. One of the most successful and widely used approaches developed for this purpose is Density Functional Theory (DFT). Instead of working with the complicated many-body wavefunction, DFT reformulates the problem in terms of the electron density-a much simpler quantity that depends only on three spatial dimensions. Through this reformulation and the use of carefully designed approximations for electron exchange and correlation effects, DFT provides a practical and powerful framework for a wide range of material properties from first principles, i.e., without relying on empirical data. This chapter introduces DFT as a key tool in modern computational materials science and outlines how it addresses the central challenges posed by the many-body problem. Additionally, this thesis encompasses the calculation of electronic transport properties, for which a brief overview of Boltzmann transport theory is provided. It also includes the evaluation of lattice thermal conductivity, employing the Debye-Callaway model, which is briefly discussed to support the methodology used.

2.1 Many body Schrödinger equation

A material system at the microscopic level consists of N nuclei, which are positively charged, and n electrons, which carry a negative charge. These particles interact with one another through long-range Coulomb forces. The complete quantum mechanical description of such a system is governed by the time-independent Schrödinger equation (TISE), which takes the following form [40]:

$$\hat{H}_{\text{tot}}\,\Psi(\{\mathbf{R}_I\},\{\mathbf{r}_i\}) = E_{\text{tot}}\,\Psi(\{\mathbf{R}_I\},\{\mathbf{r}_i\}), \tag{2.1}$$

Here, $\Psi(\{\mathbf{R}_I\},\{\mathbf{r}_i\})$ represents the many-body wavefunction, which is a function of the spatial coordinates of all the nuclei $\{\mathbf{R}_I\}$ and all the electrons $\{\mathbf{r}_i\}$ present in the system. The quantity E_{tot} denotes the total energy eigenvalue associated with the system. The operator $\hat{H}_{\text{tot}}$ is the total Hamiltonian, encompassing both the kinetic energy of the particles and the potential energy contributions resulting from all mutual interactions among them. The explicit expression for the Hamiltonian is given by:

$$\begin{aligned}\hat{H}_{\text{tot}} = &-\sum_{I=1}^{N}\frac{\hbar^2}{2\mathbf{M}_I}\nabla_I^2 - \sum_{i=1}^{n}\frac{\hbar^2}{2\mathbf{m}_e}\nabla_i^2 \\ &+\frac{1}{2}\sum_{\substack{I,J=1\\I\neq J}}^{N}\frac{z_I z_J e^2}{4\pi\epsilon_0|\mathbf{R}_I - \mathbf{R}_J|} + \frac{1}{2}\sum_{\substack{i,j=1\\i\neq j}}^{n}\frac{e^2}{4\pi\epsilon_0|\mathbf{r}_i - \mathbf{r}_j|} \\ &-\sum_{I=1}^{N}\sum_{i=1}^{n}\frac{z_I e^2}{4\pi\epsilon_0|\mathbf{R}_I - \mathbf{r}_i|},\end{aligned} \tag{2.2}$$

Here, z_I and $\mathbf{M}_I$ represent the atomic number and the mass of the I-th nucleus, respectively. The symbol $\mathbf{m}_e$ denotes the mass of an electron, while $\hbar$ stands for the reduced Planck constant. The quantity e refers to the elementary charge, and ϵ_0 corresponds to the vacuum permittivity.

The terms in the above Hamiltonian correspond to different physical contributions. The first term describes the kinetic energy associated with the motion of all nuclei, while the second term accounts for the kinetic energy of the electrons. The third term reflects the repulsive Coulomb interaction between all distinct pairs of nuclei. In contrast, the fourth term represents the repulsive interactions among electrons. Finally, the fifth term captures the attractive Coulomb interaction between the nuclei and electrons.

In theory, solving this many-body Schrödinger equation would yield complete information about the ground state and excited states of the material system. However, the equation poses significant computational challenges. The core difficulty arises from the nature of the Coulomb interactions, particularly the electron-electron term, which entangles the motion of every electron with every other.

As the number of particles in a quantum system increases, the associated wavefunction must account for the positions and spins of all particles simultaneously. This leads to a wavefunction that exists in a high-dimensional space-specifically, a 3N-dimensional space for N particles (since each particle has three spatial coordinates). Consequently, the computational resources required to store and manipulate this wavefunction increase exponentially with the number of particles. To address these challenges, it becomes necessary to employ well-founded approximations.

2.2 Adiabatic or Born-Oppenheimer Approximation

Solving the full Schrödinger equation for all nuclei and electrons is computationally impractical due to complex interactions and high dimensionality. A powerful and widely used simplification arises from recognizing the vast difference in mass between nuclei and electrons. The mass of a typical nucleus is several thousand times larger than that of an electron. For instance, the mass ratio between a proton and an electron is approximately

$$\frac{m_{\text{proton}}}{m_{\text{electron}}} \approx 1836.$$

Due to this mass difference, nuclei move much slowly compared to the rapidly moving electrons. Consequently, the characteristic timescales associated with their motions differ significantly:

$$t_{\text{nuclei}} \gg t_{\text{electrons}}.$$

This implies that during the short timescale over which electrons adjust their configuration, the nuclei appear essentially stationary. Thus, to a good approximation, electrons can be considered to move in the static potential field created by fixed nuclei. This separation of timescales forms the foundation of the **Born-Oppenheimer (BO) approximation**, and **adiabatic approximation** [41, 42]. Under the BO approximation, the total many-body wavefunction $\Psi(\{\mathbf{R}_I\}, \{\mathbf{r}_i\})$, which depends on both nuclear coordinates $\{\mathbf{R}_I\}$ and electronic coordinates $\{\mathbf{r}_i\}$, can be factorized into a product of nuclear and electronic

wavefunctions:

$$\Psi(\{\mathbf{R}_I\},\{\mathbf{r}_i\}) = \sum_n \Phi_n(\{\mathbf{R}_I\})\,\psi_n(\{\mathbf{R}_I\};\{\mathbf{r}_i\}), \tag{2.3}$$

where:

- $\Phi_n(\{\mathbf{R}_I\})$ is the nuclear wavefunction associated with the n-th vibrational/rotational state,
- $\psi_n(\{\mathbf{R}_I\};\{\mathbf{r}_i\})$ is the electronic wavefunction, which depends explicitly on the electronic coordinates and parametrically on the nuclear coordinates.

Under the adiabatic approximation, all electrons initially in the ground state remain in the instantaneous ground state of the Hamiltonian, even as it changes slowly due to nuclear vibrations. For a fixed configuration of nuclei (i.e., a fixed set of nuclear positions $\{\mathbf{R}_I\}$), the electrons experience a static potential, and their motion is governed by the electronic Hamiltonian. The corresponding electronic Schrödinger equation is given by:

$$\begin{aligned}\Bigg[-\sum_{i=1}^{n}\frac{\hbar^2}{2\mathbf{m}_e}\nabla_i^2 + \frac{1}{2}\sum_{\substack{i,j=1\\ i\neq j}}^{n}\frac{e^2}{4\pi\epsilon_0|\mathbf{r}_i - \mathbf{r}_j|} - \sum_{I=1}^{N}\sum_{i=1}^{n}\frac{z_I e^2}{4\pi\epsilon_0|\mathbf{R}_I - \mathbf{r}_i|} \\ +\frac{1}{2}\sum_{\substack{I,J=1\\ I\neq J}}^{N}\frac{z_I z_J e^2}{4\pi\epsilon_0|\mathbf{R}_I - \mathbf{R}_J|}\Bigg]\psi_n(\{\mathbf{R}_I\};\{\mathbf{r}_i\}) = E^n_{\text{ele}}(\{\mathbf{R}_I\})\,\psi_n(\{\mathbf{R}_I\};\{\mathbf{r}_i\}).\end{aligned} \tag{2.4}$$

In the above equation, the first term denotes the kinetic energy of electrons, the second term represents the electron-electron Coulomb repulsion, the third term describes the attractive interaction between electrons and nuclei, and the fourth term accounts for the repulsive nucleus-nucleus interaction, which remains constant for a fixed nuclear configuration.

It is important to note that in this approach, the nuclei are treated as stationary classical point charges, and their motion is ignored while solving the electronic problem. The electronic energy $E^n_{\text{ele}}(\{\mathbf{R}_I\})$ then acts as an effective potential energy surface on which the nuclei move in the next stage of the approximation. Despite the simplification by the BO approximation, the resulting electronic Schrödinger equation remains a many-body problem due to the presence of the electron-electron interaction term, which is inherently non-local and two-body in nature. As a result, exact analytic solutions are still not feasible

for systems with more than a few electrons. Therefore, additional approximations such as the Hartree-Fock method or Density Functional Theory (DFT) are employed to obtain practical solutions.

2.3 Density Functional Theory

Density Functional Theory (DFT) offers an alternative formulation of quantum many-body theory that simplifies the analysis of interacting electron systems by using the electron density $n(\mathbf{r})$ as the fundamental variable, instead of the many-body wavefunction $\Psi(\mathbf{r}_1, \mathbf{r}_2, \ldots, \mathbf{r}_n)$. This approach was pioneered by Pierre Hohenberg and Walter Kohn in 1964 and has since become the cornerstone of modern electronic structure theory. The fundamental principle of DFT is that the ground-state properties of a many-electron system are uniquely determined by its ground-state electron density, allowing for a significant simplification of the original many-body problem. In conventional many-body theory, the wavefunction depends on $3n$ spatial coordinates for a system of n electrons, making the direct solution computationally prohibitive for large n. In contrast, DFT relies solely on the electron density $n(\mathbf{r})$, which depends on just three spatial variables, independent of the number of electrons. This reduction in dimensionality is what makes DFT both efficient and widely applicable. DFT is applicable to systems composed of n interacting electrons subject to an external potential $V_{\text{ext}}(\mathbf{r})$, which typically originates from fixed nuclei in molecular or solid-state environments.

2.3.1 Hamiltonian in Atomic Units

The Hamiltonian for such a system, using Hartree atomic units ($\hbar = m_e = e = 4\pi\epsilon_0 = 1$), is given by:

$$\hat{H}_{\text{int}} = \text{-} \sum_{i=1}^{n} \frac{\nabla_i^2}{2} + \sum_{i=1}^{n} V_{\text{ext}}(\mathbf{r}_i) + \frac{1}{2} \sum_{\substack{i,j=1 \\ i \neq j}}^{n} \frac{1}{|\mathbf{r}_i \text{ - } \mathbf{r}_j|}, \tag{2.5}$$

where the first term corresponds to the total kinetic energy of the electrons, the second term describes the interaction of the electrons with the external potential applied to the system, and the third term captures the Coulomb repulsion arising from electron-electron interactions.

2.3.2 Hohenberg-Kohn Theorems

The fundamental basis of density functional theory (DFT) rests on two essential theorems formulated by Hohenberg and Kohn.

Theorem 1 (Existence Theorem):

"For a system of interacting particles in an external potential $V_{\text{ext}}(\mathbf{r})$, the potential $V_{\text{ext}}(\mathbf{r})$ is determined uniquely, except for a constant, by the ground state particle density $n_0(\mathbf{r})$" [43]. That is,

$$n_0(\mathbf{r}) \longrightarrow V_{\text{ext}}(\mathbf{r}) + \text{const.} \tag{2.6}$$

Implication: This theorem implies that all ground-state properties of the system, including the many-body wavefunction, the energy, and any observable, are unique functionals of the electron density $n_0(\mathbf{r})$.Therefore, the ground-state electron density alone encodes all the necessary information to fully characterize the system in its lowest energy state.

Theorem 2 (Variational Principle):

"A universal functional for the energy $E[n]$ in terms of the density $n(\mathbf{r})$ can be defined, valid for any external potential $V_{\text{ext}}(\mathbf{r})$. For any particular $V_{\text{ext}}(\mathbf{r})$, the exact ground state energy of the system is the global minimum value of this functional, and the density $n(\mathbf{r})$ that minimizes the functional is the exact ground state density $n_0(\mathbf{r})$" [43, 44]. That is,

$$E_0 = \min_n E[n], \quad \text{where} \quad E[n] = F_{\text{HK}}[n] + \int V_{\text{ext}}(\mathbf{r}) n(\mathbf{r})\, d\mathbf{r}. \tag{2.7}$$

The functional $F_{\text{HK}}[n]$ is universal in nature, meaning it does not depend on the external potential V_{ext}. It comprises two key contributions: the kinetic energy of the interacting electrons, $T[n]$, and the electron-electron interaction energy, $E_{\text{ee}}[n]$. These components together define the functional as

$$F_{\text{HK}}[n] = T[n] + E_{\text{ee}}[n]. \tag{2.8}$$

According to the second Hohenberg-Kohn theorem, this formulation provides a variational principle that enables the determination of the ground-state electron density by minimizing the total energy functional $E[n]$. The density that yields the minimum of this functional corresponds to the exact ground-state density, and the corresponding energy is the exact

ground-state energy of the system.

Together, the two Hohenberg-Kohn theorems assert that:

1. The ground-state electron density $n_0(\mathbf{r})$ uniquely determines all properties of a many-body system.

2. There exists a universal functional $F_{\text{HK}}[n]$, which, when added to the external potential energy term, gives a total energy functional $E[n]$ whose minimum yields the ground-state properties.

However, while the existence of $F_{\text{HK}}[n]$ is guaranteed, the theorems do not provide a method to construct this functional explicitly. In practice, therefore, further approximations are needed to evaluate $F_{\text{HK}}[n]$ reliably. A practical and widely used solution was proposed by Kohn and Sham, which introduces an auxiliary system of non-interacting electrons to approximate the interacting system. This approach, which will be discussed in the next section, forms the basis of the modern implementation of DFT.

2.3.3 Kohn-Sham Approach

While the Hohenberg-Kohn theorems guarantee the existence of a universal energy functional of the electron density, they do not provide a practical method to construct this functional. In 1965, Walter Kohn and Lu Jeu Sham addressed this limitation by introducing an elegant and computationally feasible scheme, now known as the Kohn-Sham (KS) formulation of DFT [45, 46]. The central idea is to replace the interacting many-electron system with an auxiliary system of non-interacting electrons that reproduces the same ground-state electron density as the real system.

Main Assumptions and Strategy

The Kohn-Sham approach relies on a set of foundational assumptions. It postulates the existence of a hypothetical system of non-interacting electrons that reproduces the same ground-state electron density $n_0(\mathbf{r})$ as that of the actual interacting system. Within this framework, the total energy is expressed as a functional of this density, where the known components are treated explicitly, and the complex many-body effects are encapsulated in an additional term. The non-interacting reference system is described using a set of single-particle Schrödinger-like equations governed by an effective potential $V_{\text{eff}}(\mathbf{r})$. In

Hartree atomic units ($\hbar = m_e = e = 4\pi\epsilon_0 = 1$), the Hamiltonian for a single electron in this auxiliary system is given by:

$$\hat{H}_s = -\frac{1}{2}\nabla^2 + V_{\text{eff}}(\mathbf{r}), \tag{2.9}$$

where $V_{\text{eff}}(\mathbf{r})$ represents the effective potential experienced by each electron in the fictitious non-interacting system.

Kohn-Sham Energy Functional

Using this construction, the universal Hohenberg-Kohn functional $F_{\text{HK}}[n]$ is approximated as [46]:

$$F_{\text{KS}}[n] = T_s[n] + E_H[n] + E_{\text{XC}}[n], \tag{2.10}$$

In the above equation the kinetic energy of the non-interacting reference system in Kohn-Sham DFT is denoted by $T_s[n]$. It is calculated using the Kohn-Sham orbitals $\psi_i(\mathbf{r})$ as follows [44]:

$$T_s[n] = \frac{1}{2}\sum_i \int |\nabla\psi_i(\mathbf{r})|^2 \, d\mathbf{r}, \tag{2.11}$$

where the summation runs over all occupied orbitals. The term $E_H[n]$ represents the classical electrostatic repulsion between electrons, often referred to as the Hartree energy, and is given by

$$E_H[n] = \frac{1}{2}\int\int \frac{n(\mathbf{r})n(\mathbf{r}')}{|\mathbf{r} - \mathbf{r}'|} \, d\mathbf{r} \, d\mathbf{r}'. \tag{2.12}$$

The exchange-correlation energy functional $E_{\text{XC}}[n]$ incorporates all remaining quantum mechanical effects beyond $T_s[n]$ and $E_H[n]$, including exchange interactions and electron correlation. Combining these contributions, the total Kohn-Sham energy functional takes the form:

$$E_{\text{KS}}[n] = F_{\text{KS}}[n] + \int V_{\text{ext}}(\mathbf{r})n(\mathbf{r}) \, d\mathbf{r}, \tag{2.13}$$

where $V_{\text{ext}}(\mathbf{r})$ is the external potential experienced by the electrons, typically arising from the nuclei.

Variational Principle and Kohn-Sham Equations

The ground-state electron density is determined by minimizing the Kohn-Sham energy functional with respect to variations in the density, in accordance with the Hohenberg-Kohn variational principle [46]:

$$\left.\frac{\delta E_{\text{KS}}[n]}{\delta n(\mathbf{r})}\right|_{n=n_0} = 0. \tag{2.14}$$

This minimization along with the constraint $\langle\psi_i\psi_j\rangle = \delta_{ij}$ yields a set of self-consistent single-particle equations known as the Kohn-Sham equations [43]:

$$\left(-\frac{1}{2}\nabla^2 + V_{\text{KS}}(\mathbf{r})\right)\psi_i(\mathbf{r}) = \epsilon_i\psi_i(\mathbf{r}), \tag{2.15}$$

where $\psi_i(\mathbf{r})$ are the Kohn-Sham orbitals and ϵ_i are their corresponding eigenvalues. The effective potential $V_{\text{KS}}(\mathbf{r})$ in these equations is composed of three contributions: the external potential $V_{\text{ext}}(\mathbf{r})$, the Hartree potential $V_H(\mathbf{r})$, and the exchange-correlation potential $V_{\text{XC}}(\mathbf{r})$, combined as

$$V_{\text{KS}}(\mathbf{r}) = V_{\text{ext}}(\mathbf{r}) + V_H(\mathbf{r}) + V_{\text{XC}}(\mathbf{r}). \tag{2.16}$$

The Hartree potential is given by $V_H(\mathbf{r}) = \int \frac{n(\mathbf{r}')}{|\mathbf{r}-\mathbf{r}'|}\,d\mathbf{r}'$, while the exchange-correlation potential is defined as the functional derivative of the exchange-correlation energy: $V_{\text{XC}}(\mathbf{r}) = \frac{\delta E_{\text{XC}}[n]}{\delta n(\mathbf{r})}$. Once the Kohn-Sham orbitals are obtained, the electron density is reconstructed from them as

$$n(\mathbf{r}) = \sum_{i=1}^{n} |\psi_i(\mathbf{r})|^2. \tag{2.17}$$

Self-Consistent Procedure

The Kohn-Sham potential $V_{\text{KS}}(\mathbf{r})$ is a functional of the electron density $n(\mathbf{r})$, which itself is constructed from the Kohn-Sham orbitals $\psi_i(\mathbf{r})$. Since these orbitals are determined by solving the Kohn-Sham equations that involve $V_{\text{KS}}(\mathbf{r})$, the process must be carried out iteratively until both the potential and the density are consistent with each other. The self-consistent field (SCF) method proceeds through the following general steps:

1. Begin with an initial estimate of the electron density, denoted $n^{(0)}(\mathbf{r})$.

2. Use this initial density to compute the corresponding Kohn-Sham potential $V_{\text{KS}}^{(0)}(\mathbf{r})$.

3. Solve the Kohn-Sham equations using $V_{\text{KS}}^{(0)}$ to obtain updated Kohn-Sham orbitals $\psi_i^{(1)}(\mathbf{r})$.

4. From the newly computed orbitals, construct an updated electron density $n^{(1)}(\mathbf{r}) = \sum_i |\psi_i^{(1)}(\mathbf{r})|^2$.

5. Evaluate whether the new density has sufficiently converged by comparing $n^{(1)}$ with $n^{(0)}$. If the change is below a predefined tolerance, the self-consistent solution is achieved. Otherwise, generate a new input density (e.g., using a mixing scheme) and repeat the cycle.

This iterative procedure continues until the input and output densities agree within the specified threshold. Upon achieving convergence, the final electron density and orbitals can be used to compute the ground-state properties of the system. This iterative process can be visualized by the flow chart as shown in the Figure 2.1

Thus, the Kohn-Sham formulation offers an efficient and practical route for applying density functional theory to complex many-electron systems. By replacing the original interacting system with an equivalent system of non-interacting electrons and incorporating the effects of electron interactions into the exchange-correlation functional, it allows for the reliable computation of ground-state properties in atoms, molecules, and solids. The effectiveness of DFT in fields like condensed matter physics and quantum chemistry is largely attributed to the accuracy and advancement of the exchange-correlation functional, which will be the focus of the next section.

2.3.4 Exchange and Correlation

In the previous section, we transformed the problem of interacting electrons into an auxiliary non-interacting system within the Kohn-Sham framework. This transformation is exact in principle, but in practice, all many-body effects are encapsulated into a single, unknown functional: the exchange-correlation energy functional, $E_{\text{XC}}[n]$. The exchange-correlation energy accounts for the difference between the true many-body energy and the sum of kinetic and classical electrostatic energies in the non-interacting reference system. It is customarily decomposed into two components:

$$E_{\text{XC}}[n] = E_{\text{X}}[n] + E_{\text{C}}[n], \tag{2.18}$$

where:

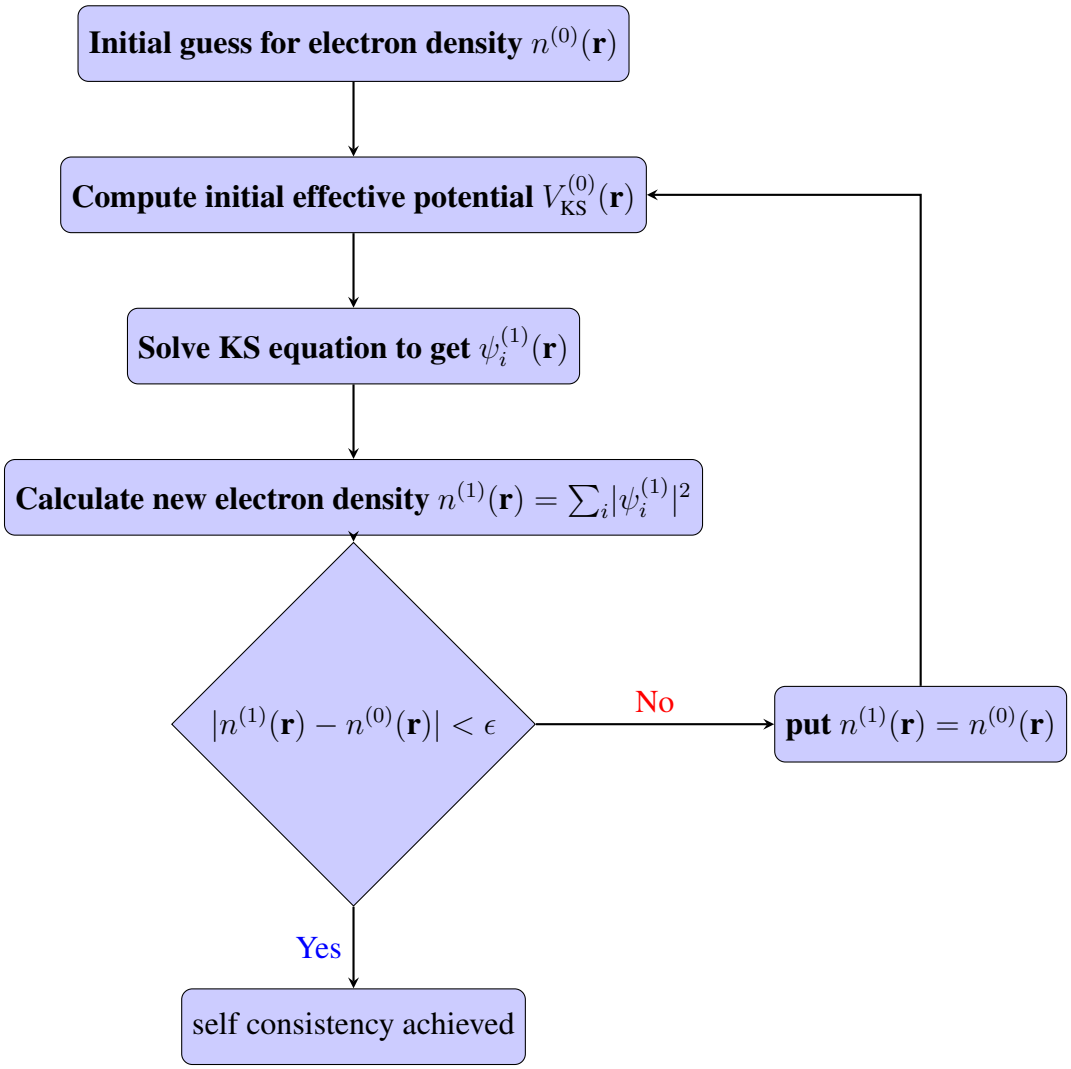

Figure 2.1: Flowchart illustrating the self-consistent procedure for solving the Kohn-Sham equations.

- $E_{\mathrm{X}}[n]$ is the **exchange energy**, which arises from the antisymmetry of the many-electron wavefunction (as required by the Pauli exclusion principle), leading to a reduction in the Coulomb repulsion between electrons with the same spin.
- $E_{\mathrm{C}}[n]$ is the **correlation energy**, which accounts for the remaining many-body interactions, particularly the correlated motion of electrons to avoid each other, beyond the mean-field Hartree description.

Physically, the exchange interaction tends to spatially separate electrons with parallel spins, reducing the probability of close encounters and thereby lowering the Coulomb repulsion. The correlation effect, on the other hand, provides an additional reduction in the total Coulomb energy by capturing the dynamic correlation between electrons, particularly those with opposite spins, which are not fully described by the exchange interaction alone [47]. While this effect may lead to a modest increase in the kinetic energy due to enhanced electron localization and motion, the overall contribution of the correlation energy results in a more accurate description of the ground-state energy and electron distribution [48].

The total exchange-correlation energy can be written formally as:

$$E_{\mathrm{XC}}[n] = \int n(\mathbf{r})\, \epsilon_{\mathrm{XC}}([n](\mathbf{r}))\, d^3\mathbf{r}, \tag{2.19}$$

where $\epsilon_{\mathrm{XC}}([n](\mathbf{r}))$ denotes the exchange-correlation energy per electron at the point $\mathbf{r}$. This quantity generally depends not only on the electron density $n(\mathbf{r})$ at that specific location, but also, in principle, on the distribution of the density in its vicinity, reflecting a non-local character. However, the precise mathematical form of $\epsilon_{\mathrm{XC}}[n]$ is not known, and therefore it must be treated using suitable approximations. The development of increasingly accurate approximations for $E_{\mathrm{XC}}[n]$ has been a central pursuit in the advancement of DFT. The two most widely used classes of approximations are described below.

2.3.4.1 Local Density Approximation (LDA)

The Local Density Approximation (LDA) represents the most basic and one of the earliest successful approaches for estimating the exchange-correlation energy in density functional theory. This method assumes that, at each point in space, the exchange-correlation energy density can be approximated by that of a uniform electron gas having the same local

electron density. Within this framework, the exchange-correlation energy is expressed as:

$$E_{\mathrm{XC}}^{\mathrm{LDA}}[n] = \int n(\mathbf{r})\, \epsilon_{\mathrm{XC}}^{\mathrm{hom}}(n(\mathbf{r}))\, d^3\mathbf{r}, \tag{2.20}$$

where $\epsilon_{\mathrm{XC}}^{\mathrm{hom}}(n)$ denotes the exchange-correlation energy per electron for a homogeneous electron gas of density n. This function has been accurately determined through quantum Monte Carlo studies of the uniform electron gas, and widely used analytic fits have been developed, including the well-known parametrization by Perdew and Zunger [49]. LDA is exact for systems with uniform electron density and performs remarkably well for many real materials where the density varies slowly over space. It accurately predicts structural properties such as lattice constants and bulk moduli in weakly correlated solids.

However, LDA tends to overbind atoms and molecules and underestimates band gaps in semiconductors and insulators [43]. These deficiencies motivated the development of more sophisticated approximations.

2.3.4.2 Generalized Gradient Approximation (GGA)

The Generalized Gradient Approximation (GGA) refines the Local Density Approximation by incorporating the effect of the spatial variation of the electron density [50]. Unlike LDA, which relies solely on the local value of the density $n(\mathbf{r})$, GGA also includes the gradient $\nabla n(\mathbf{r})$, enabling the functional to more accurately reflect the degree of inhomogeneity in the electron distribution. This additional dependence enhances the flexibility and accuracy of the functional in systems where the density changes significantly over space. The general expression for the GGA exchange-correlation functional is:

$$E_{\mathrm{XC}}^{\mathrm{GGA}}[n] = \int n(\mathbf{r})\, \epsilon_{\mathrm{XC}}(n(\mathbf{r}), |\nabla n(\mathbf{r})|)\, d^3\mathbf{r}. \tag{2.21}$$

This formulation allows GGA functionals to capture inhomogeneity effects and improve upon the LDA, especially for molecular systems, surfaces, and systems with rapid density variations [43].

In this thesis, we employ the PBE functional [51] for exchange and correlation, which is a non-empirical GGA designed to satisfy known physical constraints and provide improved accuracy for a wide range of systems, especially those where the LDA fails to capture important density variations.

Hence the accuracy of DFT calculations crucially depends on the choice of exchange-

correlation functional. While LDA provides a simple and computationally efficient approximation based on homogeneous electron gas, GGA represents a significant improvement for inhomogeneous systems. Despite their approximate nature, these functionals form the backbone of modern electronic structure calculations, and the quest for even more accurate functionals (such as hybrid or meta-GGA) continues to be an active area of research.

2.4 Periodic Supercells

Within the Kohn-Sham framework of density functional theory (DFT), the complex many-body problem involving interacting electrons is reformulated as an equivalent system of non-interacting electrons moving in an effective potential V_{KS}. Although this approach greatly reduces the complexity, it does not entirely eliminate all difficulties. One major challenge is that crystalline materials are inherently periodic, leading to an infinite number of electrons and nuclei. Another difficulty lies in the fact that the Kohn-Sham orbitals must be represented using a complete basis set, which is, by definition, infinite. These obstacles, however, can be overcome by leveraging the translational symmetry of crystalline solids. By applying periodic boundary conditions and invoking Bloch's theorem, the infinite system can be reduced to a finite problem defined within a primitive unit cell. Furthermore, the adoption of plane-wave basis sets, along with the use of pseudopotentials, makes the computational treatment of such systems feasible and efficient.

2.4.1 Bloch's Theorem

Bloch's theorem serves as a fundamental principle for analyzing electrons in a periodic potential, as encountered in crystalline solids. It asserts that if the potential satisfies the periodic condition $V(\mathbf{r}+\mathbf{T}) = V(\mathbf{r})$, where $\mathbf{T}$ denotes a lattice translation vector, then the eigenfunctions of the corresponding single-particle Schrödinger equation can be expressed in the following form:

$$\psi_{j\mathbf{k}}(\mathbf{r}) = e^{i\mathbf{k}\cdot\mathbf{r}} u_{j\mathbf{k}}(\mathbf{r}), \tag{2.22}$$

where $\mathbf{k}$ is the crystal momentum (wave vector) coming from periodic boundary conditions, j is the band index and $u_{j\mathbf{k}}(\mathbf{r})$ is a function with the periodicity of the lattice: $u_{j\mathbf{k}}(\mathbf{r}+\mathbf{T}) = u_{j\mathbf{k}}(\mathbf{r})$. This form enables us to focus our calculations on a single unit cell rather than the entire infinite crystal, thereby addressing the first computational challenge. The periodic

function $u_{j\mathbf{k}}(\mathbf{r})$ can be expanded using a plane-wave basis set [52]:

$$u_{j\mathbf{k}}(\mathbf{r}) = \frac{1}{\sqrt{\Omega}} \sum_{\mathbf{G}} C_{j,\mathbf{k}+\mathbf{G}} e^{i\mathbf{G}\cdot\mathbf{r}}, \tag{2.23}$$

where the sum runs over reciprocal lattice vectors $\mathbf{G}$, and Ω is the volume of the unit cell. Substituting this into the Bloch form of the wavefunction, we obtain:

$$\psi_{j\mathbf{k}}(\mathbf{r}) = \frac{1}{\sqrt{\Omega}} \sum_{\mathbf{G}} C_{j,\mathbf{k}+\mathbf{G}} e^{i(\mathbf{k}+\mathbf{G})\cdot\mathbf{r}}. \tag{2.24}$$

This expression shows that the Bloch wavefunction is a linear combination of plane waves characterized by momenta $\mathbf{k} + \mathbf{G}$.

Plane-Wave Cutoff

In principle, an infinite number of plane waves are required to represent the wavefunction accurately. However, in practice, high-momentum components contribute minimally to the total energy and can be neglected. Therefore, we introduce an energy cutoff E_{cut} to truncate the plane-wave expansion:

$$\frac{\hbar^2|\mathbf{k}+\mathbf{G}|^2}{2\mathbf{m}} \leq E_{\text{cut}}. \tag{2.25}$$

Only those reciprocal vectors $\mathbf{G}$ satisfying the above condition are retained in the basis set. Hence, the wavefunction becomes:

$$\psi_{j\mathbf{k}}(\mathbf{r}) = \frac{1}{\sqrt{\Omega}} \sum_{|\mathbf{k}+\mathbf{G}|\leq\mathbf{G}_{\text{cut}}} C_{j,\mathbf{k}+\mathbf{G}} e^{i(\mathbf{k}+\mathbf{G})\cdot\mathbf{r}}. \tag{2.26}$$

This approach resolves the second challenge by converting the infinite basis set into a finite one, whose size is controlled by E_{cut}. The value of E_{cut} is chosen by performing convergence tests on total energy or other physical properties of interest.

2.4.2 *k*-Point Sampling

To calculate physical observables like total energy, charge density, and density of states, integrals over the Brillouin zone (BZ) are requiblack. Since the BZ contains an infinite number of k-points, numerical integration is necessary using a finite grid of k-points. The

accuracy of these integrations strongly depends on the sampling of $\mathbf{k}$-space. Uniform grids of special $\mathbf{k}$-points can be generated using the Monkhorst-Pack scheme [53], which is one of the most widely used methods in plane-wave DFT calculations. In this scheme, the $\mathbf{k}$-points are defined as [54]:

$$\mathbf{k} = \sum_{i=1}^{n} \frac{m_i}{N_i} \mathbf{G}_i, \quad m_i = 1, 2, \ldots, N_i. \tag{2.27}$$

where $\mathbf{G}_i$'s are the reciprocal lattice vectors and N_i is the total number of unit cells in the direct lattice in the i^{th} direction . Instead of performing a continuous integration, the Brillouin zone is discretized into a finite set of $\mathbf{k}$-points. These points are often assigned weights based on the symmetry of the system, allowing the integration to be carried out efficiently over the irreducible portion of the Brillouin zone.

Here, q specifies the resolution of the $\mathbf{k}$-point grid used for sampling the Brillouin zone. Instead of performing a continuous integration, the Brillouin zone is discretized into a finite set of $\mathbf{k}$-points. These points are often assigned weights based on the symmetry of the system, allowing the integration to be carried out efficiently over the irreducible portion of the Brillouin zone.

2.4.3 Pseudopotentials

In atomic systems, core electron wavefunctions exhibit rapid oscillations in the vicinity of the nucleus, necessitating a very large number of plane waves for accurate representation. However, since core electrons are not involved in chemical bonding or low-energy excitations, their explicit treatment in most calculations is unnecessary. To address this inefficiency, the pseudopotential approximation is employed. This method involves substituting the true all-electron potential V_{ext} with a smoother effective potential V_{pseudo}, which interacts only with the valence electrons while effectively reproducing the influence of the nucleus and core electrons. Correspondingly, the true valence wavefunction is replaced by a pseudo wavefunction ψ_{pseudo} that agrees with the actual wavefunction beyond a certain core radius $\mathbf{r}_c$, but remains smooth and free of nodes within the core region. A schematic diagram of this pseudopotential and pseudo wavefunction, along with true wave function and true potential, is shown in Figure 2.2. This simplification dramatically decreases the number of plane waves needed for an accurate basis set, thereby reducing the overall computational effort. Two main categories of pseudopotentials are commonly used:

- **Norm-Conserving Pseudopotentials:** These enforce two conditions: (1) the pseudo

and all-electron wavefunctions must match beyond a cutoff radius r_c, and (2) their norms within r_c must be equal. These pseudopotentials are transferable and accurate but require a relatively large plane-wave basis [55].

- **Ultrasoft Pseudopotentials:** Introduced by Vanderbilt, these relax the norm-conservation constraint, allowing for even smoother pseudo wavefunctions. This leads to a smaller basis set and thus faster computations. However, additional terms (augmentation charges) are required to maintain accuracy [56].

An extension of this idea is the Projector Augmented-Wave (PAW) method, which reconstructs the full all-electron wavefunction from the pseudo one, offering an excellent compromise between accuracy and efficiency.

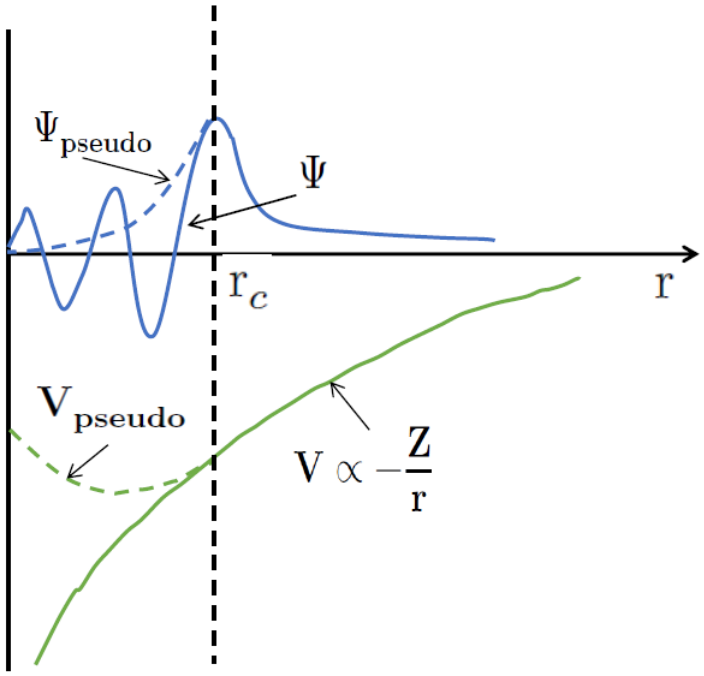

Figure 2.2: A schematic illustrating the all-electron and pseudo-electron potentials along with their respective wavefunctions [4].

Hence, the combined use of periodic boundary conditions, Bloch's theorem, **k**-point sampling, and pseudopotentials allows for efficient and accurate treatment of crystalline solids in DFT. These approximations and techniques change the infinite-dimensional problem to a computationally tractable form without significant loss of physical accuracy.

2.5 Calculation of Forces and Stresses

In density functional theory (DFT)-based simulations, the ability to compute forces on atoms and stresses on the unit cell is essential for geometry optimization, molecular dynamics, and response property calculations. These quantities are derived from the total energy of the system as a function of the nuclear positions and cell shape.

2.5.1 Forces on Atoms

The force on the I-th atom, located at position $\mathbf{R}_I$, is given by the negative derivative of the total energy $E(\mathbf{R})$ with respect to its position, representing the gradient of the energy landscape:

$$\mathbf{F}_I = -\frac{\partial E(\mathbf{R})}{\partial \mathbf{R}_I}. \tag{2.28}$$

In practice, this derivative is evaluated using the *Hellmann-Feynman theorem* [57,58], which provides an efficient route to compute forces within the Born-Oppenheimer approximation. For a normalized eigenstate $\Psi(\mathbf{R})$ of the electronic Hamiltonian H_{BO}, the theorem states:

$$\mathbf{F}_I = -\left\langle \Psi(\mathbf{R}) \left| \frac{\partial H_{\text{BO}}}{\partial \mathbf{R}_I} \right| \Psi(\mathbf{R}) \right\rangle. \tag{2.29}$$

This formulation allows the calculation of forces without requiring numerical derivatives of total energy through multiple configurations. In this context, H_{BO} is the electronic Hamiltonian with fixed nuclei, and the force arises due to the interaction between the electrons and the external ionic potential, as well as ion-ion interactions.

2.5.2 Stress Tensor

In addition to atomic forces, the stress on the unit cell is a crucial quantity, particularly in structural relaxation under pressure or cell deformation simulations. The stress tensor is defined as the derivative of the total energy with respect to a strain tensor applied to the unit cell. According to the "stress theorem" proposed by Nielsen and Martin [52, 59, 60], the stress tensor $\sigma^s_{\alpha\beta}$ is given by:

$$\sigma^s_{\alpha\beta} = -\frac{1}{\Omega}\frac{\partial E_{\text{tot}}}{\partial \epsilon_{\alpha\beta}}, \tag{2.30}$$

where $\epsilon_{\alpha\beta}$ is the strain tensor, α and β denote Cartesian indices (x, y, z), and Ω is the volume of the unit cell. The stress tensor provides insights into internal pressures and can be used for variable-cell optimization. It contains both kinetic and potential energy contributions:

$$\sigma^s_{\alpha\beta} = \sigma^{\text{kin}}_{\alpha\beta} + \sigma^{\text{ext}}_{\alpha\beta} + \sigma^{\text{xc}}_{\alpha\beta} + \sigma^{\text{ion}}_{\alpha\beta}, \tag{2.31}$$

where each term corresponds to:

- **Kinetic energy contribution**: from the response of the kinetic energy to cell deformation,
- **External potential contribution**: arising from the electron-ion interaction,
- **Exchange-correlation contribution**: due to the response of the exchange-correlation energy under strain,
- **Ion-ion contribution**: from classical electrostatic interactions among the nuclei.

In numerical implementations, these components are typically evaluated in reciprocal space, and their accuracy depends on the plane-wave cutoff and **k**-point sampling.

Stress and Variable-Cell Relaxation

In variable-cell relaxation (VC-relax), the stress tensor is minimized along with atomic forces. The target is to find both the equilibrium positions of atoms and the equilibrium shape and volume of the unit cell where:

$$\mathbf{F}_I = 0, \qquad \sigma^s_{\alpha\beta} = 0. \tag{2.32}$$

Hence, accurate force and stress calculations are fundamental to pblackicting structural, mechanical, and thermodynamic properties of materials.

2.6 Phonons from Density Functional Perturbation Theory

Phonons are the quantized modes of lattice vibrations in a crystalline solid and play a central role in determining a wide range of physical properties. These include vibrational spectra (as seen in Raman experiments), structural stability, thermal conductivity, specific

heat, and thermal expansion. Understanding phonon properties from first principles is, therefore, critical to the predictive modelling of materials. In 1954, Born and Huang developed a comprehensive theory of lattice dynamics [61], which laid the foundation for the quantum mechanical treatment of phonons. However, at the time, the computational tools required to solve the resulting equations for realistic systems were unavailable. With the development of Density Functional Theory (DFT) [62,63] and, later, Density Functional Perturbation Theory (DFPT) [64, 65], it became possible to compute phonon properties from first principles for complex materials containing many atoms per unit cell.

2.6.1 Lattice Dynamics from Electronic Structure Theory

Under the Born-Oppenheimer (BO) approximation, the dynamics of electrons and atomic nuclei is decoupled due to the large difference in their masses. It is assumed that electrons respond instantaneously to any change in the nuclear positions. Based on this assumption, lattice vibrations are analyzed by performing a Taylor expansion of the BO total energy $E(\mathbf{R})$ around the equilibrium atomic positions. The vibrational modes are then determined by solving the eigenvalue problem of the dynamical matrix, which is constructed from the second-order partial derivatives of the total energy with respect to atomic positions and includes mass-weighting.

$$\det \left| \frac{1}{\sqrt{\mathbf{M}_I \mathbf{M}_J}} \frac{\partial^2 E(\mathbf{R})}{\partial \mathbf{R}_I \partial \mathbf{R}_J} - \omega^2 \right| = 0, \tag{2.33}$$

where $\mathbf{M}_I$ and $\mathbf{M}_J$ are the masses of the I-th and J-th atoms, and ω denotes the phonon frequencies. The key quantity in Eqn. 2.33 is the Hessian matrix (also referred to as the force constant matrix), which requires the evaluation of second derivatives of the total energy. From the Hellmann-Feynman theorem (Section 1.5.1), the force experienced by the I-th nucleus is expressed as [64]:

$$\mathbf{F}_I = - \int n_{\mathbf{R}}(\mathbf{r}) \frac{\partial V_{\mathbf{R}}(\mathbf{r})}{\partial \mathbf{R}_I} \, d\mathbf{r} - \frac{\partial E_{\text{Ewald}}(\mathbf{R})}{\partial \mathbf{R}_I}, \tag{2.34}$$

where $n_{\mathbf{R}}(\mathbf{r})$ is the ground-state electron density for atomic configuration $\mathbf{R}$, $V_{\mathbf{R}}(\mathbf{r})$ is the electron-ion potential given by:

$$V_{\mathbf{R}}(\mathbf{r}) = - \sum_I \frac{Z_I e^2}{|\mathbf{r} - \mathbf{R}_I|}, \tag{2.35}$$

and $E_{\text{Ewald}}(\mathbf{R})$ is the classical Coulombic interaction energy among nuclei (Ewald energy). Differentiating Eqn. 2.34 with respect to atomic positions gives the second derivative of the BO energy, or the interatomic force constant matrix [64]:

$$\frac{\partial^2 E(\mathbf{R})}{\partial \mathbf{R}_I \partial \mathbf{R}_J} \equiv -\frac{\partial \mathbf{F}_I}{\partial \mathbf{R}_J} = \int \frac{\partial n_{\mathbf{R}}(\mathbf{r})}{\partial \mathbf{R}_J} \frac{\partial V_{\mathbf{R}}(\mathbf{r})}{\partial \mathbf{R}_I} \, d\mathbf{r} + \int n_{\mathbf{R}}(\mathbf{r}) \frac{\partial^2 V_{\mathbf{R}}(\mathbf{r})}{\partial \mathbf{R}_I \partial \mathbf{R}_J} \, d\mathbf{r} + \frac{\partial^2 E_{\text{Ewald}}(\mathbf{R})}{\partial \mathbf{R}_I \partial \mathbf{R}_J}. \tag{2.36}$$

This expression contains both electronic and ionic contributions to the force constants. The term $\partial n_{\mathbf{R}}(\mathbf{r})/\partial \mathbf{R}_J$ captures the first-order response of the electron density to nuclear displacements and is the most computationally challenging term to evaluate. The electron density $n_{\mathbf{R}}(\mathbf{r})$ is obtained from self-consistent DFT, while its first-order variation $\partial n_{\mathbf{R}}(\mathbf{r})/\partial \mathbf{R}_J$ is evaluated using DFPT.

2.6.2 Density-Functional Linear Response

DFPT provides a powerful and elegant framework for calculating linear responses of an interacting electron system to small perturbations, such as atomic displacements, electric fields, or strain. To compute the phonon spectrum, we consider perturbations to the nuclear positions and calculate the resulting first-order change in the electron density. The variation of the electron density $\Delta n(\mathbf{r})$ due to an atomic displacement is given by [64]:

$$\Delta n(\mathbf{r}) = 4 \, \text{Re} \sum_{n=1}^{N_{\text{occ}}} \psi_n^*(\mathbf{r}) \Delta \psi_n(\mathbf{r}), \tag{2.37}$$

where $\Delta \psi_n(\mathbf{r})$ represents the first-order perturbative correction to the Kohn-Sham (KS) orbital $\psi_n(\mathbf{r})$, derived via conventional first-order perturbation theory [64]:

$$(H_{\text{SCF}} - \epsilon_n)|\Delta \psi_n\rangle = -(\Delta V_{\text{SCF}} - \Delta \epsilon_n)|\psi_n\rangle, \tag{2.38}$$

with H_{SCF} being the unperturbed KS Hamiltonian, ϵ_n the KS eigenvalue, and $\Delta \epsilon_n = \langle \psi_n | \Delta V_{\text{SCF}} | \psi_n \rangle$. The perturbed self-consistent potential ΔV_{SCF} includes contributions from the external perturbation, the induced Hartree potential, and the exchange-correlation (XC) potential [64]:

$$\Delta V_{\text{SCF}}(\mathbf{r}) = \Delta V(\mathbf{r}) + e^2 \int \frac{\Delta n(\mathbf{r}')}{|\mathbf{r} - \mathbf{r}'|} d\mathbf{r}' + \left. \frac{dv_{\text{XC}}(n)}{dn} \right|_{n=n(\mathbf{r})} \Delta n(\mathbf{r}). \tag{2.39}$$

These equations form a closed, self-consistent set, completely analogous to the KS equations for the unperturbed system. The variation of KS orbitals $\Delta\psi_n(\mathbf{r})$ can also be written in its spectral form [64]:

$$\Delta\psi_n(\mathbf{r}) = \sum_{m\neq n} \psi_m(\mathbf{r}) \frac{\langle\psi_m|\Delta V_{\text{SCF}}|\psi_n\rangle}{\epsilon_n - \epsilon_m}. \tag{2.40}$$

In principle, the spectral expression requires knowledge of the entire unoccupied KS spectrum. However, DFPT avoids explicit summation over unoccupied states by solving the linear system directly in the occupied subspace, which significantly reduces computational cost.

Hence, the steps to compute phonon frequencies using DFPT are:

1. Solve the ground-state KS equations to obtain $n(\mathbf{r})$ and $\psi_n(\mathbf{r})$.
2. Apply a small perturbation (e.g., atomic displacement) and solve the linearized KS equations to obtain $\Delta\psi_n(\mathbf{r})$.
3. Use $\Delta\psi_n(\mathbf{r})$ to compute $\Delta n(\mathbf{r})$.
4. Use $\Delta n(\mathbf{r})$ in Eqn. 2.36 to compute the dynamical matrix.
5. Diagonalize the dynamical matrix to obtain phonon frequencies and eigenvectors.

This method enables the calculation of full phonon dispersion curves and related lattice dynamical properties with high accuracy and efficiency.

2.7 Electronic Transport

Electronic transport properties were evaluated using the Boltzmann transport theory within the constant relaxation time and rigid band approximations (CRTA). In this approach, the transport coefficients per unit relaxation time were first computed by solving the Boltzmann transport equation. Subsequently, the relaxation time was estimated using deformation potential theory, which captures the scattering of charge carriers by acoustic phonons.

2.7.1 Transport coefficient under constant relaxation time approximation

When a temperature gradient ∇T and an electric field $\mathbf{E}$ are applied to a material, the system deviates from equilibrium. In such a situation, the electron distribution function $f(T;\mu)$ no longer matches the equilibrium distribution $f_0(T;\mu)$, and instead takes the form:

$$f(T;\mu) = f_0(T;\mu) + \delta f(T;\mu) \tag{2.41}$$

The time evolution of this distribution function f is governed by the Boltzmann transport equation, which can be written as [66]:

$$\frac{df}{dt} = \left(\frac{\partial f}{\partial t}\right)_{\text{coll}} + \left(\frac{\partial f}{\partial t}\right)_{\text{diff}} + \left(\frac{\partial f}{\partial t}\right)_{\text{field}}. \tag{2.42}$$

Here, the diffusion and field terms represent the contributions to the change in distribution due to the temperature gradient and the electric field, respectively. These are given by [66]:

$$\left(\frac{\partial f}{\partial t}\right)_{\text{diff}} = \text{-}\mathbf{v_k} \cdot \nabla_{\mathbf{r}} f = \text{-}\mathbf{v_k} \cdot \left(\frac{\partial f}{\partial T}\right) \nabla T \tag{2.43}$$

$$\left(\frac{\partial f}{\partial t}\right)_{\text{field}} = \text{-}e\mathbf{E}.\nabla_k f = \text{-}e\mathbf{E} \cdot \mathbf{v_k} \left(\text{-}\frac{\partial f}{\partial \epsilon}\right) \tag{2.44}$$

Where $v_{\mathbf{k}} = \frac{\nabla \epsilon_{\mathbf{k}}}{\hbar}$

In steady state, the time derivative of the distribution function vanishes:

$$\frac{df}{dt} = 0 \tag{2.45}$$

As a result, the Boltzmann transport equation (Equation 2) reduces to:

$$\text{-}\left(\frac{\partial f}{\partial t}\right)_{\text{coll}} = \left(\frac{\partial f}{\partial t}\right)_{\text{diff}} + \left(\frac{\partial f}{\partial t}\right)_{\text{field}}. \tag{2.46}$$

By substituting Equations 2.43 and 2.44 in Equation 2.42, and assuming that the non-equilibrium distribution function f varies with temperature T and energy ϵ in a way that closely resembles the equilibrium distribution f_0, we obtain:

$$\text{-}\left(\frac{\partial f}{\partial t}\right)_{\text{coll}} = \text{-}e\,\mathbf{E} \cdot \mathbf{v_k} \left(\text{-}\frac{\partial f_0}{\partial \varepsilon}\right) \text{ - } \mathbf{v_k} \cdot \nabla T \left(\frac{\partial f_0}{\partial T}\right) \tag{2.47}$$

In the constant relaxation time approximation (RTA), it is assumed that the perturbation due to the temperature gradient and applied electric field slightly disturbs the distribution function f. This disturbed distribution then relaxes back to equilibrium f_0 over a characteristic time scale τ, referred to as the relaxation time. Within this approximation, the collision term is modeled as:

$$\left(\frac{\partial f}{\partial t}\right)_{\text{coll}} = \frac{f \text{ - } f_0}{\tau} = \frac{\delta f}{\tau} \tag{2.48}$$

Furthermore, using the identity:

$$\frac{\partial f_0}{\partial T} = \frac{\varepsilon \text{ - } \mu}{T}\left(\text{-}\frac{\partial f_0}{\partial \varepsilon}\right) \tag{2.49}$$

the Boltzmann transport equation becomes:

$$\frac{\delta f}{\tau} = \mathbf{v_k} \cdot \left[\text{-}e\,\mathbf{E} + \frac{\varepsilon \text{ - } \mu}{T}\nabla T\right]\left(\text{-}\frac{\partial f_0}{\partial \varepsilon}\right) \tag{2.50}$$

The electric current density is defined as [54]:

$$\mathbf{J}_e = \text{-}e \int \frac{d^3k}{(2\pi)^3}\,\mathbf{v_k}\,\delta f \tag{2.51}$$

Similarly, the heat current—which refers to the component of the energy current not associated with particle flow—is defined as [54]:

$$\mathbf{J}_q = \int \frac{d^3k}{(2\pi)^3}\,(\varepsilon_{\mathbf{k}} \text{ - } \mu)\,\mathbf{v_k}\,\delta f \tag{2.52}$$

By substituting δf from Equation 2.50 into Equations 2.51 and 2.52, and comparing the resulting expressions for the electric current $\mathbf{J}_e$ and the heat current $\mathbf{J}_q$ with their standard forms involving the electrical conductivity σ, Seebeck coefficient α, and the electronic contribution to thermal conductivity κ^e:

$$\mathbf{J_e} = \sigma\mathbf{E} \text{ - } \sigma\alpha\nabla T, \quad \mathbf{J}_q = T\alpha\sigma\mathbf{E} \text{ - } \kappa^e\nabla T, \tag{2.53}$$

we obtain the $(ij)^{\text{th}}$ component of the electrical conductivity per unit relaxation time $\left(\frac{\sigma_{ij}(T;\mu)}{\tau}\right)$, the Seebeck coefficient $(\alpha_{ij}(T;\mu))$, and the electronic thermal conductivity per

unit relaxation time $\left(\frac{\kappa_{ij}^{e}(T;\mu)}{\tau}\right)$ as follows [67, 68]:

$$\frac{\sigma_{ij}(T;\mu)}{\tau} = \frac{1}{\Omega}\int d\epsilon \left(-\frac{\partial f_0}{\partial \epsilon}\right)\left(\frac{\sigma_{ij}(\epsilon)}{\tau}\right) \tag{2.54}$$

where the projected conductivity tensor $\sigma_{ij}(\epsilon)$ is defined by:

$$\frac{\sigma_{ij}(\epsilon)}{\tau} = e^2 \sum_{\beta}\int \frac{d^3\mathbf{k}}{4\pi^3}\delta(\epsilon - \epsilon(\beta;\mathbf{k}))v_i(\beta;\mathbf{k})v_j(\beta;\mathbf{k}) \tag{2.55}$$

$$\begin{aligned}\alpha_{ij}(T;\mu) = &\left(\frac{1}{eT\Omega}\right)\sum_{k}\left(\tau\sigma_{ik}^{-1}(T;\mu)\right)\\ &\left(\int d\epsilon\left(-\frac{\partial f_0}{\partial \epsilon}\right)(\epsilon - \mu)\left(\frac{\sigma_{kj}(\epsilon)}{\tau}\right)\right)\end{aligned} \tag{2.56}$$

and the expression for the electronic thermal conductivity per unit relaxation time is:

$$\frac{\kappa_{ij}^{e}(T;\mu)}{\tau} = \frac{\kappa_{ij}(T;\mu)}{\tau} - T\sum_{\alpha,\beta}\nu_{i\alpha}\left(\frac{\sigma_{\beta\alpha}^{-1}}{\tau}\right)\nu_{\beta j} \tag{2.57}$$

where the terms on the right-hand side are defined as:

$$\frac{\kappa_{ij}(T;\mu)}{\tau} = \left(\frac{1}{e^2T\Omega}\right)\int d\epsilon\left(-\frac{\partial f_0}{\partial \epsilon}\right)(\epsilon - \mu)^2\left(\frac{\sigma_{ij}(\epsilon)}{\tau}\right) \tag{2.58a}$$

and

$$\nu_{ij} = \frac{1}{eT\Omega}\int d\epsilon\left(-\frac{\partial f_0}{\partial \epsilon}\right)(\epsilon - \mu)\left(\frac{\sigma_{kj}(\epsilon)}{\tau}\right) \tag{2.58b}$$

In Equation (2.55), the summation is taken over all electronic bands β, and Ω denotes the volume of the unit cell of the crystal.

2.7.2 Relaxation time of charge carriers using deformation potential theory

Due to lattice vibrations, a local strain field described by the divergence of the atomic displacement, $\nabla \cdot \mathbf{u}(\mathbf{r})$, arises within the crystal. This strain locally perturbs the periodic potential experienced by charge carriers. The resulting perturbation in the Hamiltonian, denoted as H_{e-ph}, represents the interaction between electrons or holes and acoustic phonons. This interaction causes scattering of carriers located near the conduction band

minimum (CBM) and the valence band maximum (VBM). The form of this electron-phonon interaction Hamiltonian is given by [69, 70]:

$$H_{e-ph}(\mathbf{r}) = \Xi \ \nabla \cdot \mathbf{u}(\mathbf{r}) \tag{2.59}$$

where Ξ is the deformation potential constant, which characterizes the shift in the electronic band edge energy E_{edge} in response to lattice strain, defined as the relative change in lattice parameter $(a - a_0)$, with a_0 being the equilibrium lattice constant.

$$\Xi = \left(\frac{\partial E_{edge}}{\partial \left(\frac{\Delta a}{a_0} \right)} \right)_{a=a_0} \tag{2.60}$$

The displacement field $\mathbf{u}(\mathbf{r})$ [69] and the electron-phonon interaction Hamiltonian $H_{e\text{-}ph}$ are given by:

$$\mathbf{u}(\mathbf{r}) = \frac{1}{\sqrt{N}} \sum_{\mathbf{q}} \mathbf{e}_{\mathbf{q}} \left(a_{\mathbf{q}} e^{i\mathbf{q}\cdot\mathbf{r}} + a_{\mathbf{q}}^{\dagger} e^{-i\mathbf{q}\cdot\mathbf{r}} \right) \tag{2.61}$$

$$H_{e-ph} = \frac{\Xi}{\sqrt{N}} \sum_{\mathbf{q}} (i\mathbf{q} \cdot \mathbf{e}_{\mathbf{q}}) \left(a_{\mathbf{q}} e^{i\mathbf{q}\cdot\mathbf{r}} - a_{\mathbf{q}}^{\dagger} e^{-i\mathbf{q}\cdot\mathbf{r}} \right) \tag{2.62}$$

Here, N is the number of lattice sites per unit volume, $\mathbf{e}_{\mathbf{q}}$ is the polarization unit vector of the acoustic phonon mode, and $a_{\mathbf{q}}$ is the phonon annihilation operator corresponding to the wave vector $\mathbf{q}$. For transverse acoustic phonons, the polarization vector is perpendicular to the wave vector, i.e., $\mathbf{e}_{\mathbf{q}} \perp \mathbf{q}$, which implies that $\mathbf{q} \cdot \mathbf{e}_{\mathbf{q}} = 0$. As a result, the electron-phonon interaction Hamiltonian $H_{e\text{-}ph}$ vanishes for transverse acoustic modes. In contrast, for longitudinal acoustic phonons, the polarization is parallel to the wave vector: $\mathbf{e}_{\mathbf{q}} = \hat{\mathbf{q}}$, so that $\mathbf{q} \cdot \mathbf{e}_{\mathbf{q}} = q$. Therefore, the electron-phonon interaction Hamiltonian simplifies to the following form for longitudinal acoustic modes:

$$H_{\text{e-ph}}(\mathbf{r}) = \frac{\Xi}{\sqrt{N}} \sum_{\mathbf{q}} iq \left(a_{\mathbf{q}} e^{i\mathbf{q}\cdot\mathbf{r}} - a_{\mathbf{q}}^{\dagger} e^{-i\mathbf{q}\cdot\mathbf{r}} \right) \tag{2.63}$$

The relaxation time $\tau(E_{\mathbf{k}})$, associated with the perturbed Hamiltonian, is obtained using Fermi's golden rule as follows [69]:

$$\frac{1}{\tau(\epsilon_{\mathbf{k}})} = \frac{2\pi}{\hbar} \sum_{\boldsymbol{q}} |M_{\mathbf{k},\mathbf{k}+\mathbf{q}}|^2 \delta(\epsilon_{\mathbf{k}} - \epsilon_{\mathbf{k}\pm\mathbf{q}} \mp \hbar\omega_{\boldsymbol{q}}) \tag{2.64}$$

Here, $M_{\mathbf{k},\mathbf{k+q}}$ denotes the matrix element for an electron initially in the state $|\mathbf{k}\rangle$ being scattered to the state $|\mathbf{k}+\mathbf{q}\rangle$ due to the interaction with a phonon of wave vector $\mathbf{q}$ via the perturbed Hamiltonian described above. The expression for $M_{\mathbf{k},\mathbf{k+q}}$ is given by:

$$\begin{aligned} M_{\mathbf{k},\mathbf{k+q}} &= \langle \mathbf{k}+\mathbf{q}| \, |H_{e-ph}||\mathbf{k}\rangle \\ &= \int \psi^*_{\mathbf{k+q}}(\mathbf{r}) H_{e-ph}(\mathbf{r}) \psi_{\mathbf{k}}(\mathbf{r}) \, d^3r \\ &= \frac{\Xi \, q}{V} \frac{1}{\sqrt{N}} \int e^{-i\mathbf{k}'\cdot\mathbf{r}} \left(a_{\mathbf{q}} e^{i\mathbf{q}\cdot\mathbf{r}} + a^{\dagger}_{\mathbf{q}} e^{-i\mathbf{q}\cdot\mathbf{r}} \right) e^{i\mathbf{k}\cdot\mathbf{r}} d^3r \end{aligned}$$

where,

$$\psi_{\mathbf{k}}(\mathbf{r}) = \frac{1}{\sqrt{V}} e^{i\mathbf{k}\cdot\mathbf{r}}, \tag{2.65}$$

In the high-temperature limit, the phonon occupation leads to $|a_{\mathbf{q}}|^2 = \dfrac{k_b T N}{2\rho q^2 v^2_{\mathbf{q}}}$, where ρ is the mass density of the crystal and $v_{\mathbf{q}}$ is the group velocity of the longitudinal acoustic phonon. Substituting this into the expression for the matrix element, the squared magnitude of the scattering matrix element becomes:

$$|M_{\mathbf{k},\mathbf{k+q}}|^2 = \frac{k_B T \Xi^2}{C} \tag{2.66}$$

Here, $C = 2\rho v^2_{\mathbf{q}}$ represents the elastic constant, which is also expressed as:

$$C = \left(\frac{1}{V_0} \frac{\partial^2 E}{\partial \left(\frac{\Delta a}{a_0} \right)^2} \right)_{a=a_0} \tag{2.67}$$

Here, E denotes the total electronic energy obtained from density functional theory (DFT) calculations. We substitute the expression for $|M_{\mathbf{k},\mathbf{k+q}}|^2$ into Equation 2.64 and perform an average over all electronic states near the band edge b [69], resulting in:

$$\tau_b = \frac{\int \tau_b(\epsilon_{\mathbf{k}}) f(\epsilon_{\mathbf{k}}) d\mathbf{k}}{\int f(\epsilon_{\mathbf{k}}) d\mathbf{k}} \tag{2.68}$$

Here, $f(E_{\mathbf{k}})$ is the Fermi–Dirac distribution function, and the integration is carried out over the electronic states within band b. The resulting relaxation time associated with band b thus obtained is:

$$\tau_b = \frac{2\,(2\pi)^{\frac{1}{2}}\,\hbar^4 C}{3\Xi^2\,(k_B T)^{\frac{3}{2}}\,(m_D^*)^{\frac{3}{2}}} \tag{2.69}$$

The quantity m_D^* denotes the density-of-states effective mass for band b, and is defined as:

$$m_D^* = N_v^{\frac{2}{3}}\,(m_l.m_{t_1}.m_{t_2})^{\frac{1}{3}} \tag{2.70}$$

Here, N_v represents the valley degeneracy, while m_l and m_t denote the longitudinal and transverse effective masses, respectively. The averaging over the three spatial directions is performed because, near the band extrema, the constant energy surfaces are ellipsoidal in shape, resulting in anisotropic effective masses along the longitudinal and transverse axes of the ellipsoid.

The effective mass is defined as:

$$\frac{1}{m^*} = \frac{1}{\hbar^2}\frac{\partial^2 \epsilon}{\partial k^2} \tag{2.71}$$

Likewise, the conductivity effective mass associated with a given band is given by:

$$\frac{1}{m_\sigma^*} = \frac{1}{3}\left(\frac{1}{m_l^*} + \frac{1}{m_{t1}^*} + \frac{1}{m_{t2}^*}\right). \tag{2.72}$$

The mobility of charge carriers for a specific band b (denoted as μ_b) is expressed by:

$$\mu_b = \frac{e\tau_b}{m_\sigma^*} \tag{2.73}$$

In systems where multiple bands contribute significantly near the valence band (VB) or conduction band (CB) due to degeneracy or near-degeneracy, the average carrier mobility μ_{av} and the average conductivity effective mass $m_{\sigma,av}^*$ are defined as follows [71]:

$$\mu_{av} = \sum_b \frac{n_b}{n}\mu_b \;\;, \quad \frac{1}{m_{\sigma,av}^*} = \sum_b \frac{n_b}{n}\frac{1}{m_{\sigma,b}^*} \tag{2.74}$$

Here, n_b represents the carrier concentration in the valley of band b, and $n = \sum_b n_b$ is the total carrier concentration. The proportion of carriers residing in the valley of band b

relative to the VB or CB is given by:

$$\frac{n_b}{n_{VB/CB}} = \left(\frac{m^*_{D,b}}{m^*_{D,VB/CB}}\right)^{\frac{3}{2}} \exp\left(-\frac{\Delta E}{k_B T}\right) \tag{2.75}$$

where ΔE denotes the energy offset between the valley extremum and the VBM/CBM. Finally, the average relaxation time that takes into account all contributing valley extrema is given by [71]:

$$\tau_{av} = \frac{m^*_{\sigma,av}\mu_{av}}{e} \tag{2.76}$$

2.8 Phonon Boltzmann transport equation (PBTE)

Just like in electron transport, when a temperature gradient ∇T is applied to a material, it disturbs the equilibrium of the system. Because of the temperature gradient, the distribution of phonons (quantized lattice vibrations) also gets disturbed. At thermal equilibrium (no ∇T), phonons follow the Bose-Einstein distribution, denoted as n^0_ς (ς represents phonon mode having wave vector **q** and branch index p). However, when ∇T is present, phonons are driven out of equilibrium, and their distribution function becomes n_ς, which is different from n^0_ς. The time evolution of this nonequilibrium phonon distribution is governed by the phonon Boltzmann transport equation (BTE), which provides a framework to describe how phonons behave under external perturbations like temperature gradients. This BTE for phonons is given by [66, 72, 73]:

$$\frac{dn_\varsigma}{dt} = \left(\frac{\partial n_\varsigma}{\partial t}\right)_{\text{scatt}} + \left(\frac{\partial n_\varsigma}{\partial t}\right)_{\text{diff}} \tag{2.77}$$

The first term on the right-hand side represents the scattering processes occurring within the system, while the second term accounts for diffusion arising from the spatial temperature gradient. Under steady-state conditions, as discussed in [72]:

$$\frac{dn_\varsigma}{dt} = 0; \quad \text{and} \quad \left(\frac{\partial n_\varsigma}{\partial t}\right)_{\text{diff}} = \text{-}\mathbf{v}_\varsigma \cdot \nabla T \frac{\partial n_\varsigma}{\partial T} \tag{2.78}$$

Using Equation 2.78 in Equation 2.77, we get :

$$\mathbf{v}_\varsigma \cdot \nabla T \frac{\partial n_\varsigma}{\partial T} = \left.\frac{\partial n_\varsigma}{\partial t}\right|_{\text{scatt}} \tag{2.79}$$

2.8.1 Linearized phonon BTE

When temperature gradient is small, we can linearized the phonon BTE with :

$$n_\varsigma = n_\varsigma^0 + n_\varsigma^0(1+n_\varsigma^0)\Phi_\varsigma, \tag{2.80}$$

where Φ_ς is a small perturbation which is linear in temperature gradient ∇T.
In phonon-phonon interactions, two primary types of three-phonon processes can occur: absorption and emission. In an absorption process, a phonon ς absorbs another phonon ς' to become a third phonon ς'', whereas in an emission process, a phonon ς decays into two phonons ς' and ς''. All such processes must satisfy two fundamental conservation laws. The first is energy conservation, given by $\omega_\varsigma \pm \omega_{\varsigma'} = \omega_{\varsigma''}$, and the second is momentum conservation, represented by $\mathbf{q}_\varsigma \pm \mathbf{q}_{\varsigma'} = \mathbf{q}_{\varsigma''} + \mathbf{G}$, where $\mathbf{G}$ is a reciprocal lattice vector that ensures all phonon wavevectors $\mathbf{q}$ lie within the same Brillouin zone (BZ) image. When $\mathbf{G} = 0$, the process is termed a Normal (N) process, while for $\mathbf{G} \neq 0$, it is classified as an Umklapp (U) process. When only three phonon scattering is taken into account, this linearized phonon BTE becomes [74, 75] :

$$\text{-}\mathbf{v}_\varsigma \cdot \nabla T \frac{\partial n_\varsigma^0}{\partial T} = n_\varsigma^0(1+n_\varsigma^0)\frac{1}{N}\sum_{\varsigma'\varsigma''}\left[(\Phi_\varsigma + \Phi_{\varsigma'} \text{ - } \Phi_{\varsigma''})\Gamma^{+}_{\varsigma\varsigma'\varsigma''} + \frac{1}{2}(\Phi_\varsigma \text{ - } \Phi_{\varsigma'} \text{ - } \Phi_{\varsigma''})\Gamma^{\text{-}}_{\varsigma\varsigma'\varsigma''}\right] \tag{2.81}$$

In the above equation, N is the number of $\mathbf{q}$ points in the Brillouin zone. The quantities $\Gamma^{+}_{\varsigma\varsigma'\varsigma''}$ and $\Gamma^{\text{-}}_{\varsigma\varsigma'\varsigma''}$are the transition rates for three-phonon absorption $(+)$ and emission (-) processes, respectively, which can be calculated using first-principles methods.

By transformation $\phi_\varsigma = \text{-}\frac{\hbar}{k_B T^2}\mathbf{E}_\varsigma \cdot \nabla T$ Equation 2.81 becomes [76]:

$$\left\{\text{-}\omega_\varsigma \mathbf{v}_\varsigma + \frac{1}{N}\sum_{\varsigma'\varsigma''}\left[(\mathbf{E}_\varsigma + \mathbf{E}_{\varsigma'}\text{-}\mathbf{E}_{\varsigma''})\Gamma^{+}_{\varsigma\varsigma'\varsigma''} + \frac{1}{2}(\mathbf{E}_\varsigma\text{-}\mathbf{E}_{\varsigma'}\text{-}\mathbf{E}_{\varsigma''})\Gamma^{\text{-}}_{\varsigma\varsigma'\varsigma''}\right]\right\} \cdot \nabla T = 0 \tag{2.82}$$

The phonon Boltzmann transport equation (BTE) given above can be recast as a system of linear equations in terms of $\mathbf{E}_\varsigma$, expressed as

$$\sum_{\varsigma'} \Lambda_{\varsigma\varsigma'}\mathbf{E}_{\varsigma'} = \mathbf{B}_\varsigma,$$

where Λ is a square matrix of coefficients and $\mathbf{B}_\varsigma = \omega_\varsigma \mathbf{v}_\varsigma$. In the case where only Normal (N) processes are considered, the equation

$$\sum_{\varsigma'} \Lambda_{\varsigma\varsigma'} \mathbf{E}_{\varsigma'} = 0$$

holds true not only for the trivial solution $\mathbf{E}_{\varsigma'} = 0$, but also for $\mathbf{E}_{\varsigma'} = \mathbf{q}_{\varsigma'}$. This implies that a finite heat current can exist even in the absence of a temperature gradient ($\nabla T = 0$). As a result, N processes alone are insufficient to relax the heat current, and thus lead to a divergent (infinite) thermal conductivity κ [75, 76].

The heat current **J** arising from a small temperature gradient can be formulated using the phonon distribution function as [77] :

$$\mathbf{J} = \frac{1}{NV} \sum_{\varsigma} \hbar \omega_\varsigma \mathbf{v}_\varsigma n_\varsigma = \text{-} \frac{1}{k_B T^2 NV} \sum_{\varsigma} \hbar^2 \omega_\varsigma^2 n_\varsigma^0 (1 + n_\varsigma^0) \mathbf{v}_\varsigma (\mathbf{E}_\varsigma \cdot \nabla T) \tag{2.83}$$

Where V is the volume of the unit cell. From the Fourier's law :

$$J^i = \sum_j \kappa^{ij} (\nabla T)^j \tag{2.84}$$

, the lattice thermal conductivity κ^{ij} is given by,

$$\kappa^{ij} = \frac{1}{k_B T^2 NV} \sum_{\varsigma} \hbar^2 \omega_\varsigma^2 n_\varsigma^0 (1 + n_\varsigma^0) v_\varsigma^i E_\varsigma^j \tag{2.85}$$

2.8.2 Callaway model

Solving the linear equations $\sum_{\varsigma'} \Lambda_{\varsigma\varsigma'} E_{\varsigma'} = B_\varsigma$ is challenging due to the high dimensionality involved. Moreover, the exact solution of the BTE is often unnecessary because the coefficients $\Lambda_{\varsigma\varsigma'}$, which depend on the interatomic potential, may not be accurately known. As a result, the relaxation time approximation (RTA) is commonly used instead. Under this relaxation time approximation, the Boltzmann transport equation is written as

$$\text{-} \mathbf{v}_\varsigma \cdot \nabla T \frac{\partial n_\varsigma^0}{\partial T} = \frac{n_\varsigma \text{-} n_\varsigma^0}{\tau_\varsigma^C} \tag{2.86}$$

In the relaxation time approximation (RTA), the relaxation time τ_ς^C is parameterized.

However, RTA tends to underestimate the thermal conductivity κ, because it assumes all scattering processes are resistive, which is not always true. For example, RTA predicts a finite κ even when only Normal (N) processes are present, which should instead lead to infinite κ. To address this, Callaway proposed treating Normal (N) and Umklapp (U) processes separately, using the relation

$$\frac{1}{\tau_\varsigma^C} = \frac{1}{\tau_\varsigma^N} + \frac{1}{\tau_\varsigma^U} + \frac{1}{\tau_\varsigma^{PD}}$$

where τ_ς^Nm, τ_ς^U and τ_ς^{PD} are the relaxation times for N, U, and point defect scattering processes, respectively. He then modified the original expression accordingly as given by [77, 78]:

$$\text{-}\mathbf{v}_\varsigma \cdot \nabla T \frac{\partial n_\varsigma^0}{\partial T} = \frac{n_\varsigma \text{-} n_\varsigma^0}{\tau_\varsigma^C} + \frac{n_\varsigma \text{-} n_\varsigma^*}{\tau_\varsigma^N} \tag{2.87}$$

Umklapp (U) processes and scattering because of point defects (PD) drive the phonon distribution n_ς toward the equilibrium distribution n_ς^0, while Normal (N) processes push it toward a displaced distribution n_ς^*, which depends on both the phonon wavevector $\mathbf{q}_\varsigma$ and frequency ω_ς. This displaced distribution function can be expressed approximately as [77, 78]:

$$n_\varsigma^* \approx n_\varsigma^0 \text{ - } n_\varsigma^0(1 + n_\varsigma^0)(\mathbf{A} \cdot \mathbf{q}_\varsigma) \tag{2.88}$$

where $\mathbf{A}$ is a Lagrange multiplier. Substituting Equation 2.88 in the Equation 2.87 we get :

$$n_\varsigma \text{-} n_\varsigma^0 = \text{-}\tau_\varsigma^C \mathbf{v}_\varsigma \cdot \nabla T \frac{\partial n_\varsigma^0}{\partial T} \text{ - } \frac{\tau_\varsigma^C}{\tau_\varsigma^N} \frac{k_B T^2}{\hbar \omega_\varsigma} (\mathbf{A} \cdot \mathbf{q}_\varsigma) \frac{\partial n_\varsigma^0}{\partial T} \tag{2.89}$$

To solve the equation, Callaway used the fact that Normal (N) processes conserve phonon momentum. Therefore, he set the rate of change of the total phonon momentum due to N processes to zero, as described in [78] and is given by :

$$\sum_\varsigma \frac{n_\varsigma \text{ - } n_\varsigma^*}{\tau_\varsigma^N} \cdot \mathbf{q}_\varsigma = 0 \tag{2.90}$$

Putting Equation 2.88 and Equation 2.89 in Equation 2.90, we get

$$\sum_{\varsigma} \frac{\tau_{\varsigma}^{C}}{\tau_{\varsigma}^{N}} (\mathbf{v}_{\varsigma} \cdot \nabla T) \mathbf{q}_{\varsigma} \frac{\partial n_{\varsigma}^{0}}{\partial T} = \sum_{\varsigma} \frac{\tau_{\varsigma}^{C}}{\tau_{\varsigma}^{N} \tau_{\varsigma}^{R}} \frac{k_B T^2}{\hbar \omega_{\varsigma}} (\mathbf{A} \cdot \mathbf{q}_{\varsigma}) \mathbf{q}_{\varsigma} \frac{\partial n_{\varsigma}^{0}}{\partial T}. \tag{2.91}$$

The τ_{ς}^{R} in the above equation is total resistive scattering rate given by $(\tau_{\varsigma}^{R})^{-1} = (\tau_{\varsigma}^{U})^{-1} + (\tau_{\varsigma}^{PD})^{-1}$

Although the solution of the above equation is linear in the temperature gradient ∇T, its direction is not always the same as that of ∇T. The symmetry of the crystal lattice restricts the allowed directions. If the temperature gradient is applied along the i direction, then only the A_i component is nonzero and can be determined by the equation [76]:

$$\frac{A_i}{\nabla_i T} = \frac{1}{k_B T^2} \frac{\sum_{\varsigma} \hbar \omega_{\varsigma} \tau_{\varsigma}^{C} (\tau_{\varsigma}^{N})^{-1} v_{\varsigma}^{i} q_{\varsigma}^{i} n_{\varsigma}^{0} (1 + n_{\varsigma}^{0})}{\sum_{\varsigma} \tau_{\varsigma}^{C} (\tau_{\varsigma}^{N} \tau_{\varsigma}^{U})^{-1} (q_{\varsigma}^{i})^2 n_{\varsigma}^{0} (1 + n_{\varsigma}^{0})} \tag{2.92}$$

By combining the solution for A_i from Equation 2.92 and the phonon distribution n_{ς} from Equation 2.89, and using Equation 2.83 for the heat current, the thermal conductivity κ can be obtained. This gives the expression for κ as calculated using Callaway's approximate solution to the phonon Boltzmann transport equation (BTE) as [76] :

$$\kappa_{ii} = \kappa_{ii}^{\text{RTA}} + \frac{(I_1^i)^2}{I_3^i} \tag{2.93}$$

with the following expressions [76]:

$$\kappa_{ii}^{\text{RTA}} = \frac{1}{k_B T^2 N V} \sum_{\varsigma} (\hbar \omega_{\varsigma})^2 (v_{\varsigma}^{i})^2 \tau_{\varsigma}^{C} n_{\varsigma}^{0} (1 + n_{\varsigma}^{0}) \tag{2.94}$$

$$I_1^i = \frac{1}{k_B T^2 N V} \sum_{\varsigma} \tau_{\varsigma}^{C} (\tau_{\varsigma}^{N})^{-1} \hbar \omega_{\varsigma} v_{\varsigma}^{i} q_{\varsigma}^{i} n_{\varsigma}^{0} (1 + n_{\varsigma}^{0}) \tag{2.95}$$

$$I_3^i = \frac{1}{k_B T^2 N V} \sum_{\varsigma} \tau_{\varsigma}^{C} (\tau_{\varsigma}^{N} \tau_{\varsigma}^{R})^{-1} (q_{\varsigma}^{i})^2 n_{\varsigma}^{0} (1 + n_{\varsigma}^{0}) \tag{2.96}$$

In the above expressions, κ_{ii}^{RTA} refers to the thermal conductivity calculated using the standard relaxation time approximation (RTA), as given in Equation 2.86.

2.8.3 Debye Approximation: Transition to Continuous Form

In the Debye model, the phonon dispersion relation is assumed to be linear, given by $\omega = v_i q$, where v_i is the constant phonon group velocity for each mode i. Consequently, the phonon group velocity v_i does not vary with wavevector. Summations over discrete

phonon modes ς are replaced by integrals using the Debye density of states, leading to the substitution $\sum_{\varsigma} \rightarrow \int_0^{\omega_D} D(\omega)\, d\omega$, where $D(\omega) = \frac{9N\omega^2}{\omega_D^3}$ [54], and ω_D is the Debye cutoff frequency corresponding to the Debye temperature Θ_D. To facilitate integration, a dimensionless variable $x = \frac{\hbar\omega}{k_B T}$ is introduced, which implies $\omega = \frac{k_B T}{\hbar} x$ and $d\omega = \frac{k_B T}{\hbar} dx$. Additionally, the equilibrium phonon occupation function satisfies $n^0(1 + n^0) = \frac{e^x}{(e^x - 1)^2}$. Given the linear dispersion, the phonon wavevector for mode i is expressed as $q_{\varsigma}^i = \frac{\omega_{\varsigma}}{v_i}$.

Using the above transformations, and Equation 2.93, the lattice thermal conductivity for i^{th} mode (where $i = LA, TA, or TA'$) is given by [79–81] :

$$k_i = \frac{1}{3}\left(\frac{k_B^4 T^3}{2\pi^2 \hbar^3 v_i}\right)\left[\int_0^{\frac{\Theta_D^i}{T}} \frac{\tau_i^C(x) x^4 e^x}{(e^x - 1)^2} dx + \frac{\left(\int_0^{\frac{\Theta_D^i}{T}} \frac{\tau_i^C(x) x^4 e^x}{\tau_i^N(x)(e^x - 1)^2} dx\right)^2}{\int_0^{\frac{\Theta_D^i}{T}} \frac{\tau_i^C(x) x^4 e^x}{\tau_i^N(x)\tau_i^R(x)(e^x - 1)^2} dx}\right] \tag{2.97}$$

In Equation 2.97, Θ_D^i is the Debye temperature corresponding to the i^{th} mode. This Θ_D^i is given by [82, 83]:

$$\Theta_D^i = \frac{\hbar\omega_i^{max}}{k_B} \tag{2.98}$$

where ω_i^{max} is the maximum phonon frequency for the i^{th} mode.
For normal phonon scattering, the corresponding relaxation time for the longitudinal (τ_{LA}^N) and transverse acoustic ($\tau_{TA}^N / \tau_{TA'}^N$) modes are [79–81]:

$$\frac{1}{\tau_N^{LA}(x)} = \frac{k_B^3 \gamma_{LA}^2 V_a}{M_a \hbar^2 v_{LA}^5}\left(\frac{k_B}{\hbar}\right)^2 x^2 T^5 \tag{2.99}$$

$$\frac{1}{\tau_{TA/TA'}^N} = \frac{k_B^4 \gamma_{TA/TA'}^2 V_a}{M_a \hbar^3 v_{TA/TA'}^5}\left(\frac{k_B}{\hbar}\right) x T^5 \tag{2.100}$$

where $\gamma_i = \sqrt{< \left(\gamma_i^k\right)^2 >}$ is the mode averaged Gruneissen parameter, M_a is the average atomic mass per unit cell and V_a is the average volume per atom.

In most crystalline solids the dissipative scattering is primarily due to Umklapp processes and the corresponding relaxation time (τ_i^U) for the i^{th} mode is given by [79–81] :

$$\frac{1}{\tau_i^U(x)} = \frac{\hbar\gamma^2}{M_a v_i^2 \Theta_D^i}\left(\frac{k_B}{\hbar}\right)^2 x^2 T^3 e^{-\frac{\Theta_D^i}{3T}} \tag{2.101}$$

Hence, for the systems in which only N and U processes are only source of scattering, the total phonon scattering rate ($\frac{1}{\tau^C}$) is given by:

$$\frac{1}{\tau^C} = \frac{1}{\tau^N} + \frac{1}{\tau^U} \tag{2.102}$$

In disordered solids, significant mass and strain field fluctuations can occur at the same Wyckoff position due to the presence of two or more atomic species with differing atomic masses and radii. As a result, propagating phonons are expected to be scattered by these point defects, which arise from such mass and strain field variations. To accurately compute the scattering rates for these dissipative processes, it is therefore necessary to account for the effects of both mass and strain field fluctuation scattering. Using the formalism developed by Klemens [84], the relaxation times for mass fluctuation scattering (τ_i^M) and strain field fluctuation scattering (τ_i^S) are given by:

$$\frac{1}{\tau_i^M} = \left(\frac{V_a k_B^4}{4\pi\hbar^4 v_i^3}\right) x^4 T^4 \Gamma_M, \quad \frac{1}{\tau_i^S} = \left(\frac{V_a k_B^4}{4\pi\hbar^4 v_i^3}\right) x^4 T^4 \Gamma_S \tag{2.103}$$

where the disordered scattering parameter Γ_M and Γ_S are given by :

$$\Gamma_M = \frac{\sum_{j=1}^n c_j \left(\frac{\overline{M_j}}{\overline{\overline{M}}}\right)^2 f_j^1 f_j^2 \left(\frac{M_j^1 \text{ - } M_j^2}{\overline{M_j}}\right)^2}{\sum_{j=1}^n c_j}, \quad \Gamma_S = \frac{\sum_{j=1}^n c_j \left(\frac{\overline{M_j}}{\overline{\overline{M}}}\right)^2 f_j^1 f_j^2 \epsilon \left(\frac{r_j^1 \text{ - } r_j^2}{\overline{r_j}}\right)^2}{\sum_{j=1}^n c_j} \tag{2.104}$$

Here, ϵ is a phenomenological adjustable parameter that depends on the Gruneisen parameter γ and the Poisson ratio ν. Its value has been estimated in [85] and was used in the reference [86] for half-Heusler systems. The expression for ϵ is given by:

$$\epsilon = \frac{2}{9}\left(\frac{6.4\gamma\,(1+\nu)}{1 \text{ - } \nu}\right)^2, \quad where \quad \nu = \frac{1 \text{ - } 2\left(\frac{v_T}{v_L}\right)^2}{2 \text{ - } 2\left(\frac{v_T}{v_L}\right)^2} \tag{2.105}$$

Here c_j represents the relative site degeneracy, f_j denotes the fractional occupation, $\overline{M_j}(\overline{r_j})$ is the average mass (average atomic radius) at the site j, and $\overline{\overline{M}}$ is the average atomic mass of the compound. We note that these corrections have been successfully applied to half-Heuslers previously [83, 87]. Consequently, the total relaxation time for the i^{th} mode of the different structures of the double Heuslers is given by :

$$\frac{1}{\tau^C} = \frac{1}{\tau^N} + \frac{1}{\tau^U} + \frac{1}{\tau^M} + \frac{1}{\tau^S} \tag{2.106}$$

2.9 Generation of structures using the Monte Carlo special quasirandom structure method

To construct optimal periodic supercells that closely approximate a truly disordered structure, the objective is to match the cluster correlation functions $\rho_\alpha(\sigma)$ of a given atomic configuration σ with those of an ideally random structure. In this context, a configuration σ is defined by an array of site variables σ_i, each representing the occupancy of lattice site i. For systems where all sublattices are binary, each site i can take a value of either 0 or 1, corresponding to the type of atom occupying that site. A cluster α consists of a specific group of lattice sites considered in evaluating a given correlation function. The cluster correlation $\rho_\alpha(\sigma)$ quantifies the average product of the site variables within cluster α, and the goal is to reproduce these values as closely as possible to those of the fully disordered limit [88]. This cluster correlation is defined as :

$$\rho_\alpha(\sigma) = \left\langle \prod_i \gamma_{\alpha,M_i}(\sigma_i) \right\rangle \tag{2.107}$$

Here, M_i represents the number of distinct chemical species that can occupy site i. For a binary sublattice, $M_i = 2$. The cluster function $\gamma_{\alpha_i,M_i}(\sigma_i)$ takes the following values:

$$\gamma_{0,2}(0) = 1, \quad \gamma_{0,2}(1) = 1, \quad \gamma_{1,2}(0) = \text{-}1, \quad \gamma_{1,2}(1) = 1,$$

as defined in the ATAT software [89]. The average is taken over all clusters that are symmetry-equivalent to the cluster α, and the product runs over all sites i contained in the cluster. The occupation variable σ_i is defined as either 0 or 1, depending on which element occupies site i in cluster α. In the fully disordered limit, where the occupation of each site is statistically independent, the correlation function $\rho_\alpha(\sigma^{\text{dis}})$ is given by [88].

$$\rho_\alpha(\sigma^{dis}) = \left\langle \prod_i \gamma_{\alpha,M_i}(\sigma_i) \right\rangle = \prod_i \langle \gamma_{\alpha,M_i}(\sigma_i) \rangle \tag{2.108}$$

In the context of present binary sublattices, where each site is evenly occupied by two

types of elements, this correlation amounts to zero across all clusters.

To generate special quasi-random structures (SQS) satisfying the target correlation constraints, all supercells containing the specified number of atoms were first enumerated. In the initial step, atomic species were randomly assigned to lattice sites within each supercell based on the desired composition of each sublattice. For each candidate supercell configuration, two-point and three-point clusters—up to several nearest neighbors—were systematically identified. The correlation deviation for each cluster α was computed as:

$$\Delta\rho_\alpha(\sigma) = \rho_\alpha(\sigma) \text{ - } \rho_\alpha(\sigma^{\text{dis}}),$$

where $\rho_\alpha(\sigma)$ is the cluster correlation for the given structure, and $\rho_\alpha(\sigma^{\text{dis}})$ corresponds to that of a fully disordered (random) state. An objective function, Q, was then evaluated for each structure by summing the squared deviations of these correlations. The structure with the lowest value of the objective function was selected as the optimal SQS. The objective function is defined as [88]:

$$Q = \text{-}L + \sum_{\alpha \epsilon A} |\Delta\rho_\alpha(\sigma)| \tag{2.109}$$

Here L is the largest diameter for which $\Delta\rho_\alpha(\sigma) = 0$ for all clusters α and summation is over all the specified clusters.

In the subsequent phase of the algorithm, a new supercell configuration was generated by randomly selecting one of the previously constructed supercells and performing a permutation between two atoms belonging to the same sublattice. The selection process was guided by the Metropolis algorithm, which probabilistically accepts or rejects new configurations based on their quality. After applying the permutation, the objective function was evaluated for the new supercell. If the resulting objective function value was lower than that of the current best special quasi-random structure (SQS), the new configuration was accepted as the updated best SQS. Otherwise, the previous best SQS was retained. This procedure was repeated iteratively, gradually refining the atomic arrangement. The process continued until a supercell configuration was found that significantly minimized the objective function, indicating a close match to the correlation properties of a fully disordered structure.

Chapter 3

Entropy-stabilized ZrHfCoNiSnSb half-Heusler alloy for thermoelectric applications: a theoretical prediction [2]

3.1 Introduction

Half-Heusler alloys are one class of intermetallic compounds that exhibit great promise as thermoelectric materials suitable for high-temperature applications owing to their remarkable attributes, including a high Seebeck coefficient, exceptional mechanical strength, and thermal stability. On the contrary, the increased lattice thermal conductivity of these materials poses a disadvantage for thermoelectric applications. These compounds, having a composition of XYZ where X (Wyckoff position 4b(0.5, 0.5, 0.5)) and Y (Wyckoff position 4c(0.25, 0.25, 0.25)) are transition metals and Z (Wyckoff position 4a(0, 0, 0)) is a p-block element, comprise of three interlocking face-centred cubic sublattices and an additional vacant sublattice in the same cubic structure. The semiconducting properties and stability of half-Heusler compounds can be understood using the Zintl concept [90], according to which the most electropositive element, X, acts as a cation and donates all of its valence electrons to the tetrahedrally bonded YZ sublattice, effectively forming the anionic part of the structure. Based on this concept, a half-Heusler compound with a valence electron count (VEC) of 18 may be a stable semiconductor with potential for thermoelectric applications. TiNiSn [6, 91], ZrNiSn [6, 91], HfNiSn [6, 92], TiCoSb [7, 93], ZrCoSb [7, 93] and HfCoSb [7, 93] are some of the well-studied VEC 18 half-Heuslers for thermoelectric applications. The crystal structure of half-Heusler alloy XYZ is shown in Fig. 3.1

To overcome the issue of lattice thermal conductivity, a potential solution involves

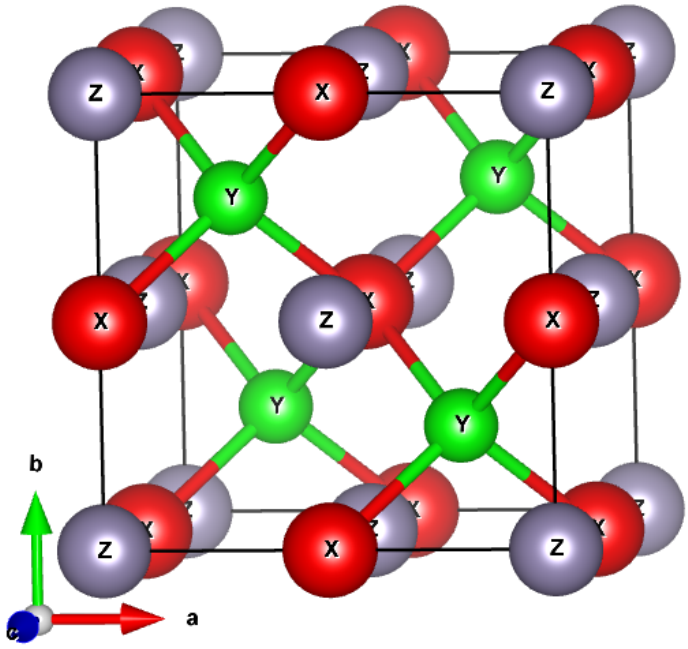

Figure 3.1: Crystal structure of half-Heusler alloy XYZ.

inducing mass disorder at lattice sites by blending the elemental compositions of two or more half-Heusler (HH) alloys, thereby forming a high-entropy alloy. The concept of high entropy has been applied to various classes of materials, including chalcogenides [94, 95] and oxides [96, 97]. In these systems, a high configurational entropy favors the formation of a single-phase structure by contributing significantly to the Gibbs free energy [98]. Compared to conventional solid solutions with low levels of elemental additions, the high-entropy effect can overcome limitations in solubility. This was demonstrated by the successful synthesis of a single-phase (MgCoNiCuZn)O compound with a rock-salt structure [97], which can be viewed as an equimolar mixture of MgO, CoO, NiO, CuO, and ZnO. In this system, the typical solubility limits of binary combinations such as MgO–ZnO and CuO–NiO were surpassed due to entropic stabilization. Among half-Heusler compounds, the high-entropy concept has also been successfully applied in the synthesis of a single-phase (TiZrHfVNbTa)$Fe_{0.5}Co_{0.5}Sb$ [35], which is based on six VEC 18 half-Heuslers: TiCoSb, ZrCoSb, HfCoSb, VFeSb, NbFeSb, and TaFeSb. Similarly, stabilization of the VEC 17.5 half-Heusler compound ZrTiNiFeSnSb [99] is achieved through the high-entropy effect, despite the individual instability of its VEC 17 and VEC 19 parent phases. Another notable example, though not a high-entropy alloy, is the synthesis of Ti_2NiCoSnSb [100], which can be regarded as an equimolar mixture of the

parent HHs TiNiSn and TiCoSb. This alloy has a lattice thermal conductivity of 7 $Wm^{-1}K^{-1}$ as compared to 24 $Wm^{-1}K^{-1}$ for TiCoSb [93] and 13 $Wm^{-1}K^{-1}$ for TiNiSn [6] at room temperature. However, its power factor is significantly reduced as compared to parent compounds, leading to the low value of the figure of merit. Intriguingly, the question arises as to whether it is feasible to synthesize a material by combining the compositions of two half-Heusler compounds with reduced lattice thermal conductivity while retaining the power factor of the original parent compounds. The investigation also seeks to ascertain the stability of this mixed compound in comparison to its parent compounds. Additionally, it will be interesting to understand how the blending process influences the electronic transport properties of this composite material.

The compound ZrHfCoNiSnSb can be regarded as a combination of ZrNiSn/HfNiSn and HfCoSb/ZrCoSb. Our present results indicate that this compound is dynamically stable and is likely to be synthesized at elevated temperatures. The calculated lattice thermal conductivity at 300 K is 5.40 W,$m^{-1}K^{-1}$, which is significantly lower than that of the parent compounds. Moreover, for the n-type case, the computed power factor lies between those of the constituent parent compounds, resulting in a predicted zT of 1.00 at 1100 K.

3.2 Computational details

The calculations were carried out using plane-wave density functional theory (DFT) based calculations as implemented in the Quantum ESPRESSO [101, 102] software. The electron-ion interactions were described using ultrasoft pseudopotentials. For the wavefunction (charge density), we have used a basis set whose size corresponds to a kinetic energy cutoff of 60(480) Ry. The electron-electron exchange and correlation effects were treated using the Perdew-Burke-Ernzerhof (PBE) [50] parametrization of the generalized gradient approximation (GGA). For electronic calculations, the Brillouin zone (BZ) was sampled with a shifted $10 \times 10 \times 10$ and $6 \times 6 \times 6$ Monkhorst-pack k-mesh for the conventional unit cell of the parent compounds and ZrHfCoNiSnSb, respectively. To compute the density of states (DOS) and the electronic transport properties we have used $20 \times 20 \times 20$ k-mesh grid for the parent compounds and $18 \times 18 \times 18$ k-mesh grid for ZrHfCoNiSnSb. Since spin-orbit interaction has a negligible effect in the HEA (as evident from the band structure shown in Figure A.3 of Appendix A), it was not included in the DFT calculations.

To study the dynamical stability, vibrational properties, and lattice thermal conductivity, the phonons were computed using density functional perturbation theory [64]. The

calculations were performed on a $6 \times 6 \times 6$ q-mesh for the primitive unit cell of the parent compounds and a $3 \times 3 \times 3$ q-mesh for ZrHfCoNiSnSb.

Electronic transport properties were calculated using semi-classical Boltzmann transport theory under the constant relaxation time and rigid band approximations. Within this approach, transport properties per unit relaxation time were first computed using the BoltzTraP2 code [68], and the constant electronic relaxation time τ_{av} was then estimated using deformation potential theory [103]. The complete methodology is described in Section 2.7 of Chapter 2.

3.3 Results and discussions

3.3.1 Structure, thermodynamic stability and bonding

To model the most disordered configuration of ZrHfCoNiSnSb, we employed the Monte Carlo Special Quasirandom Structure (McSQS) method, as implemented in the ATAT software [88]. The quasirandom structures were generated with the constraint that the Zr and Hf atoms occupy the Wyckoff site 4b (0.5, 0.5, 0.5), Ni and Co atoms occupy the site 4c (0.25, 0.25, 0.25) and Sn and Sb atoms occupy the site 4a (0, 0, 0). We constructed four different quasirandom structures within this constraint. In the construction of the SQS structures, pair correlation functions were included up to the fourth nearest-neighbor distance, while triplet correlations were considered up to the third nearest-neighbor distance. Three of these structures are the 12-atom structure in the conventional cubic HH supercell (Type I), the 24-atom quasirandom structure with the conventional cubic cell doubled along the c- direction (Type II), and the 24-atom quasirandom structure with a $2\times2\times2$ primitive fcc supercell (Type III). Additionally, we also generated a 24-atom SQS with no constraints on the particular choice of crystal structure (Type IV). The initial structures of these unit cells are shown in Figure A.1 of the Appendix A, while the optimized structures are shown in Fig. 3.2. The corresponding McSQSc transformation matrices for all the generated structures are provided in Equations A.2-A.5 of Appendix A.

On optimizing the lattice parameters and the atomic positions of the above-mentioned unit cells, we find that the Type I structure is the lowest in energy. The relative energies per formula unit of the other structures with respect to that of Type I (ΔE) and the lattice parameters of all the structures are reported in Table 3.1. It is interesting to note that

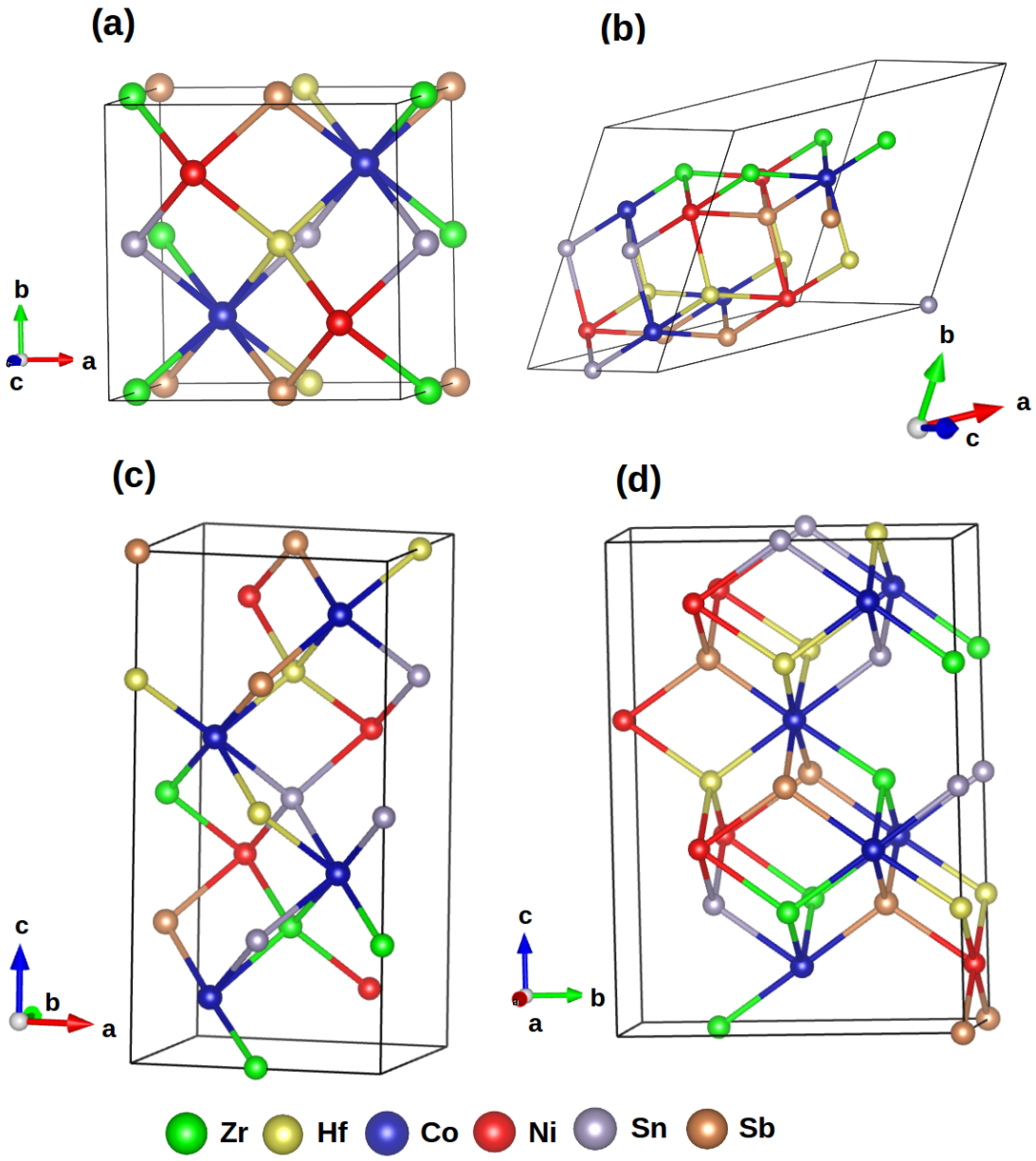

Figure 3.2: Crystal structures of the optimized SQSs: (a) conventional unit cell, (b) $2 \times 2 \times 2$ supercell, (c) double conventional unit cell, and (d) unconstrained SQS with 24 atoms.

post-geometry optimization, the lattice parameters and the angles between the lattice vectors deviate from those observed in the supercells of fcc lattice. For example, in the lowest-energy Type I structure, all three lattice vectors are equal, and the interaxial angles are 90.000° prior to geometry optimization. After optimization, the structure relaxes into a

monoclinic phase characterized by the C_2 point group which includes only the identity and a 180° rotation about the Z-axis as its symmetry operations, due to slight variations in the lattice parameters and a deviation of the angle γ from 90.000°. Since Type I is the lowest energy structure amongst the ones considered in this study, all subsequent calculations for ZrHfCoNiSnSb were performed using this unit cell. To assess whether the Type I structure accurately captures the extensive disorder, a convergence analysis was performed by comparing the Type I McSQS with truly disordered 96-atom McSQSs (constructed as a $2 \times 2 \times 2$ supercell of the conventional unit cell). The results of this analysis are presented in Section A.10 of Appendix A. As shown in Figure A.10 of Appendix A, the bond lengths and bond orders—which indicate how charge is distributed between atoms and thus partially characterize the local chemical environment—exhibit excellent agreement between the 12-atom and 96-atom SQS structures. This demonstrates that the 12-atom SQS effectively captures the key features of the extensive configurational disorder present in the larger 96-atom system.

Table 3.1: Computed relative energy per formula unit (ΔE), lattice parameters and angle between the lattice parameters for the different SQS structures considered in this study.

Structure	Type-I	Type-II	Type-III	Type-IV
ΔE (in eV)	0.000	0.028	0.014	0.026
Lattice parameters (in Å)	a = 6.109, b = 6.107, c = 6.115	a = 6.101, b = 6.108, c = 12.199	a = 8.623, b = 8.628, c = 8.626	a = 4.318, b = 8.626, c = 12.204
Angles	$\alpha = \beta = 90.000°$, $\gamma = 90.004°$	$\alpha = 90.006°$, $\beta = 90.001°$, $\gamma = 89.979°$	$\alpha = 60.084°$ $\beta = 60.065°$, $\gamma = 60.075°$	$\alpha = 90.044°$ $\beta = 90.000°$, $\gamma = 90.000°$

These alloys are typically synthesized experimentally via arc melting of the elemental precursors. Hence, to check the stability of the HEA against segregation into the individual bulk components, we have computed their average formation energy (E_f) [104], which is given as:

$$E_f = \frac{E_{\text{ZrHfCoNiSnSb}} - aE_{\text{Hf}} - bE_{\text{Zr}} - cE_{\text{Ni}} - xE_{\text{Co}} - yE_{\text{Sn}} - zE_{\text{Sb}}}{(a+b+c+x+y+z)} \tag{3.1}$$

where $E_{\text{ZrHfCoNiSnSb}}$ is the total energy of the HEA and E_i, i =Hf, Zr, Ni, Co, Sn and Sb, are the energy per atom of the i^{th} element in its bulk. a, b, c, x, y and z are the number of atoms of Hf, Zr, Ni, Co, Sn and Sb, respectively, in the HEA. The conditions used for calculating E_f in the above equation — including the elemental standard states, crystal structures, and temperature — are provided in section A.9 of the Appendix A. We find that

our proposed HEA has a formation energy of -0.75 eV per atom, suggesting that this is highly stable with respect to the segregation into individual atomic phases.

Additionally, the proposed HEA might also be thought of as a mixture of two stable HHs, namely, HfNiSn and ZrCoSb HHs or ZrNiSn and HfCoSb HHs. Hence, it is also imperative to study the stability of the HEA with respect to phase segregation into these HHs. To do so, we considered the following chemical reactions:

$$\text{ZrHfCoNiSnSb} \longrightarrow \text{HfNiSn} + \text{ZrCoSb} \tag{3.2}$$

$$\text{ZrHfCoNiSnSb} \longrightarrow \text{ZrNiSn} + \text{HfCoSb} \tag{3.3}$$

and computed the enthalpy of formation (ΔH_e), which is given by:

$$\Delta H_e = E_{\text{HfNiSn/ZrNiSn}} + E_{\text{ZrCoSb/HfCoSb}} - E_{\text{ZrHfCoNiSnSb}} \tag{3.4}$$

where the first, second and third terms on the right-hand side of Eqn. 3.4 are the total energies of the HHs into which they can phase segregate and HEA, respectively. For reactions A.6 and 3.3, we obtain ΔH_e to be -70 meV and -86 meV per formula unit. While the negative values of ΔH_e might initially suggest that ZrHfCoNiSnSb will phase segregate to either HfNiSn and ZrCoSb or ZrniSn and HfCoSb, the role of configurational entropy (ΔS_{config}) at elevated synthesis temperatures become crucial in reducing the Gibbs free energy and contributing to the overall thermodynamic stability [98] of ZrHfCoNiSnSb over HfNiSn/ZrNiSn and ZrCoSb/HfCoSb. This configurational entropy is given by [35]:

$$\Delta S_{\text{config}} = -k_B \left(\sum_{x=1}^{m} \sum_{i=1}^{n} f_i^x ln\left(f_i^x\right) \right) \tag{3.5}$$

In Eqn 3.5, k_B is the Boltzmann constant. The summation over x runs over all the sublattices (here it is 3) and f_i^x is the fraction of element i in the sublattice x. For the case of ZrHfCoNiSnSb, in Type-I, each of Hf/Zr, Ni/Co, and Sn/Sb forms fcc sublattice. Using Eqn. 3.5, ΔS_{config} for the Type-I structure of the HEA comes out to be 2.079 k_b. The temperature above which this system can be synthesized will be the one at which the change in the Gibbs free energy (ΔG) is positive. This Gibbs free energy difference, ΔG,

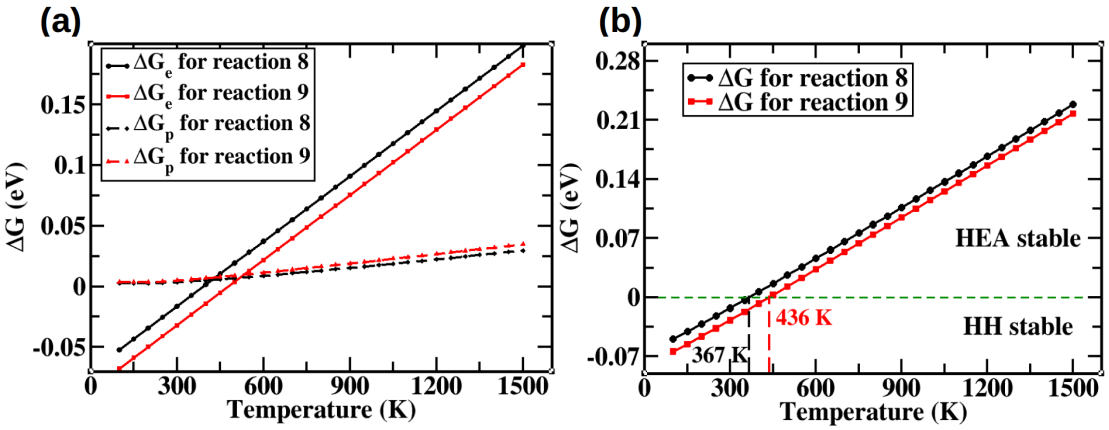

Figure 3.3: (a) Individual components of ΔG as a function of temperature. (b) Total Gibbs free energy as a function of temperature.

is expressed as:

$$\Delta G = \Delta G_e + \Delta G_p \tag{3.6}$$

where the contributions of electronic energy and configurational entropy to the Gibbs free energy, ΔG_e, are given by

$$\Delta G_e = \Delta H_e \text{ - } T\Delta S_{\text{config}} \tag{3.7}$$

and ΔG_p represents the phonon contribution to the Gibbs free energy, defined as:

$$\Delta G_p = \Delta H_p \text{ - } T\Delta S_p \tag{3.8}$$

Here, H_p and S_p denote the phonon energy (or vibrational energy) and phonon entropy (or vibrational entropy) of the respective structures, given by:

$$H_p = \int_0^{\omega_{\max}} g(\omega)\hbar\omega \left(\frac{1}{e^{\hbar\omega/k_BT} \text{ - } 1} + \frac{1}{2} \right) d\omega \tag{3.9}$$

and

$$S_p = \int_0^{\omega_{\max}} g(\omega)k_B \left[\frac{\hbar\omega/k_BT}{e^{\hbar\omega/k_BT} \text{ - } 1} \text{ - } \ln\left(1 \text{ - } e^{\text{ - } \hbar\omega/k_BT}\right) \right] d\omega \tag{3.10}$$

In these expressions, $g(\omega)$ represents the phonon density of states corresponding to the frequency ω, and $\omega_{\max}$ is the maximum phonon frequency.

Fig. A.10 illustrates the variation of ΔG with temperature for the cases described in Equations A.6 and 3.3.

As can be seen from the Fig. A.10, ΔG is positive when T is greater than 367 K and 436

K for reactions A.6 and 3.3, respectively. We note that these temperatures are only 67 K and 136 K above room temperature, and are much lower than the synthesis temperatures of half-Heusler systems. Thus, our analysis suggests that these materials will be stable towards segregation into the HHs. A more detailed discussion on segregation kinetics and the potential formation of secondary phases is provided in Section A.11 of the Appendix A.

At this point, it would be interesting to compare the local geometry of this HEA with those of conventional HHs. A conventional HH can be thought of as a combination of two zinc blend structures formed by the YZ elements and the XY elements. In each of the zinc blende structures, the Y element is at the centre of the tetrahedra formed either by the X or the Z element. Moreover, these are perfect tetrahedra, i.e., in each tetrahedra, the four Y-Z or Y-X bonds have the same bond lengths. In contrast, for the HEA, the introduction of the disorder at each of the atomic sites distorts these tetrahedra because two of the vertices are occupied by Hf (Sb) while the other two by Zr (Sn). In ZrNiSn and HfNiSn, the Ni-Sn bond lengths are 2.665 Å and 2.647 Å, respectively, while in the HEA we find the bond length to be 2.656 Å. Similarly, the Co-Sb bond length in HEA is 2.625 Å which is slightly shorter (similar) than (to) that of 2.642 Å (2.624 Å) in ZrCoSb (HfCoSb). Moreover, we also observe formation of new Ni-Sb and Co-Sn bonds with bond lengths of 2.625 Å and 2.662 Å , respectively. In the X-Y sublattice of the HEA, the Zr-Ni (Zr-Co) bonds are elongated (shortened) compared to those observed in ZrNiSn and ZrCoSb ($d_{\text{Zr-Ni}}$=2.688 Å in HEA vs 2.665 Å in ZrNiSn; $d_{\text{Zr-Co}}$=2.609 Å in HEA vs. 2.642 Å in ZrCoSb). In contrast, both the Hf-Ni and Hf-Co bonds in HEA are shortened compared to those observed in the parent HHs. However, the Zr-Ni (Zr-Co) bond is elongated (shortened) than that observed in ZrNiSn (ZrCoSb). These asymmetries in the local geometry result in deviation from the cubic symmetry. Further, such a wide variation of bond lengths suggests that there is significant heterogeneity in terms of bonding and bond strength in the HEA, the implications of which on the thermoelectric properties are discussed later.

In order to understand the nature of the bonding between the different elements in the HEA, we have computed the difference between the charge density distribution and superposition of the atomic densities ($\Delta\rho$) for the HEA and the parent compounds. $\Delta\rho$ provides information as to how the atomic charge densities are rearranged when the different elements interact to form a compound. Fig. 3.4 shows the $\Delta\rho$ for the HEA, while those for the parent compounds are shown in Figure A.5 of the Appendix A. In the Co-containing

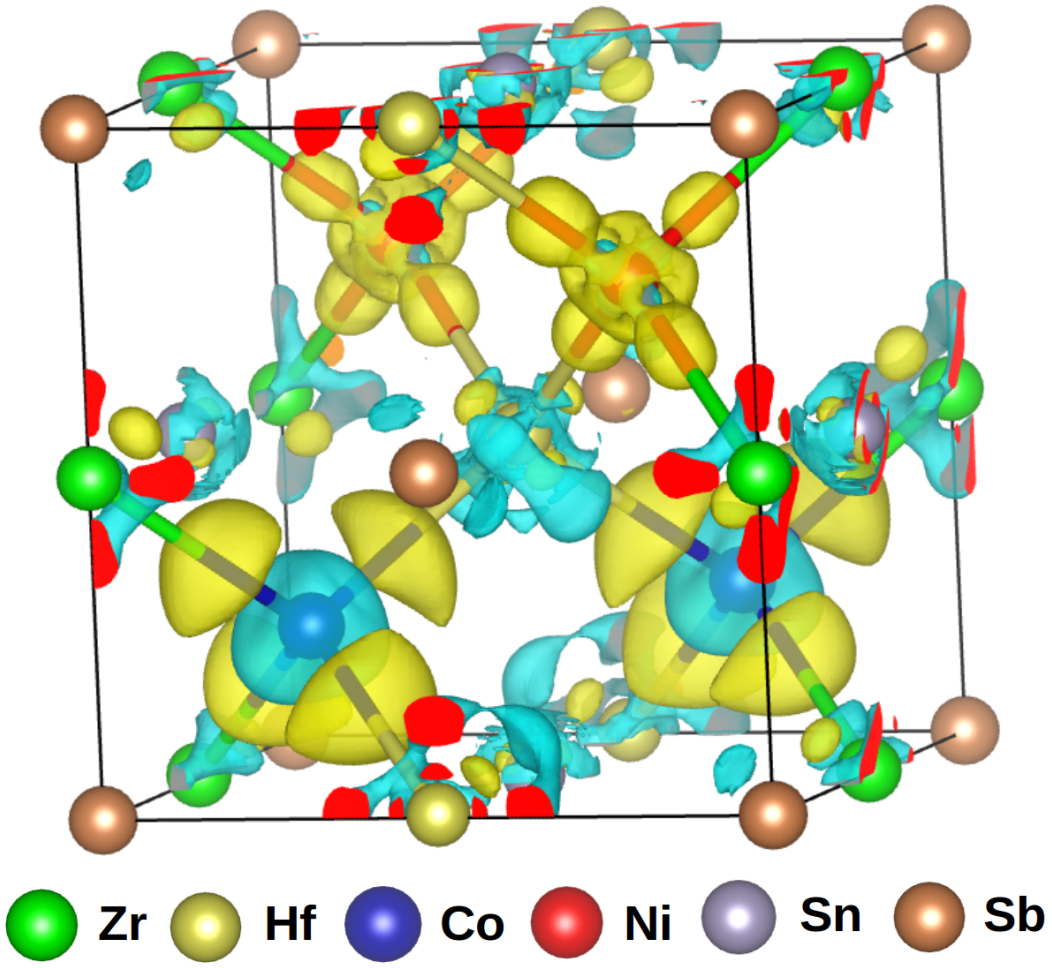

Figure 3.4: Isosurfaces of charge density difference ($\Delta\rho$) between the electron density of the HEA and that obtained from the superposition of the atomic densities. Yellow (Turquoise) isosurfaces denote accumulation (depletion) of charge density. The isosurfaces correspond to an isovalue of 0.009 e Bohr^{-3}

parent compounds, namely ZrCoSb and HfCoSb, we observe that there is charge depletion from the Co atom (Turquoise isosurfaces in Figure A.5 (b) and (d) of Appendix A). Further, both charge depletion and accumulation can be observed around the Hf/Zr atoms, with the former dominating. Charge depletion is also observed around Sb. Importantly, we observe charge accumulation in between the Zr/Hf and Co bonds, suggesting a covalent nature of bonding between them. No such charge accumulation is observed between the Co-Sb bonds. Similarly, in the Ni-containing compounds, i.e., in ZrNiSn and HfNiSn, we primarily observe charge depletion around Zr/Hf and Sn. However, in contrast with Co, we

observe both accumulation and depletion of charges from Ni, with the former dominating. Additionally, charge accumulation is also observed along the Ni-Zr/Hf bonds. The charge cloud, in this case, is more directional compared to the Co-containing HH and is localized closer to the Ni atom. Thus, in the Ni (Co) containing parent compounds, the X-Y bond is ionic (covalent) in nature. Interestingly, in the HEA, the electron rearrangement around the Ni and Co atoms remains similar to the parent compounds with slight deviations due to local distortion in its structure. This shows the presence of a bonding hierarchy in the HEA.

3.3.2 Phonon dispersion and Lattice thermal conductivity

In order to assess the dynamical stability of the HEA, we have computed its phonon spectrum, which is shown in Fig. 3.5. Further, in order to understand how the lattice vibrations are altered in the HEA in comparison with the parent HHs, we have also computed the phonon spectra of the latter (Fig. 3.5 (c)-(f)). Since both the parent compounds and the HEA lack a center of inversion, LO-TO splitting corrections were included in all phonon calculations. The absence of any imaginary modes in the HEA vibrational spectrum throughout the BZ suggests that the HEA is dynamically stable. A LO-TO splitting of approximately 25 cm^{-1} was observed in ZrNiSn and HfNiSn, around 50 cm^{-1} in HfCoSb and ZrCoSb, and about 21 cm^{-1} in the HEA ZrHfCoNiSnSb, as shown in Figure A.12 of Appendix A. Additionally, the Born effective charges—which determine the strength of the coupling between phonons and the macroscopic electric field (the main origin of LO-TO splitting)—were computed and compared with previously reported values [6, 7] in Tables A.11 and A.12 of Appendix A. Our results for the high-frequency dielectric tensor and Born effective charges of the parent HHs are in excellent agreement with previously reported values, as shown in Table A.11 of Appendix A. Compared to the parent HHs, where there is either nil or negligible mixing of the acoustic and optical phonons, the HEA spectrum shows a significant overlap of these phonon modes. This enhanced mixing can be attributed to the softening of the low-frequency optical modes. Usually, this mixing between the heat-carrying acoustic modes with the optical ones results in scattering of the former, thereby reducing the lattice thermal conductivity. Moreover, in the HHs, the high-frequency optical phonon bands are flat, giving rise to sharp peaks in the phonon density of states (PhDOS). In contrast, in the HEA, the optical phonon bands become more dispersive, giving rise to the broader peaks in PhDOS. The atom projected PhDOS show that for the modes that have frequencies less than 125 cm^{-1}, the major contribution

is from the heaviest element Hf. The other heavy elements like Sb, Sn and Zr also have reasonable contributions in lower frequency modes. The Sb and Sn atoms have a dominant contribution to the phonon modes lying between 125 cm^{-1} and 175 cm^{-1}. For $175 < \omega <$ 200 cm^{-1}, the lattice vibrations are dominated by the vibrations of the Zr atoms, while those having frequency beyond 200 cm^{-1}, the major contributions are from the displacements of the lightest Ni and Co atoms.

In order to understand whether the nature of localization of the phonon modes in the HEA changes compared to the HH, we have computed the inverse participation ratio for each mode (IPR). This IPR is computed as [105] :

$$IPR = \sum_{i} \left[\sum_{\alpha} \epsilon_{i\alpha,n} \epsilon^{*}_{i\alpha,n} \right]^{2} \tag{3.11}$$

Here $\epsilon_{i\alpha,n}$ represents the eigenvector component along the α-direction for mode n. $IPR = 1$ ($IPR \simeq 1/N$, N being the number of atoms in the unit cell) implies a completely localized (delocalized) phonon mode. Fig. 3.5 shows the IPR for the HEA as well as the parent compounds. While for the HHs, all the phonon modes till about 130 cm^{-1} are completely delocalized, in HEA the phonon modes with frequency greater than 50 cm^{-1} tends to localize. However, relative to the HHs where we observe that the high-frequency phonon modes are highly localized ($IPR = 1$ for some modes), the overall degree of delocalization of the modes is relatively lower in the HEA suggesting that the modes are more diffusive in nature.

The effect of hierarchical bonding, discussed in the previous section, is reflected in the computed the mode resolved Gruneisan parameter (γ_i^k), which for the phonon of the i^{th} branch with wave vector k is given by:

$$\gamma_i^k = - \frac{V_0}{\omega_i^k} \frac{\partial \omega_i^k}{\partial V} \tag{3.12}$$

where V_0 is the equilibrium volume of the unit cell and ω_i^k is the frequency corresponding to the phonon of the i^{th} branch with wave vector k. The derivative in Equation 4.1 is evaluated numerically by using the central difference method. To achieve this, we computed the phonon spectra by applying strain, varying the lattice parameters by $\pm 1\%$. The γ_i^k of the parent HH and the HEA are plotted in Fig. 3.6. While for the HH γ_i^k typically lies between 0 and 2.5, in the HEA, it varies from -1.4 to 7.4, i.e. an overall spread of 8.8. Moreover, this enhancement in the spread of γ_i^k is primarily restricted to the heat-carrying acoustic

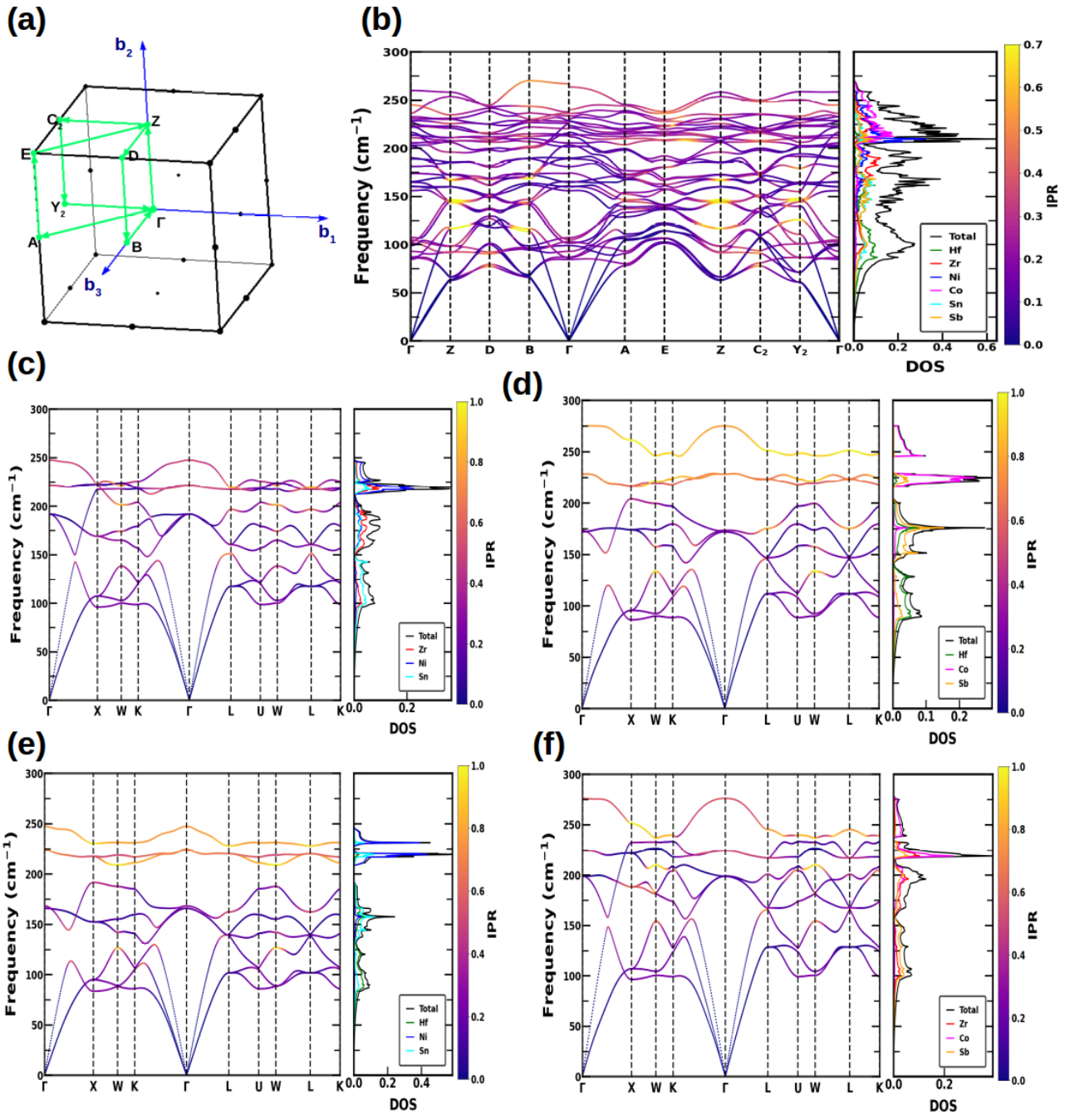

Figure 3.5: (a) Irreducible Brillouin zone showing the path marked in green for the HEA, Phonon dispersion, inverse participation ratio (IPR) of the phonon modes and phonon density of states of (b) ZrHfCoNiSnSb (c) ZrNiSn (d) HfCoSb (e) HfNiSn (f) ZrCoSb .

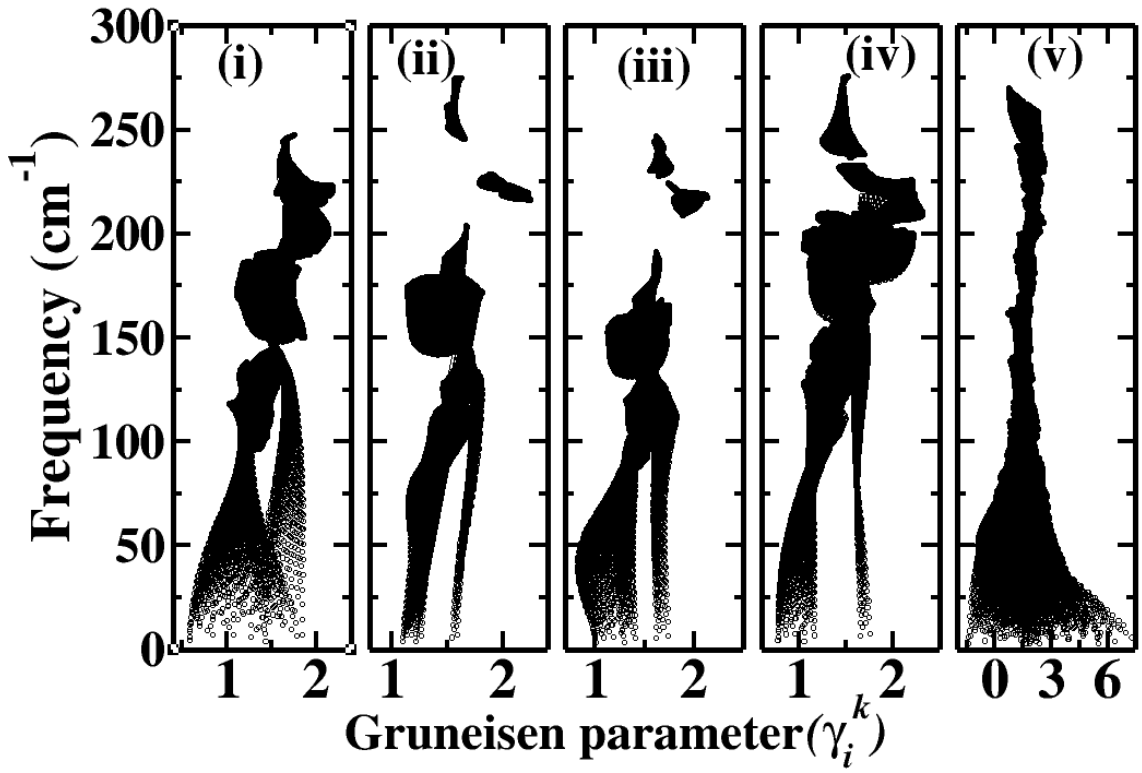

Figure 3.6: Mode resolved Gruneisen parameters for the parent HHs (a) ZrNiSn (b) HfCoSb (c) HfNiSn (d) ZrCoSb and (e) ZrHfCoNiSnSb.

phonons. This suggests that the HEA lattice becomes significantly more anharmonic compared to that of the parent HHs.

The effect of the changes in bonding of the HEA lattice and thereby their vibrational properties also affect thermal transport in these materials. We have computed the lattice thermal conductivity (k_L) for all the systems using the Debye-Callaway model [79, 81, 106]. According to this model, k_L is the sum over the contribution to lattice thermal conductivity from one longitudinal acoustic (k_{LA}) and two transverse acoustic branches (k_{TA} and $k_{TA'}$). The methodology for calculating lattice thermal conductivity is detailed in Section 2.8 of Chapter 2.

In most crystalline solids, the dissipative scattering is primarily due to Umklapp processes hence, for the parent HHs, for i^{th} mode, the total phonon scattering rate $\left(\frac{1}{\tau^C_{HH,i}}\right)$ depends on the scattering rates associated with the normal (N) and the Umklapp (U) processes and is given by:

$$\frac{1}{\tau^C_{HH,i}} = \frac{1}{\tau^N_i} + \frac{1}{\tau^U_i} \tag{3.13}$$

However, in the case of ZrHfCoNiSnSb HEA, significant mass fluctuation (MF) occurs at the Wyckoff position 4b (0.5, 0.5, 0.5), which can now be occupied either by Hf or Zr, the latter having a mass half of that of Hf. Further, the 4a (0, 0, 0) position, which is now occupied by either Sb or Sn will also exhibit mass fluctuations due to their different atomic masses. Hence, we expect that the propagating phonons will be scattered also by these mass defects in HEA caused by these mass fluctuations plays a crucial role in phonon scattering. Hence, to compute the scattering rates for dissipative processes in the HEA, we have also incorporated the effect of mass fluctuation scattering. We note that these corrections have been successfully applied to double HHs previously [83, 87]. Consequently, the total relaxation time for the i^{th} mode of ZrHfCoNiSnSb is given by :

$$\frac{1}{\tau^{C}_{HEA,i}} = \frac{1}{\tau^{N}_{i}} + \frac{1}{\tau^{U}_{i}} + \frac{1}{\tau^{M}_{i}} \tag{3.14}$$

The values of the different parameters used to compute the lattice thermal conductivity are given in Table 3.2.

Table 3.2: Mode resolved Debye temperature (Θ^{i}_{D}), long wavelength phonon velocity (v_i) and Gruneisen parameter (γ_i) for the parent systems and the HEA. The values given in square brackets are from Ref. [5])

Property	ZrNiSn	HfCoSb	HfNiSn	ZrCoSb	ZrHfCoNiSnSb
Θ^{LA}_{D} (K)	217 [214]	210	201 [196]	238	153
Θ^{TA}_{D} (K)	170 [166]	161	147 [145]	185	146
$\Theta^{TA'}_{D}$ (K)	186 [184]	171	160 [160]	200	148
v_{LA} (m/s)	5338 [5323]	5115	4830 [4746]	5746	5224
v_{TA} (m/s)	3080 [2852]	2843	2540 [2508]	3115	2499
$v_{TA'}$ (m/s)	3080 [3600]	2843	2540 [3120]	3115	2683
γ_{LA}	1.46 [1.69]	1.62	1.53 [1.55]	1.54	1.41
γ_{TA}	1.22 [1.30]	1.36	1.28 [1.35]	1.23	1.45
$\gamma_{TA'}$	1.27 [1.36]	1.43	1.41 [1.38]	1.25	1.58
γ	1.61 [1.71]	1.64	1.59 [1.59]	1.59	1.70

Fig. 3.7 shows the lattice thermal conductivity of the HHs and the HEA. Since the lattice thermal conductivity is primarily governed by acoustic phonon modes—while optical modes contribute minimally due to their low group velocities—the parameter reported in Table 3.2 is largely influenced by the acoustic modes. Consequently, as the Debye–Callaway model accounts only for acoustic contributions, the LO-TO splitting corrections have a negligible effect on the lattice thermal conductivity, as illustrated in Figure A.13 of Appendix A. We observe that at 300 K the k_L of the HHs lie between 20.37

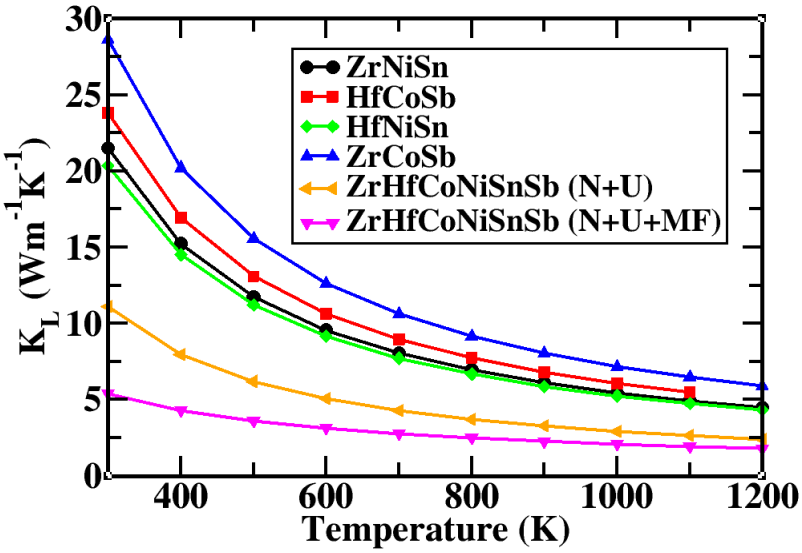

Figure 3.7: Lattice thermal conductivity as a function of temperature. N, U and MF represent Normal, Umklapp and Mass fluctuation scattering processes.

and 28.65 $Wm^{-1}K^{-1}$ with HfNiSn (ZrCoSb) having the lowest (highest) value. We note that our computed values of k_L is in reasonably good agreement with those reported in the literature using the solutions of the semiclassical Boltzmann transport equations for phonons that are more computationally demanding but accurate [6, 7, 107]. For all the systems, the lattice thermal conductivity is reduced with an increase in temperature. For the HEA, when we compute the lattice thermal conductivity by including only the Umklapp scattering, we obtain a value of 11.03 $Wm^{-1}K^{-1}$ at 300 K. We note that this is less than half of the values observed in the HHs. This drastic reduction in lattice thermal conductivity can be attributed to the different types of chemical bonding observed in the HEA lattice that resulted in enhanced anharmonicity. On incorporation of the scattering effects due to mass fluctuations, the lattice thermal conductivity is further reduced to 5.40 $Wm^{-1}K^{-1}$ at 300 K. Thus, our results suggest that the synergistic effect of the changes in bonding in the HEA lattice and the mass fluctuations can drastically reduce k_L. At room temperature, the k_L of the HEA is reduced by a factor of three compared to the parent HHs Hf/ZrNiSn, and by a factor of five compared to Zr/HfCoSb. Interestingly, in line with the findings reported by Anand et al. [108] for double Heusler alloys, the HEA ZrHfCoNiSnSb exhibits lattice thermal conductivity values that are comparable to those of double Heusler compounds with the lowest k_L. In fact, its lattice thermal conductivity is lower than that of most double Heusler systems discussed in the same reference.

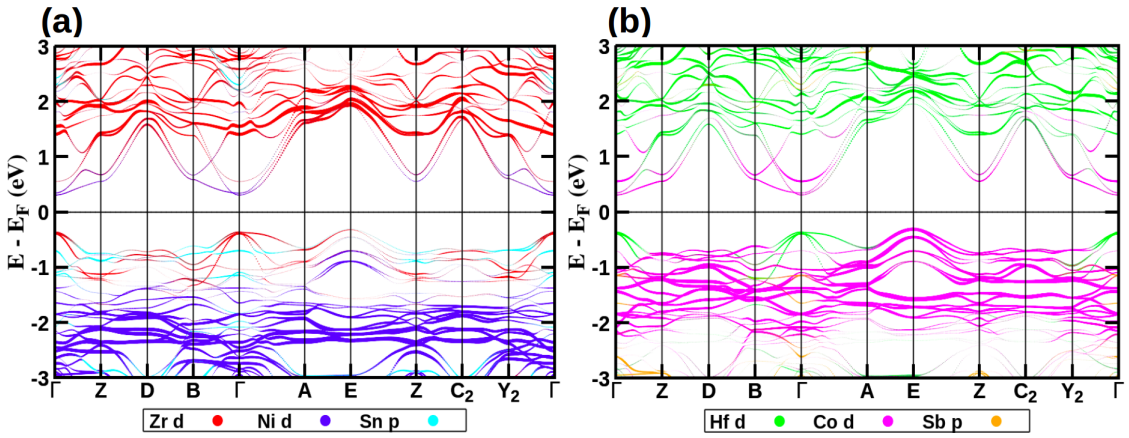

Figure 3.8: Band structure of HEA showing contributions from (a) Zr-d (red), Ni-d (blue), and Sn-p (turquoise) orbitals (b) Hf-d (green), Co-d (pink), and Sb-p (orange) orbitals.

3.3.3 Electronic properties

Fig. 3.8 shows the band structure of ZrHfCoNiSnSb, along with the contributions from the d-states of the transition metals and the p-states of the p-block elements. Those for the parent HHs are shown in Figure A.4 of Appendix A. In accordance with the literature report, we observe that all the HHs are semiconducting in nature, with HfCoSb having the largest band gap of 1.12 eV [7], followed by 1.05 eV for ZrCoSb [7], 0.51 eV for ZrNiSn [6] and 0.40 eV for HfNiSn [6] . The conventional unit cell of these HHs have the conduction band minima (CBM) at the Γ point of the BZ. However, their valence band maxima (VBM) occurs at different points of the BZ. Similar to the CBM, the VBM of ZrNiSn and HfNiSn is at the Γ point of the BZ, making these two HHs as a direct band gap semiconductor. In contrast, ZrCoSb has VBM at the R point of the BZ making it an indirect band gap semiconductor. In the case of HfCoSb, there are two degenerate VBMs, namely at Γ and the R point of the BZ. Additionally, the VB and CB edges of Zr/HfNiSn are closer to the Fermi energy than those of Zr/HfCoSb. The band structure characteristics of the corresponding primitive unit cell, obtained using the unfolding technique [109], are presented in Section A.13 of Appendix A.

Similar to the HHs, the CBM of the HEA is at the Γ point of the BZ while the VBM is at E-point (Fig. 3.8). Since the lattice parameters of this monoclinic lattice are very close and the deviation of the γ from 90° is negligibly small, the E point of the BZ of this monoclinic lattice is the same as that of the R-point of the BZ of the cubic lattice. The HEA is an indirect semiconductor with a band gap of 0.61 eV, which is less than that of

the Zr/HfCoSb and more than that of Zr/HfNiSn. Additionally, the maxima of the valence band at the $\Gamma-$point is only 60 meV below the VBM, suggesting that at high temperatures, p-type carriers belonging to this hole pocket will also contribute to the transport properties. We note that these features of the valence band are very similar to those observed in ZrCoSb (Figure A.4 (e) of Appendix A) and HfCoSb (Figure A.4(c) of Appendix A). Furthermore, the conduction band of the HEA have additional electron pockets at the B and Z points of the BZ. These are about 280 and 250 meV higher in energy compared to the CBM. These high symmetry points of the BZ of the HEA are analogous to the X-point of the cubic BZ of the HHs. While the VBM at E-point have contributions from Co-d states, the hole pocket at the Γ point has a contribution from Zr and Hf-d states (Figure 3.8 and Figure A.4(a) of Appendix A). The Ni-d states lie deep inside the valence band. This is in contrast to that observed in Hf/ZrNiSn, where Ni-d orbitals contributed to hole pockets at the R-point of the cubic BZ. The CBM at Γ and the electron pockets at B and Z-points in the BZ of the HEA have contributions from the d-orbitals of all the transition metal elements.

3.3.4 Carrier relaxation times

The average relaxation time (τ_{av}) of charge carriers in these materials was calculated using deformation potential theory [103], as described in Section 2.7 of Chapter 2. This approach considers only scattering due to acoustic phonons. The conductivity and density-of-states (DOS) effective masses at various band extrema in the Brillouin zone (BZ), which are used in the relaxation time calculations, are listed in Tables A.2 to A.7 in Appendix A for both the parent half-Heuslers (HHs) and the high-entropy alloy (HEA).

This average relaxation time (τ_{av}) was calculated by including all electronic bands located within 150 meV above CBM (for electrons) and 150 meV below the VBM (for holes). The quantities required to compute τ_{av} using the above equations and the values of τ_{av} and μ_{av} for electrons and holes at 300 K for all the compounds are given in Tables 3.3 and 3.4, respectively. It is observed that all the parent HHs, except HfCoSb, the average conductivity effective mass of electrons is greater than that of holes. In contrast, for the HEA HHs $m^*_{\sigma,av}$ of electrons are smaller than that of holes. Further, we observe that the magnitude of the deformation potential of electrons and holes, which is a measure of the coupling between the charge carriers and acoustic phonons are similar. However, we find that $|\Xi|$ of electrons for all the compounds are larger than that observed in holes. This suggests that in these materials, the electron-acoustic phonon coupling is larger than that between holes and acoustic phonons.

Table 3.3: Average conductivity effective mass ($m^*_{\sigma,av}$), deformation potentials ($|\Xi|$), elastic constants (C), average mobility (μ_{av})and average relaxation time (τ_{av}) for electrons in the different materials. The values of μ_{av} and τ_{av} reported in the table had been computed at 300 K.

Property	ZrNiSn	HfCoSb	HfNiSn	ZrCoSb	ZrHfCoNiSnSb
$m^*_{\sigma,av}$	2.13	4.37	2.10	3.46	0.92
$\|\Xi\|$ (eV)	16.12	15.51	16.20	15.42	15.75
C (GPa)	233	275	242	264	247
μ_{av} (cm^2/Vs)	42.8	6.65	48.17	7.47	60.02
τ_{av} (fs)	51.73	16.52	57.61	14.72	31.45

Table 3.4: Average conductivity effective mass ($m^*_{\sigma,av}$), deformation potentials ($|\Xi|$), elastic constants (C), average mobility (μ_{av})and average relaxation time (τ_{av}) for holes in the different materials. The values of μ_{av} and τ_{av} reported in the table had been computed at 300 K.

Properties	ZrNiSn	HfCoSb	HfNiSn	ZrCoSb	ZrHfCoNiSnSb
$m^*_{\sigma,av}$	0.75	5.74	0.61	1.54	1.27
$\|\Xi\|$ (eV)	15.51	14.82	15.70	14.84	15.17
C (GPa)	233	275	242	264	247
μ_{av} (cm^2/Vs)	153.3	8.33	241.68	3.91	5.30
τ_{av} (fs)	65.23	27.20	83.61	3.41	3.83

Fig. 3.9 shows the variation of τ_{av} as a function of temperature. We find that τ_{av} of electrons in the HEA is smaller (larger) than that in ZrNiSn and HfNiSn (ZrCoSb and HfCoSb). For the holes, we find that while τ_{av} of the HEA is larger than that observed in ZrCoSb, it is smaller than that observed in the other parent HHs, namely ZrNiSn, HfCoSb and HfNiSn.

3.3.5 Electronic transport calculation

Full electronic transport calculations were performed by combining the Boltzmann transport equation with a constant relaxation time approximation and a relaxation time derived from the deformation potential theory. Fig. 3.10 (a)-(d) illustrates the variation in the electronic transport properties of ZrHfCoNiSnSb with carrier concentration, ranging from 10^{19} to 10^{22} cm^{-3}, at different temperatures. The Seebeck coefficient exhibits an initial increase followed by a decrease at elevated temperatures as the carrier concentration increases. With increasing temperature, the peak position shifts towards higher carrier concentrations while the peak magnitude decreases. At 900 K, the maximum Seebeck coefficient reaches 372 μV/K for n-type carriers and 413 μV/K for p-type carriers, occurring at carrier concentrations of 3.19×10^{19} cm^{-3} and 5.29×10^{19} cm^{-3}, respectively. These

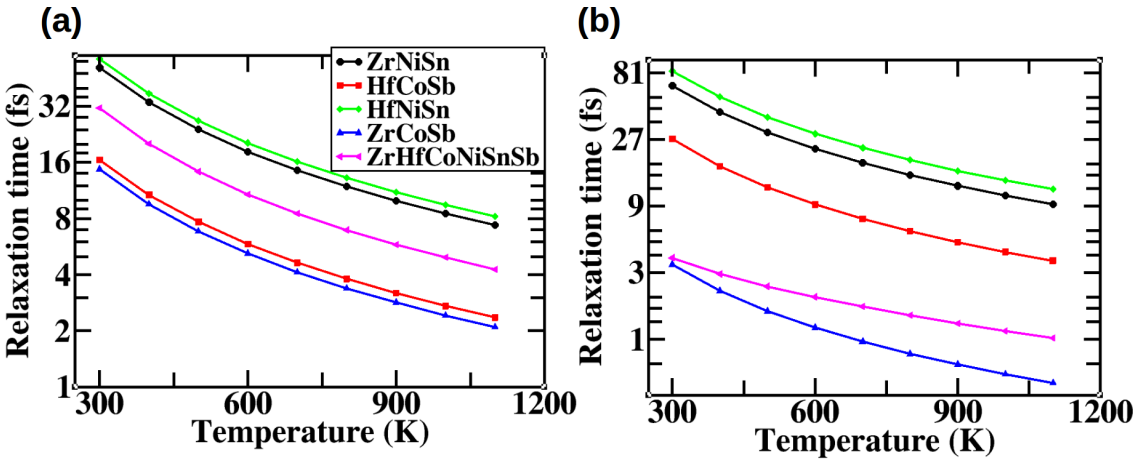

Figure 3.9: Average relaxation time (τ_{av}) of (a) electrons and (b) holes in the parent HHs and the HEA.

concentrations correspond to chemical potentials of 0.16 eV below the conduction band minimum (CBM) for n-type carriers and 0.22 eV above the valence band maximum (VBM) for p-type carriers.

Fig. 3.10(b) presents the electrical conductivity (σ) as a function of carrier concentration at different temperatures for both n-type and p-type carriers. The plot reveals that σ for n-type carriers is higher than that for p-type carriers. This is evident from the fact that the average effective conductive mass of electrons is smaller than that of holes, as indicated in Tables 3.3 and 3.4. The electrical conductivity for both types of carriers remains low up to a carrier concentration of approximately 10^{20} cm^{-3}. This behavior arises because the chemical potential remains within the bandgap in this carrier concentration range, leading to a negligible value of the projected conductivity tensor $\sigma_{ij}(\epsilon)$, as defined by Equation 2.55, at the peak of the selection function $\phi = -\partial f_0(T;\mu)/\partial\epsilon$. Consequently, only the tail of the selection function contributes to the electrical conductivity, resulting in extremely low values of σ. Beyond a carrier concentration of approximately 10^{20} cm^{-3}, the electrical conductivity increases with increasing carrier concentration. This suggests that the chemical potential has shifted into the conduction or valence bands, where $\sigma_{ij}(\epsilon)$ makes a significant contribution to the overall electrical conductivity $\sigma_{ij}(T;\mu)$ at the peak of the selection function. According to the Wiedemann-Franz law, the electronic contribution to the thermal conductivity (k_e) follows a similar trend as σ, as depicted in Fig. 3.10 (c).

The performance of a thermoelectric device is characterized by the power factor ($S^2\sigma$), which directly influences its efficiency. As shown in Fig. 3.10 (a), the Seebeck coefficient

generally decreases with increasing carrier concentration across most of the concentration range. Meanwhile, Fig. 3.10(b) indicates that electrical conductivity increases consistently throughout the entire carrier concentration range. Consequently, the power factor exhibits an optimal value, as observed in Fig. 3.10(d). With increasing temperature, the peak position of the power factor shifts toward higher carrier concentrations. From Fig. 3.10(d), it is evident that for both n-type and p-type carriers, the peak power factor initially increases and then decreases with rising temperature. For the n-type case, ZrHfCoNiSnSb achieves a maximum power factor of 3.32 (3.88) mW K^{-2} m^{-1} at a carrier concentration of 1.26×10^{21} (1.54×10^{21}) cm^{-3} at 300 (900) K, for the chemical potential is located 0.24 (0.23) eV above the conduction band minimum (CBM). In contrast, for the p-type case, the maximum power factor reaches 1.16 (1.06) mW K^{-2} m^{-1} at a carrier concentration of 1.37×10^{21} (2.08×10^{21}) cm^{-3} at 300 (900) K, corresponding to a chemical potential of 0.13 (0.09) eV below the valence band maximum (VBM). For comparison, the transport properties of different systems were plotted against the carrier concentration at 900 K in Appendix A. As shown in Figure A.7(a), which depicts electrical conductivity, HfNiSn exhibits the highest electrical conductivity across all carrier concentrations for the n-type case, followed by ZrNiSn, ZrHfCoNiSnSb, HfCoSb, and ZrCoSb. Similarly, for the p-type case, HfNiSn again shows the highest electrical conductivity, followed by ZrNiSn, HfCoSb, ZrHfCoNiSnSb, and ZrCoSb. Figure A.8(a) illustrates the variation of the Seebeck coefficient as a function of carrier concentration at 900 K for different structures. For the n-type case, ZrCoSb exhibits the highest Seebeck coefficient, followed by HfCoSb, ZrHfCoNiSnSb, ZrNiSn, and HfNiSn. In the p-type case, HfCoSb has the highest Seebeck coefficient, followed by ZrCoSb, ZrHfCoNiSnSb, ZrNiSn, and HfNiSn. These trends in electrical conductivity and the Seebeck coefficient are explained using the projected conductivity tensor $\sigma_{ii}(\epsilon)$, the selection function $\phi = -\partial f_0(T;\mu)/\partial\epsilon$, and the projected Seebeck tensor $\alpha_{ii}(\epsilon)$ (as defined in Equation A.1 of appendix A). Figure A.9(a) in Appendix A presents the variation of the electronic component of thermal conductivity as a function of carrier concentration for different structures at 900 K. In accordance with the Wiedemann-Franz law, this electronic contribution to thermal conductivity follows a similar trend to that of σ, with the structural hierarchy remaining consistent. Figure A.9(b) illustrates the variation of the power factor as a function of carrier concentration for different structures. As observed in the plot, HfNiSn and ZrNiSn exhibit the highest power factor for the n-type case, primarily due to their high electrical conductivity, followed by ZrHfCoNiSnSb, HfCoSb, and ZrCoSb. Similarly, for the p-type case, HfNiSn and ZrNiSn again demonstrate the highest power

factor, followed by HfCoSb. However, for the p-type case, ZrHfCoNiSnSb and ZrCoSb show a power factor approximately an order of magnitude lower than the other systems, predominantly due to their lower electrical conductivity.

3.3.6 Figure of merit

The electronic transport properties, in combination with the lattice thermal conductivity, were used to compute the figure of merit (zT) as a function of carrier concentration for different temperatures, as shown in Fig. 3.10(e). With increasing temperature, the zT peak shifts toward higher carrier concentrations for both n-type and p-type carriers. At all temperatures, the zT value for n-type carriers remains higher than that for p-type carriers. A comparison of zT as a function of carrier concentration at 900 K among different structures is provided in Appendix A. As depicted in Figure A.9(c), for n-type carriers, ZrHfCoNiSnSb exhibits the highest zT value up to a carrier concentration of 4×10^{21} cm^{-3}, followed by ZrNiSn and HfNiSn, which display nearly identical zT values across all carrier concentrations. Despite their high Seebeck coefficients, HfCoSb and ZrCoSb exhibit relatively low zT values for n-type carriers due to their lower electrical conductivity and higher lattice thermal conductivity, as seen in Figure A.9(c) of Appendix A. For p-type carriers, up to a concentration of 1×10^{21} cm^{-3}, ZrNiSn and HfNiSn attain the highest and nearly identical zT values, followed by HfCoSb. However, ZrHfCoNiSnSb and ZrCoSb display comparatively lower zT values across all carrier concentrations, primarily due to their lower electrical conductivity. Fig. 3.11 presents a comparison of the peak zT values for all structures at different temperatures. As observed, for n-type carriers, ZrHfCoNiSnSb consistently exhibits the highest peak zT value across all temperatures, followed by HfNiSn and ZrNiSn. In contrast, HfCoSb and ZrCoSb show comparatively lower peak zT values due to their lower electrical conductivity and higher lattice thermal conductivity. For p-type carriers, HfNiSn attains the highest peak zT value, followed by HfCoSb and ZrNiSn, whereas ZrHfCoNiSnSb and ZrCoSb maintain lower peak zT values across all temperatures due to their lower electrical conductivity. The peak zT value of ZrHfCoNiSnSb for n-type carriers reaches 1.00 at 1100 K, which is 27, 104, 32, and 170 % higher than that of ZrNiSn, HfCoSb, HfNiSn, and ZrCoSb, respectively. The optimized carrier concentration corresponding to this maximum zT value at 300 K and 900 K is provided in Tables A.8 and A.9 in Appendix A.

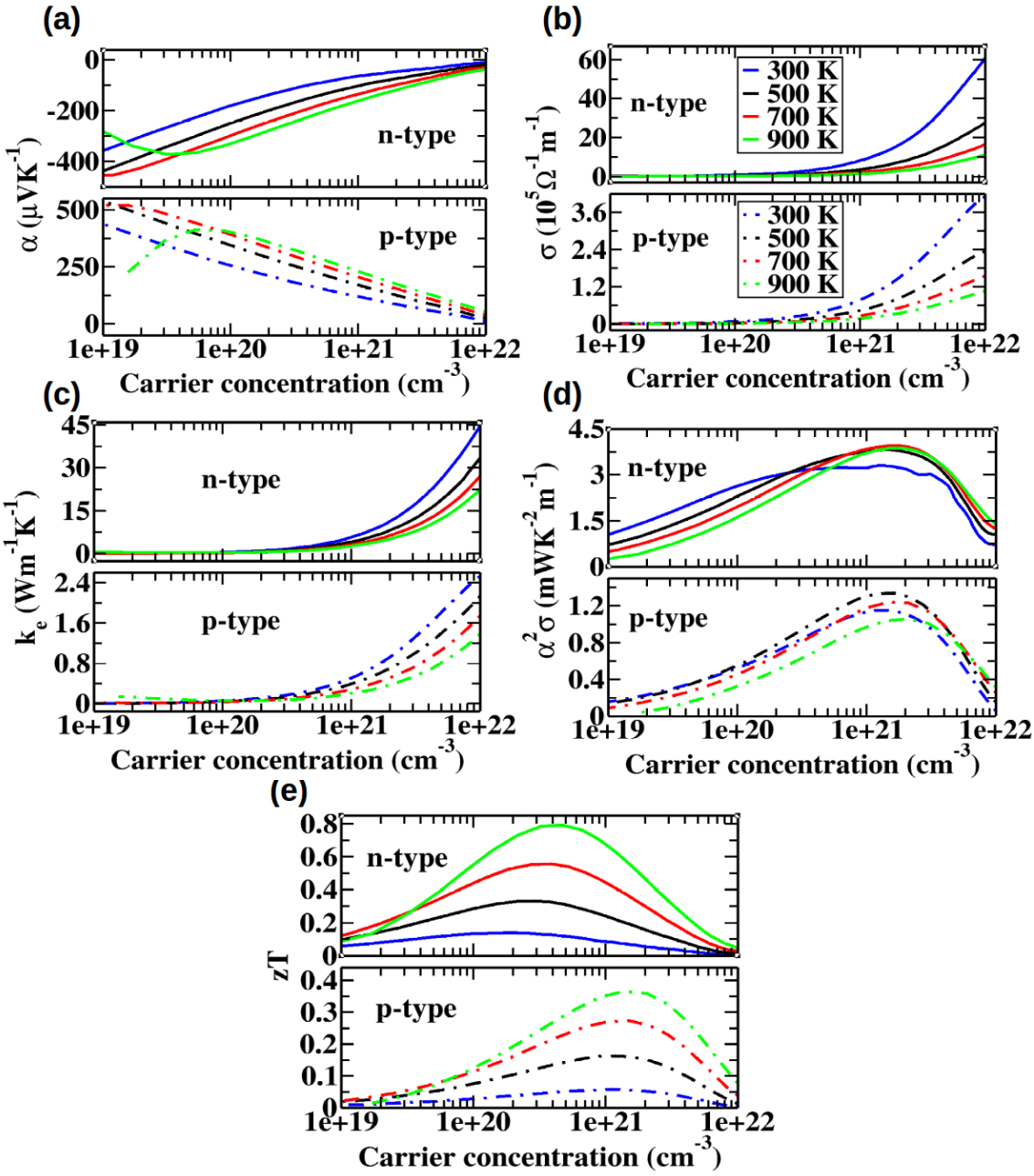

Figure 3.10: (a) Seebeck coefficient, (b) Electrical conductivity, (c) Electronic thermal conductivity, (d) Power factor and (e) Figure of merit as a function of carrier concentration at different temperatures for ZrHfCoNiSnSb.

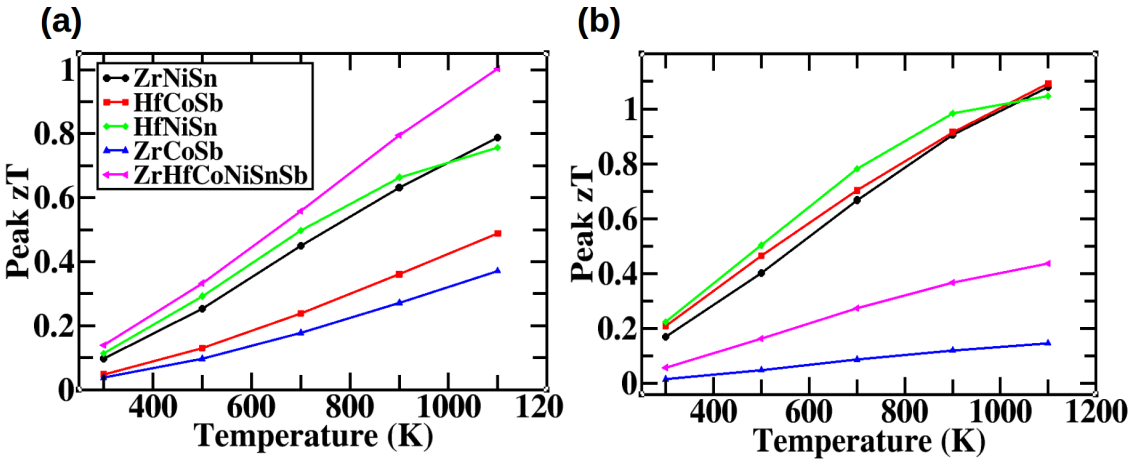

Figure 3.11: (a) Peak value of figure of merit for electrons, (b) Peak value of figure of merit for holes.

3.4 Conclusions

ZrHfCoNiSnSb exhibits greater stability at high temperatures compared to its parent compounds, largely due to the entropic contribution to the Gibbs free energy at elevated temperatures. The absence of imaginary modes in the phonon dispersion curve also confirms its dynamical stability. Additionally, based on both mode-resolved and average Gruneisen parameters, it is suggested that ZrHfCoNiSnSb possesses stronger anharmonicity and higher lattice thermal resistance than its parent compounds. The Seebeck coefficient and the other electronic transport properties of ZrHfCoNiSnSb exhibit comparability to the half-Heusler compounds from which it is composed(i.e., ZrNiSn/HfNiSn and HfCoSb/ZrCoSb). Notably, the lattice thermal conductivity of ZrHfCoNiSnSb is approximately one-third of ZrNiSn/HfNiSn and one-fifth of HfCoSb/ZrCoSb at room temperature, and it has significantly reduced lattice thermal conductivity compared to the parent half-Heusler compounds across all temperatures. For the case when the charge carriers are electrons, at 1100 K, the zT value of ZrHfCoNiSnSb is 1.00, surpassing the values of all of the parent compounds.

Chapter 4

Thermoelectric properties of Nb_2Co_2InSb and Nb_2Co_2GaSb double half-Heuslers

4.1 Introduction

Half-Heusler (hH) alloys represent a versatile class of intermetallic compounds with the general formula XYZ , where X and Y are transition metals, and Z is a p-block element. These materials crystallize in a non-centrosymmetric cubic structure (space group $F\bar{4}3m$) and have attracted significant attention due to their tunable electronic structures, mechanical robustness, and thermal stability. Their application in thermoelectric energy conversion stems from their semiconducting nature, high carrier mobility, and the possibility of band engineering through elemental substitution or disorder. This flexibility has led to the discovery of numerous high-performing thermoelectric compounds, such as ZrNiSn, HfNiSn, and TiNiSn [6, 92, 110] for n-type transport as well as NbFeSb, TaFeSb, and ZrCoBi [32, 111, 112] for p-type transport. A key factor behind their efficiency lies in their outstanding electrical transport capabilities. However, despite their promise, half-Heusler compounds face challenges when compared to leading thermoelectric materials like IV-VI group semiconductors. A major limitation is their inherently high lattice thermal conductivity (k_L), which hinders their performance. For instance, while ZrNiSn exhibits a relatively low k_L of 10 $Wm^{-1}K^{-1}$ [92] at room temperature—one of the best among half-Heusler materials—it remains significantly higher than the k_L of state-of-the-art thermoelectrics like SnTe, and PbTe which has an intrinsic k_L of just 2.5 $Wm^{-1}K^{-1}$ at 300 K [113, 114]. This discrepancy highlights the need for innovative approaches to design new materials that retain the desirable electronic properties of half-Heusler compounds while achieving much lower lattice thermal conductivity.

According to Zintl chemistry [90], half-Heuslers (XYZ) are stable when the valence electron count (VEC) is 18, as this corresponds to fully filled bonding orbitals and empty anti-bonding orbitals. One effective approach to reducing the lattice thermal conductivity (k_L) is introducing mass disorder at lattice sites via aliovalent substitution, while maintaining a VEC of 18. This can be achieved by mixing VEC 17 and VEC 19 ternary half-Heusler compounds in equal proportions to form a quaternary double half-Heusler with VEC 18.

Shashwat Anand *et al.*, [108] predicted 131 quaternary double half-Heuslers derived from ternary half-Heuslers using the `enumlib` code [115], a significant increase compared to the previously identified 84 ternary half-Heusler systems. Among these, $Ti_2FeNiSb_2$, derived from TiCoSb (VEC 18) by combining TiFeSb (VEC 17) and TiNiSb (VEC 19) in equal amounts, was predicted to have a lattice thermal conductivity three times lower than the parent compound TiCoSb.

Similarly, Bhawna Sahini *et al.*, [116] studied the thermoelectric performance of various structural phases of Zr_2Ni_2InSb and Hf_2Ni_2InSb, which are derived from the ternary half-Heuslers ZrNiSn and HfNiSn, respectively. Their findings indicate that these quaternary systems, particularly the ordered structures, exhibit better thermoelectric properties than their ternary counterparts.

Like ZrNiSn and HfNiSn, NbCoSn is a half-Heusler semiconducting system with a band gap of 0.96 eV and a remarkably high melting temperature of approximately 2300 K [117]. Due to its thermal stability at high temperature, NbCoSn has been experimentally synthesized for thermoelectric applications [118]. Additionally, theoretical investigations into its thermoelectric properties have been reported [119]. The lattice thermal conductivity of NbCoSn has been estimated to be 18 $Wm^{-1}K^{-1}$ theoretically and 13.25 $Wm^{-1}K^{-1}$ experimentally. Despite possessing a power factor of 2.1 $mWm^{-1}K^{-2}$ at room temperature, its high lattice thermal conductivity limits its thermoelectric figure of merit (zT) to just 0.05 at room temperature.

This raises the question of whether derivative double half-Heusler structures can be developed from this parent compound, maintaining similar or better electronic properties while achieving significantly lower lattice thermal conductivity. In this project, we theoretically investigate the thermoelectric performance of Nb_2Co_2InSb and Nb_2Co_2GaSb. These compounds can be viewed as derivative double half-Heusler structures derived from the parent half-Heusler compound NbCoSn, where the Sn atom is replaced by In/Ga and Sb atoms.

As shown in Figure 4.1, these double half-Heusler alloys can be conceptualized as a combination of NbCoIn/NbCoGa (VEC 17) and NbCoSb (VEC 19) structures in equal proportions. In this project, a comparative study of the thermoelectric properties of two ordered structures and two (one) disordered structures of Nb_2Co_2InSb (Nb_2Co_2GaSb) was conducted. The results indicate that the ordered phases exhibit significantly superior electronic transport properties (power factor) compared to their disordered counterparts in both compounds. Furthermore, the lattice thermal conductivity of these double half-Heusler alloys is approximately five times lower than that of the ternary NbCoSn, making them highly promising candidates for thermoelectric applications.

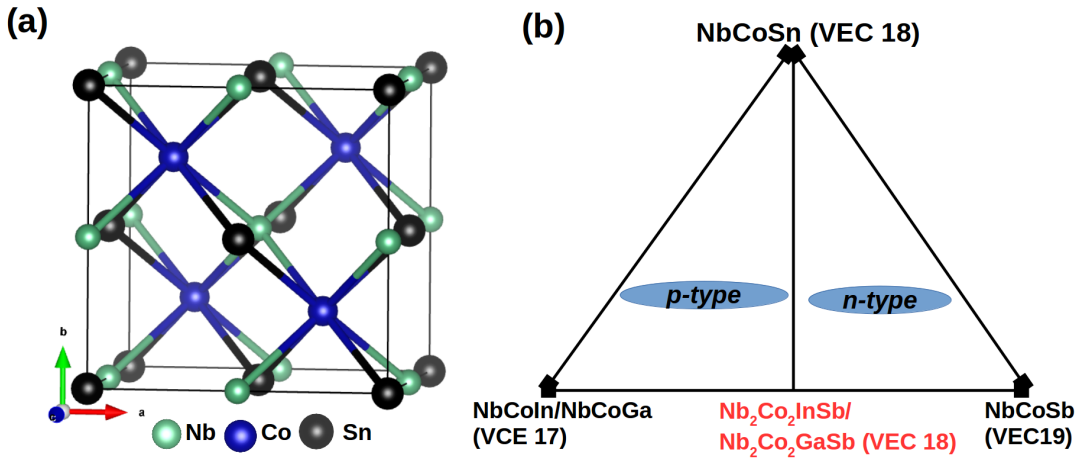

Figure 4.1: (a) Crystal structure of NbCoSn (b) VEC 18 structural derivatives of NbCoSn

Unlike earlier studies, we have explored the properties of these compounds across three relevant structural phases: cubic, tetragonal, and solid solution. For solid solution we generated two different Special Quasi-random structures SQSs (explained in section 3). These phases can be realized depending on the synthesis conditions and temperature, with ordered phases forming at lower temperatures and disordered phases at higher temperatures. For our systems, the ordered structures are exhibiting higher carrier mobility compared to the solid solution phase. Combining electronic transport calculations with the thermal conductivity give better thermoelectric performance for the ordered structures for Nb_2Co_2GaSb but for Nb_2Co_2InSb, the disorder structure has better thermoelectric performance.

4.2 Computational details

Four different structural phases of both the systems were studied. Two of these are ordered structures and another two are Special Quasi-random structures(SQSs). The first ordered structure (OS1) was generated by replacing Sn atoms with In/Ga and Sb atoms in conventional unit cell. This generates Six different structures which was found to be energetically same after optimization. The second ordered structure (OS2) has been taken from Open Quantum Material Database (OQMD). OQMD predicts OS2 as the most stable structure. The SQSs were generated with a constraint that the In/Ga and Sb atoms occupy the 4a(0, 0, 0) site. One of the SQSs is 12 atom SQSs without any constraint on the lattice structure (SQS1) while the second one is 24 atoms SQS with a contraint on the structure to be $2 \times 2 \times 2$ supercell of the primitive unit cell of half-Heusler structure (SQS2). In the construction of the SQS structures, pair correlation functions were included up to the fourth nearest-neighbor distance, while triplet correlations were considered up to the third nearest-neighbor distance. The SQS2 configuration of Nb_2Co_2GaSb was found to be dynamically unstable, and as a result, it was not considered for further analysis.

The calculations were carried out using plane-wave density functional theory (DFT) based calculations as implemented in the Quantum ESPRESSO [101, 120] software. The electron-ion interactions were described using ultrasoft pseudopotentials. For the wave-function (charge density) we have used a basis set whose size corresponds to kinetic energy cutoff of 110 Ry (880 Ry). The electron-electron exchange and correlation effects were treated using the Perdew-Burke-Ernzerhof (PBE) [50] parametrization of the generalized gradient approximation (GGA). For electronic calculations, the Brillouin zone was sampled with a shifted $8 \times 8 \times 8$ for OS1, and OS2, $12 \times 8 \times 6$ for SQS1 and $4 \times 4 \times 4$ for SQS2 Monkhorst-pack k-mesh. To compute the density of states (DOS) and the electronic transport properties, we used $24 \times 24 \times 24$ k-mesh grid for OS1 and OS2, $36 \times 24 \times 18$ for SQS1 and $12 \times 12 \times 12$ for SQS2. To study the dynamical stability, vibrational properties and lattice thermal conductivity, the phonons were computed using density functional perturbation theory [64]. The calculations were performed on a q-mesh of $2 \times 2 \times 2$ for OS1, and OS2, $3 \times 2 \times 2$ for SQS1 and $2 \times 2 \times 2$ for SQS2.

Electronic transport properties were calculated by using the semi-classical Boltzmann transport theory within the constant relaxation time and rigid band approximations as implemented in the BoltzTrap2 code [68]. Using BoltzTrap2 code Seebeck coefficient, electrical conductivity per unit relaxation time, thermal conductivity per unit relaxation

time and power factor per unit relaxation time were calculated. The constant relaxation time was then calculated using deformation potential theory (as explained in section 2.7 of chapter 2) [103] and multiplied with the above transport coefficients per unit relaxation time to get the electronic transport coefficients.

4.3 Results and Discussions

The crystal structures of all the structures are shown in the Figures 4.2 and 4.3 and their lattice parameters and relative energy is given in Tables 4.1 and 4.2.

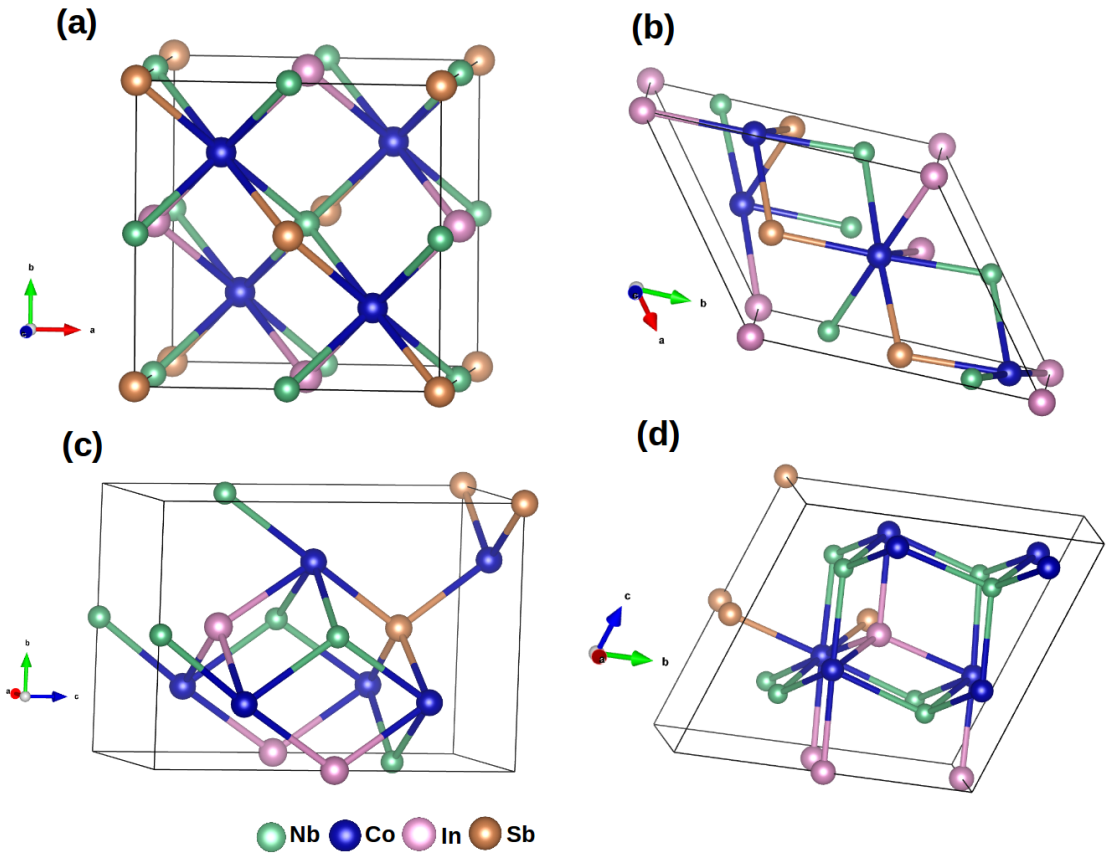

Figure 4.2: Optimized crystal structure of Nb_2Co_2InSb of (a) OS1 (b) OS2 (c) SQS1 (d) SQS2

In Tables 4.1 and 4.2, ΔE is the change in energy per formula unit of a particular structure from the most stable structure. As can be seen from the Tables 4.1 that for Nb_2Co_2InSb,

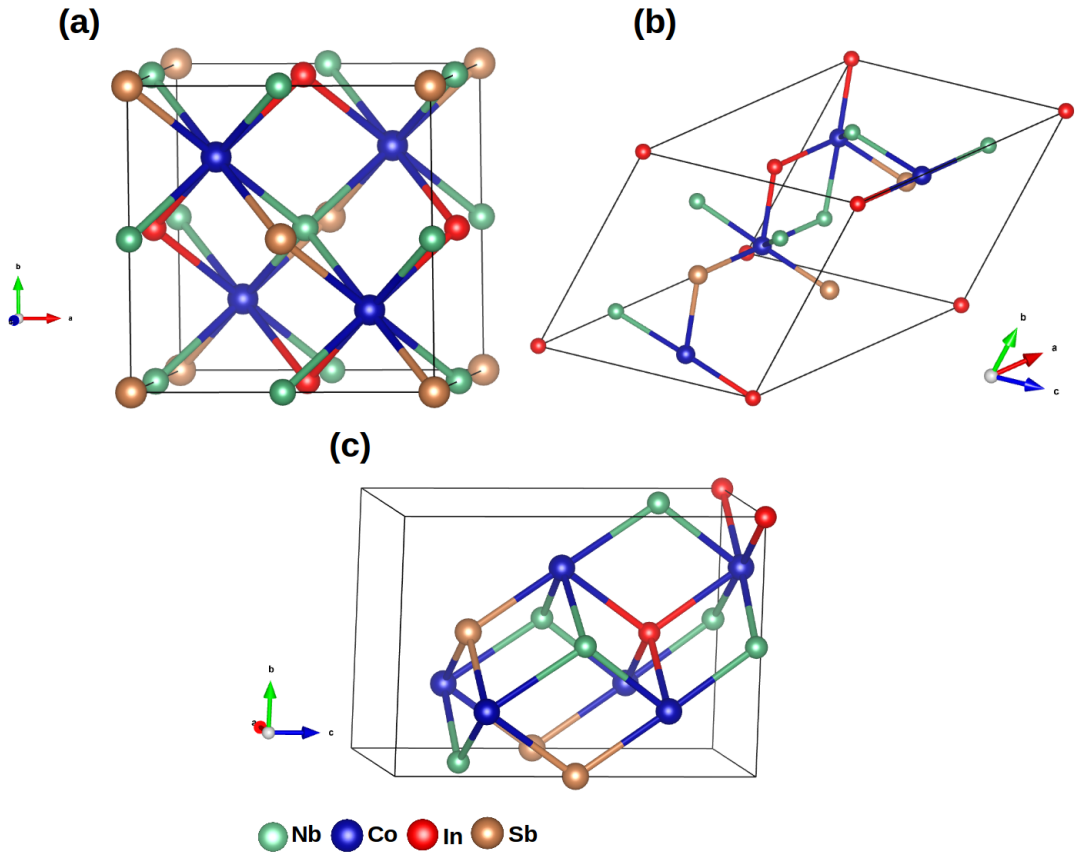

Figure 4.3: Optimized crystal structure of Nb_2Co_2GaSb of (a)OS1 (b) OS2 (c) SQS1

Table 4.1: Computed lattice parameters and the relative energies of all the structures of Nb_2Co_2InSb .

Structure	Lattice parameters (Å)	Angles (°)	ΔE per formula unit (meV)
OS1	a = b = 5.969, c = 5.962	$\alpha = \beta = \gamma = 90$	13.58
OS2	a = b = 5.964, c = 11.935	$\alpha = \beta = \gamma = 90$	0
SQS1	a = 4.216, b = 4.968, c = 8.439	$\alpha = \beta = \gamma = 90$	62.18
SQS2	a = b = c = 8.438	$\alpha = \beta = \gamma = 60$	66.97

OS2 is the most stable structure (as predicted by OQMD) but for Nb_2Co_2GaSb, SQS1 is the most stable configuration. Also for OS1, there is minor contraction of lattice parameter along the c axis changing it from cubic symmetry to tetragonal symmetry.

Table 4.2: Computed lattice parameters and the relative energies of all the structures of Nb_2Co_2GaSb .

Structure	Lattice parameters (Å)	Angles (°)	ΔE per formula unit (meV)
OS1	a = b = 5.859, c = 5.843	$\alpha = \beta = \gamma = 90$	115.51
OS2	a = b = 5.857, c = 11.684	$\alpha = \beta = \gamma = 90$	12.06
SQS1	a = 4.121, b = 5.867, c = 8.276	$\alpha = \beta = \gamma = 90$	0

4.3.1 Electronic properties

Figures 4.4 and 4.5 shows the band structure and density of states (DOS) of all the structures of Nb_2Co_2InSb and Nb_2Co_2GaSb. As observed from the DOS plots, the valence and conduction band edges are primarily composed of Nb and Co d orbitals, with a minor contribution from In/Ga p orbitals. For both the systems, increasing disorderness has lead to increment in the band gap OS1 being the lowest for both the systems and SQS2 being the highest for Nb_2Co_2InSb and SQS1 for Nb_2Co_2GaSb. The band gap of the different structures are 0.21(0.23), 0.61(0.70), 0.69(0.74) and 0.74 eV for OS1, OS2, SQS1 and SQS2 respectively for Nb_2Co_2InSb (Nb_2Co_2GaSb).

In the OS1 structure for both systems, the valence band maximum (VBM) is located at the Γ point. The conduction band minimum (CBM) also occurs at the Γ point; however, an additional conduction band extremum (CBE) is present at the same point, lying 63meV (130meV) above the CBM for Nb_2Co_2InSb (Nb_2Co_2GaSb). For the OS2 structure, the VBM again lies at the Γ point for both systems. The CBM is also at Γ, while a CBE appears at the Z point, positioned 27meV (28meV) above the CBM for Nb_2Co_2InSb (Nb_2Co_2GaSb). In the case of the SQS1 structure, the VBM is located at the S point, with another valence band extremum (VBE) situated between the Z and U points, which lies 18meV (60meV) below the VBM for Nb_2Co_2InSb (Nb_2Co_2GaSb). The CBM for SQS1 is located at the X point in both systems. For Nb_2Co_2InSb, there is an additional CBM at the Γ point, whereas in Nb_2Co_2GaSb, a CBE occurs at Γ, which is 53 meV above the CBM. In the SQS2 structure of Nb_2Co_2InSb, both the VBM and CBM are at the Γ point. There is also a VBE at the same point lying 5meV below the VBM and a CBE 58meV above the CBM.

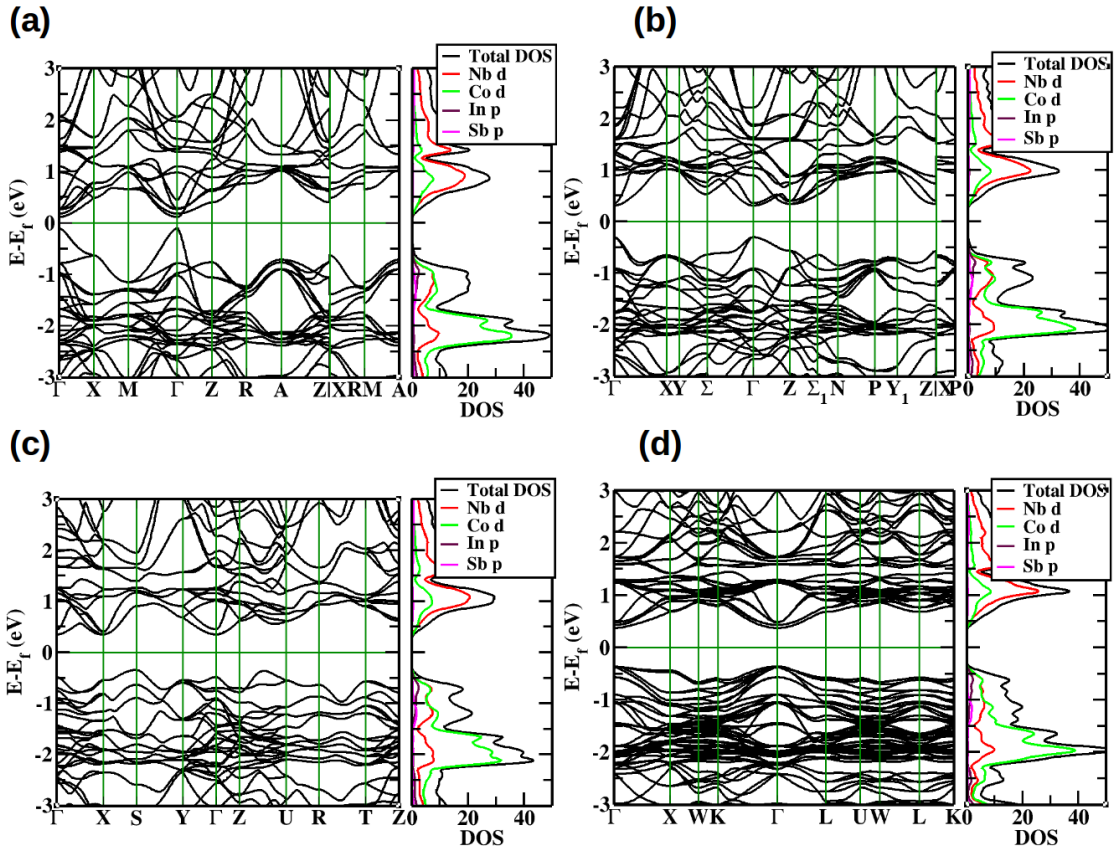

Figure 4.4: Band structures and DOS of Nb_2Co_2InSb (a)OS1 (b) OS2 (c) SQS1 (d) SQS2

4.3.2 Carrier Relaxation Times

The average relaxation time (τ_{av}) of charge carriers in these structures was determined using deformation potential theory [103], as detailed in Section 2.7 of Chapter 2. This method considers only the scattering of charge carriers by acoustic phonons. The conductivity and density of states effective masses at different band extrema in the Brillouin zone, which are required for calculating the relaxation time, are provided in Tables B.1 to B.8 in Appendix B.

The average relaxation time (τ_{av}) was computed by considering all electronic bands situated within approximately 100 meV above the conduction band minimum (for electrons) and 100 meV below the valence band maximum (for holes).The parameters required to calculate τ_{av} along with the values of τ_{av} and μ_{av} for electrons and holes at 300 K for all structures, are presented in Tables 4.3 and 4.4, respectively. From these tables, it is evident that for Nb_2Co_2InSb, the holes have a lower effective mass compared to the electrons. For

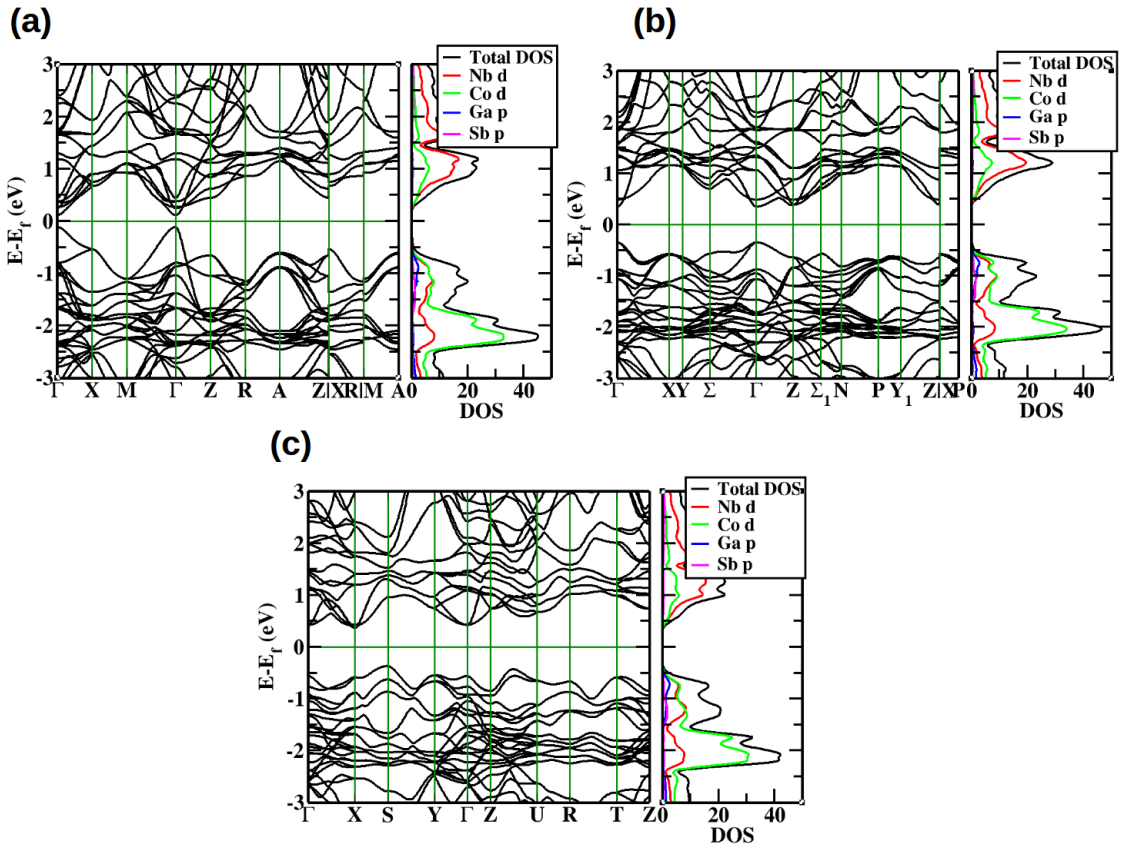

Figure 4.5: Band structures and DOS of Nb_2Co_2GaSb (a)OS1 (b) OS2 (c)SQS1

Nb_2Co_2GaSb, OS1 exhibits a lower effective mass for holes than electrons, while in OS2 and SQS1, the electrons have lighter bands than the holes.

In both systems, holes demonstrate exceptionally high carrier mobility (μ_{av}) in the ordered structures, with the highest value of 1746.7 cm^2/Vs observed in OS1 of Nb_2Co_2GaSb. For electrons, Nb_2Co_2GaSb also shows remarkably high mobility across all structures. This high mobility for holes contributes to significantly greater relaxation times in OS1 and OS2, where the relaxation times are an order of magnitude higher than those of SQS1, as shown in the temperature-dependent relaxation time plots in Figure 4.6 (b) and (d).

Additionally, the deformation potential magnitudes for electrons and holes, which quantify the coupling strength between charge carriers and acoustic phonons, are found to be comparable.

Table 4.3: The average conductivity effective mass ($m^*_{\sigma,av}$), deformation potentials ($|\Xi|$), elastic constants (C), average mobility (μ_{av}), and average relaxation time (τ_{av}) for electrons in the various structural configurations of Nb_2Co_2InSb (Nb_2Co_2GaSb) are presented. The values of μ_{av} and τ_{av} listed in the table were calculated at a temperature of 300 K.

Properties	NbCoSn	OS1	OS2	SQS1	SQS2
$m^*_{\sigma,av}$	1.30	0.68 (0.33)	1.49 (0.38)	1.05 (0.47)	0.76
$\|\Xi\|$ (eV)	18.44	17.54 (17.49)	17.48 (17.48)	17.36 (17.42)	17.41
C (GPa)	283.65	283.14 (292.01)	323.56 (367.06)	253.67 (276.97)	276.67
μ_{av} (cm^2/Vs)	6.03	107.37 (890.3)	26.20 (562.24)	29.74 (278.43)	80.49
τ_{av} (fs)	5.63	41.7 (166)	22.2(121)	17.7 (73.9)	35.5

Table 4.4: The average conductivity effective mass ($m^*_{\sigma,av}$), deformation potentials ($|\Xi|$), elastic constants (C), average mobility (μ_{av}), and average relaxation time (τ_{av}) for holes in the various structural configurations of Nb_2Co_2InSb (Nb_2Co_2GaSb) are presented. The values of μ_{av} and τ_{av} listed in the table were calculated at a temperature of 300 K.

Properties	NbCoSn	OS1	OS2	SQS1	SQS2
$m^*_{\sigma,av}$	0.93	0.17 (0.20)	0.49 (0.61)	0.86 (0.79)	1.93
$\|\Xi\|$ (eV)	17.65	17.29 (16.78)	17.08 (17.03)	16.75 (16.98)	16.99
C (GPa)	283.65	283.14 (292.01)	323.56 (367.06)	253.67 (276.97)	276.67
μ_{av} (cm^2/Vs)	2.91	297.98 (1746.7)	339.69 (236.05)	10.99(21.58)	64.55
τ_{av} (fs)	1.54	294 (202)	95 (82.6)	8.10 (9.73)	70.7

4.3.3 Electronic transport calculations

All electronic transport calculations were performed by combining the Boltzmann transport equation, assuming a constant relaxation time, with relaxation times derived from deformation potential theory. The Seebeck coefficient, electrical conductivity, and power factor as functions of carrier concentration at 1000 K are illustrated in Figures 4.7, 4.8, and 4.9, respectively.

As shown in Figure 4.7, the magnitude of the Seebeck coefficient for all the structures initially increases with carrier concentration, reaching a peak before decreasing. For NbCoSn in the n-type configuration, the maximum Seebeck coefficient is 473 μVK^{-1} at a carrier concentration of 3.68×10^{19} cm^{-3}, whereas in the p-type case, it peaks at 537 μVK^{-1} at 3.19×10^{19} cm^{-3}. For Nb_2Co_2InSb (n-type), the peak Seebeck coefficients for OS1, OS2, SQS1, and SQS2 are 277, 380, 378, and 391 μVK^{-1}, occurring at carrier concentrations of 2.46×10^{20}, 7.55×10^{19}, 7.69×10^{19}, and 6.98×10^{19} cm^{-3}, respectively. For the p-type configuration of the same compound, the respective peak values are 151, 320, 364, and 391 μVK^{-1} at 1.39×10^{20}, 6.34×10^{19}, 8.62×10^{19}, and 9.73×10^{19} cm^{-3}.

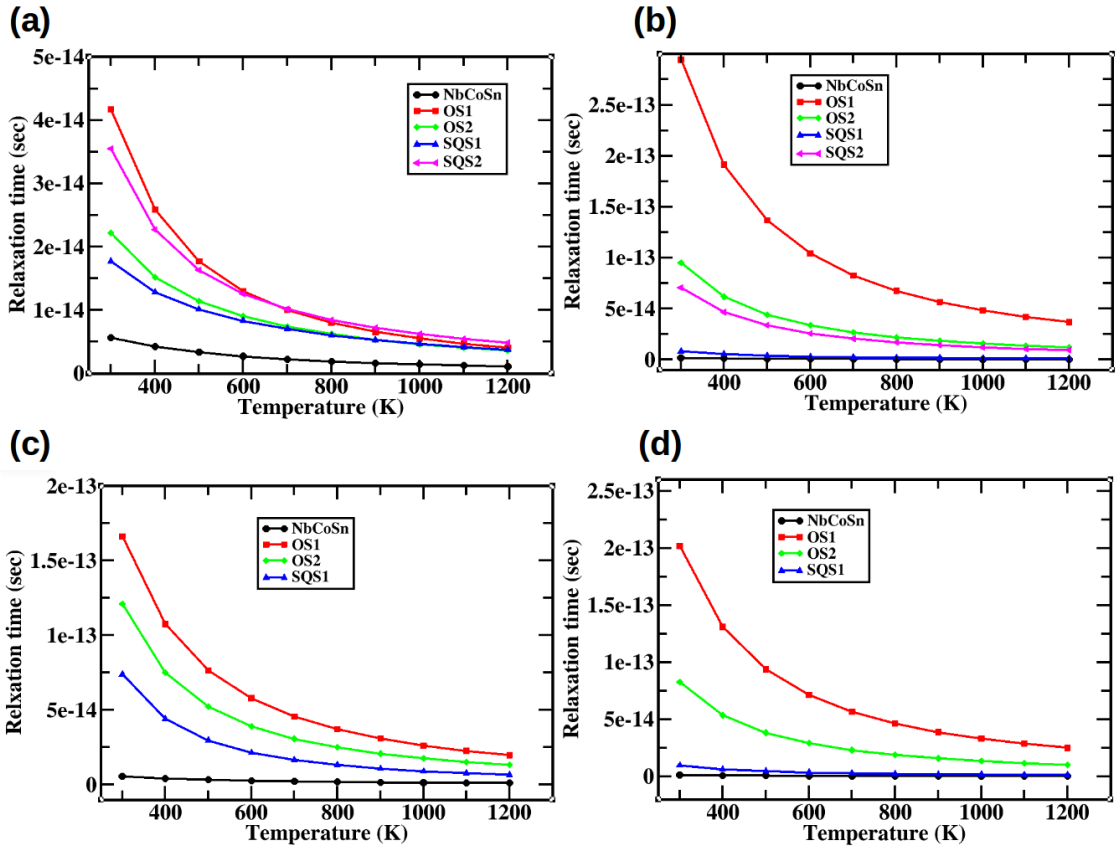

Figure 4.6: Carrier relaxation time for (a) n-type Nb_2Co_2InSb (b) p-type Nb_2Co_2InSb (c) n-type Nb_2Co_2GaSb (d) p-type Nb_2Co_2GaSb

In the case of Nb_2Co_2GaSb (n-type), OS1, OS2, and SQS1 exhibit peak Seebeck coefficients of 283, 417, and 421 μVK^{-1} at carrier concentrations of 1.76×10^{20}, 3.01×10^{19}, and 5.78×10^{19} cm^{-3}, respectively. For the p-type scenario, the peak values are 198, 415, and 403 μVK^{-1} at 1.22×10^{20}, 4.51×10^{19}, and 5.24×10^{19} cm^{-3} for OS1, OS2, and SQS1, respectively.

Figure 4.8 shows that the electrical conductivity of all the structures in both systems remains negligible up to a carrier concentration of approximately 1×10^{20} cm^{-3}. This is because, at such low carrier concentrations, the chemical potential lies within the band gap, resulting in minimal electrical conductivity. As the carrier concentration increases, the conductivity rises accordingly. Furthermore, from Figure 4.8(b) and (d), it is evident that for OS1, the electrical conductivity in the p-type case is about an order of magnitude higher than that of the other structures for both systems. This behavior is consistent with the values presented in Table 4.4, which shows that OS1 has a lower average effective

mass compared to the other configurations. A similar trend is observed for the n-type case, where OS1 also exhibits higher electrical conductivity due to its lower average effective mass, as listed in Table 4.3.

As observed in Figures 4.7 and 4.8, the magnitude of the Seebeck coefficient decreases while the electrical conductivity increases with increasing carrier concentration beyond approximately 1×10^{20} cm^{-3}. This complementary behavior leads to an optimal value of the power factor, $\alpha^2\sigma$, as illustrated in Figure 4.9. Particularly for the p-type configuration, OS1 exhibits a significantly higher peak power factor compared to the other structures. For NbCoSn, the peak power factor in the n-type case is 1.80 mWm^{-1}K^{-2}, occurring at a carrier concentration of 2.76×10^{21} cm^{-3}, while for the p-type case, the maximum value is 0.66 mWm^{-1}K^{-2} at 4.35×10^{21} cm^{-3}. In the case of Nb_2Co_2InSb (n-type), the peak power factors for OS1, OS2, SQS1, and SQS2 are 5.01, 3.87, 3.66, and 4.70 mWm^{-1}K^{-2} at carrier concentrations of 2.28×10^{21}, 1.94×10^{21}, 1.75×10^{21}, and 1.72×10^{21} cm^{-3}, respectively. For the p-type case, the corresponding peak values are 45.40, 9.72, 0.91, and 8.38 mWm^{-1}K^{-2} at carrier concentrations of 3.84×10^{21}, 1.53×10^{21}, 1.59×10^{21}, and 1.86×10^{21} cm^{-3}. For Nb_2Co_2GaSb in the n-type case, the maximum power factors for OS1, OS2, and SQS1 are 27.62, 15.18, and 8.11 mWm^{-1}K^{-2} at carrier concentrations of 2.73×10^{21}, 1.93×10^{21}, and 1.64×10^{21} cm^{-3}, respectively. For the p-type case, OS1, OS2, and SQS1 reach peak power factors of 34.85, 10.91, and 1.30 mWm^{-1}K^{-2} at carrier concentrations of 2.66×10^{21}, 2.46×10^{21}, and 2.20×10^{21} cm^{-3}, respectively.

4.3.4 Phonon dispersion and Lattice thermal conductivity

To assess the dynamical stability of both systems, phonon dispersion curves were calculated for all structures of Nb_2Co_2InSb and Nb_2Co_2GaSb. The phonon dispersion curves are presented in Figure 4.10 for Nb_2Co_2InSb and Figure 4.11 for Nb_2Co_2GaSb. Among all the considered structures, only SQS2 of Nb_2Co_2GaSb exhibited dynamical instability due to the presence of imaginary phonon modes. The phonon dispersion curve of SQS2 of Nb_2Co_2GaSb is shown in Figure B.5 of Appendix B. In contrast, all other configurations for both systems showed no imaginary frequencies, indicating their dynamical stability. From the phonon density of states (PDOS), it is evident that the low-frequency range (0–150 cm^{-1}) is primarily contributed by Sb, In/Ga, and Nb atoms. In the intermediate range (150–230 cm^{-1}), Nb atoms dominate, whereas the higher frequency range (above 230 cm^{-1}) is predominantly influenced by the lighter Co atoms.

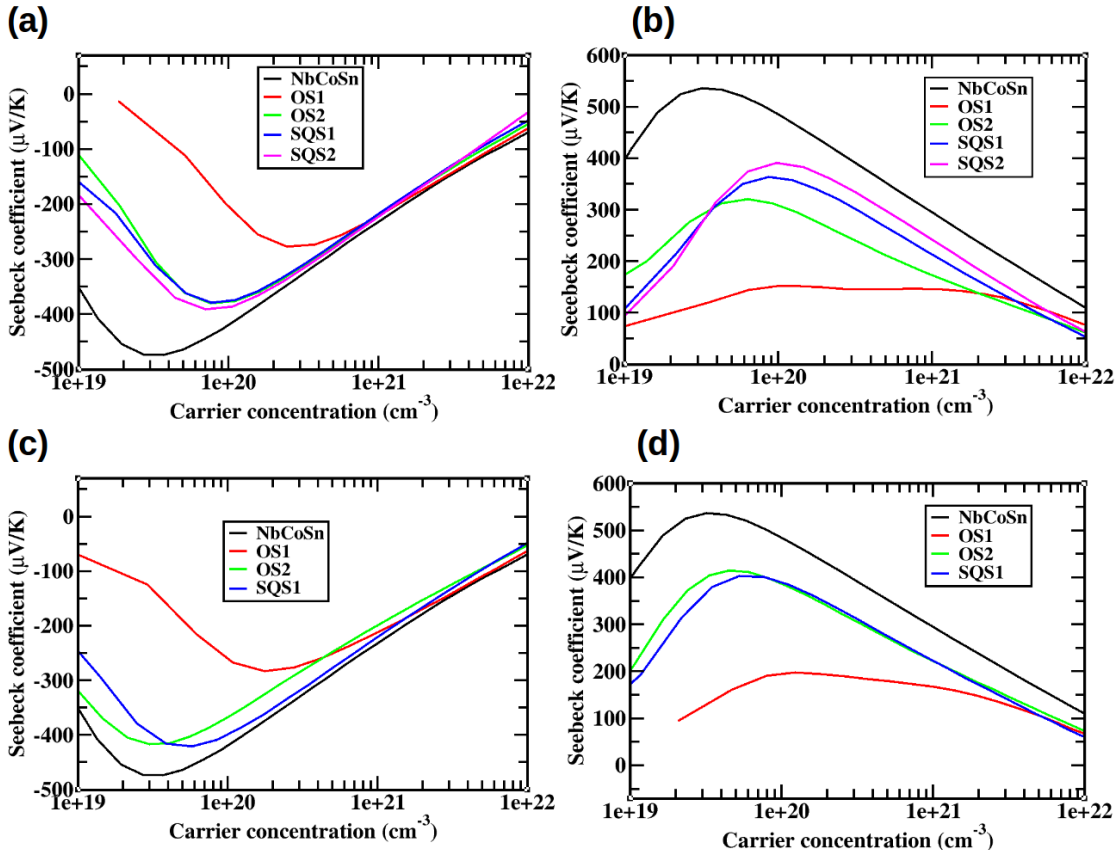

Figure 4.7: Seebeck coefficient at 1000K for (a) n-type Nb_2Co_2InSb (b) p-type Nb_2Co_2InSb (c) n-type Nb_2Co_2GaSb (d) p-type Nb_2Co_2GaSb

To assess anharmonicity in the structures, the mode-resolved Grüneisen parameter (γ_i^k) was calculated. For a phonon in the i^{th} branch with wave vector k, it is defined as:

$$\gamma_i^k = -\frac{V_0}{\omega_i^k}\frac{\partial \omega_i^k}{\partial V} \tag{4.1}$$

where V_0 is the equilibrium volume of the unit cell, and ω_i^k represents the frequency of the corresponding phonon. The derivative in Equation 4.1 was computed numerically using the central difference method. For all the dynamically stable structures except SQS1 of Nb_2Co_2GaSb, the Gruneisen parameters were calculated using the phonon dispersions by increasing and decreasing the lattice parameters by 1%. In the case of SQS1 of Nb_2Co_2GaSb, a smaller change of 0.5% was used instead. This was because a 1% increment led to bending of the transverse acoustic modes near the Γ point, resulting in a non-linear dispersion curve in that region.

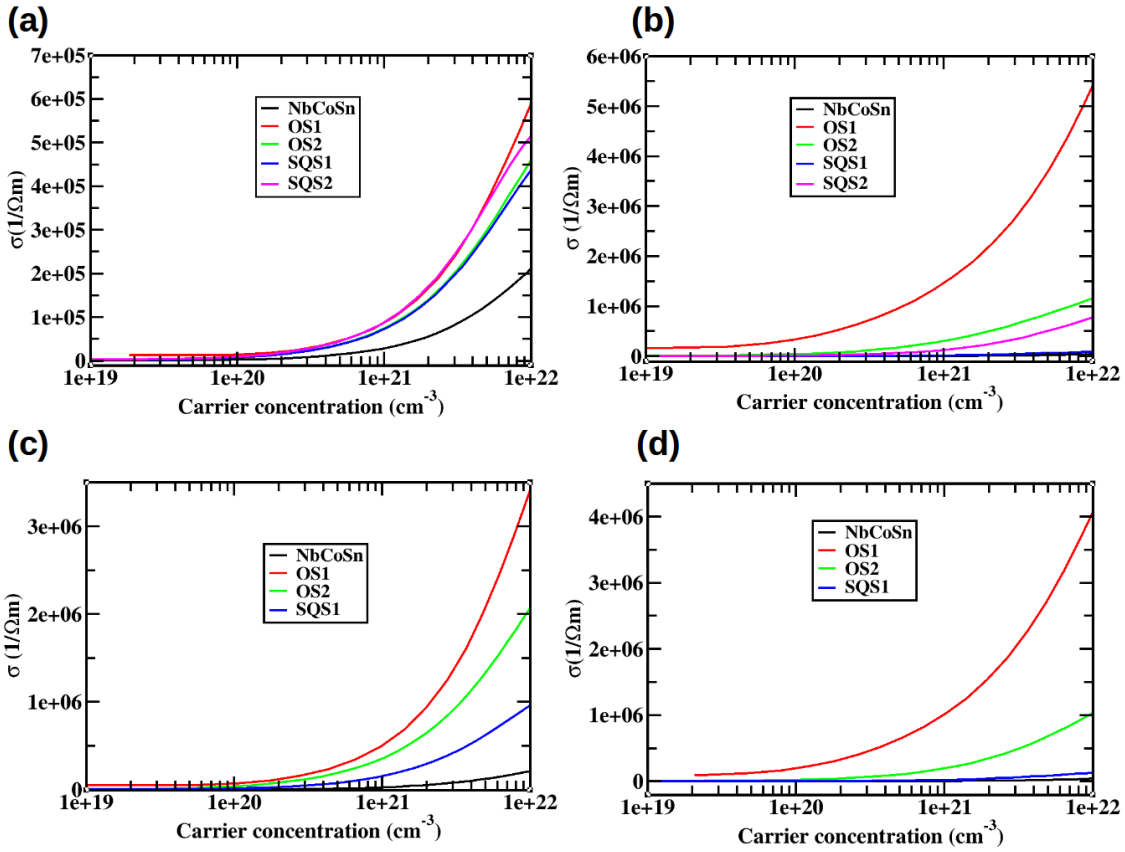

Figure 4.8: Electrical conductivity at 1000K for (a) n-type Nb_2Co_2InSb (b) p-type Nb_2Co_2InSb (c) n-type Nb_2Co_2GaSb (d) p-type Nb_2Co_2GaSb

Figure 4.12 illustrates the Grüneisen parameters for different structures of both Nb_2Co_2InSb and Nb_2Co_2GaSb. The results indicate that SQS1 exhibits greater anharmonicity in both systems. Its Grüneisen parameters span a wider range, varying from 0 to 3 for Nb_2Co_2InSb and 0 to 6 for Nb_2Co_2GaSb, compared to the narrower range of 0.5 to 2.5 observed in other structures.

The lattice thermal conductivity (k_L) for all systems was calculated using the Debye-Callaway model [79, 81, 106] . This model considers k_L as the sum of contributions from the longitudinal acoustic (k_{LA}) and two transverse acoustic branches (k_{TA} and $k_{TA'}$). The methodology for calculating the lattice thermal conductivity is detailed in section 2.8 of chapter 2.

In most crystalline solids, resistive scattering arises primarily due to Umklapp processes. Hence, for half-Heusler NbCoSn, the total phonon scattering rate for i^{th} mode combines

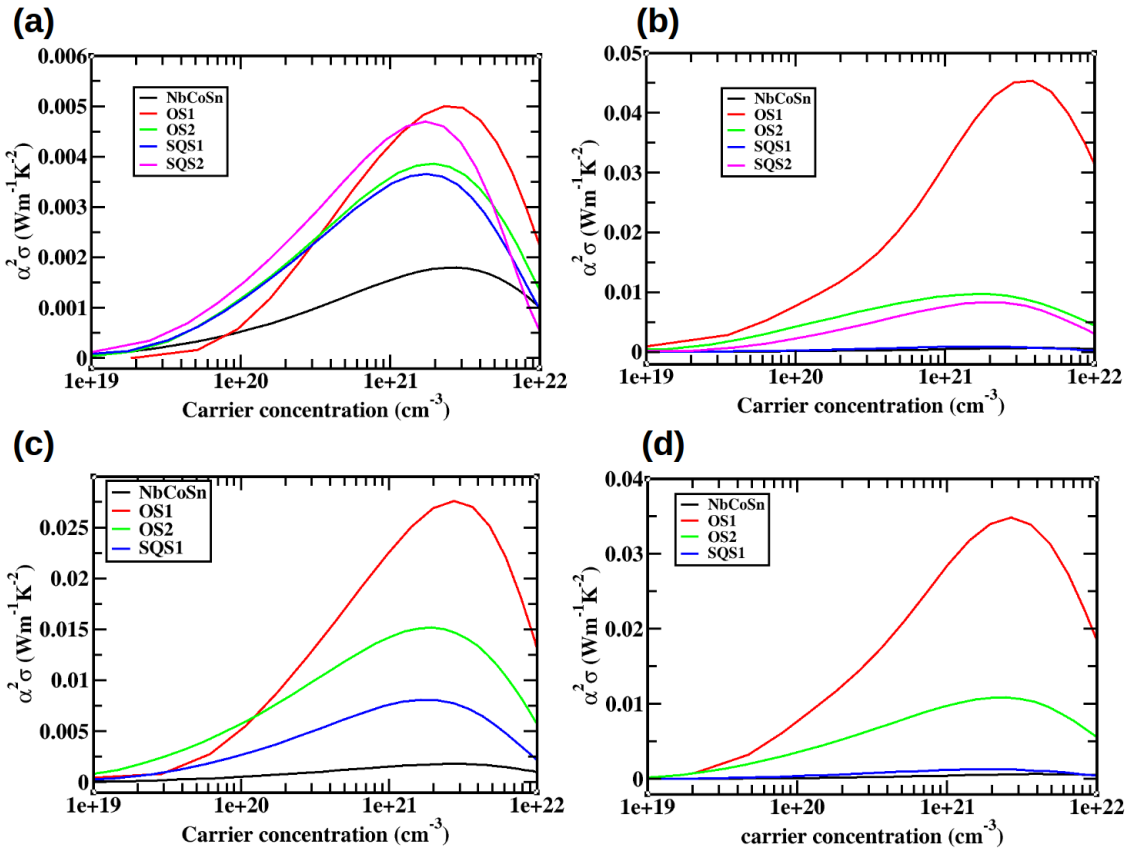

Figure 4.9: Power factor at 1000K for (a) n-type Nb_2Co_2InSb (b) p-type Nb_2Co_2InSb (c) n-type Nb_2Co_2GaSb (d) p-type Nb_2Co_2GaSb.

the contributions from normal and Umklapp processes as:

$$\frac{1}{\tau^C_{HH,i}} = \frac{1}{\tau^N_i} + \frac{1}{\tau^U_i} \tag{4.2}$$

However, in the double Heusler compounds Nb_2Co_2InSb and Nb_2Co_2GaSb, significant mass and strain field fluctuations occur due to the Wyckoff position 4c (0.0, 0.0, 0.0) being occupied by either In/Ga or Sb atoms, which differ in mass and atomic radius. This results in additional phonon scattering from these point defects. Therefore, in the double half-Heuslers (DHH), propagating phonons are also expected to be scattered by mass and strain field defects arising from these fluctuations, which play a significant role in phonon scattering. Hence, to compute the scattering rates for dissipative processes in the double half-Heuslers, we have also incorporated the effect of mass and strain field fluctuation scattering. Consequently, the total relaxation time for the i^{th} mode of DHH is given by :

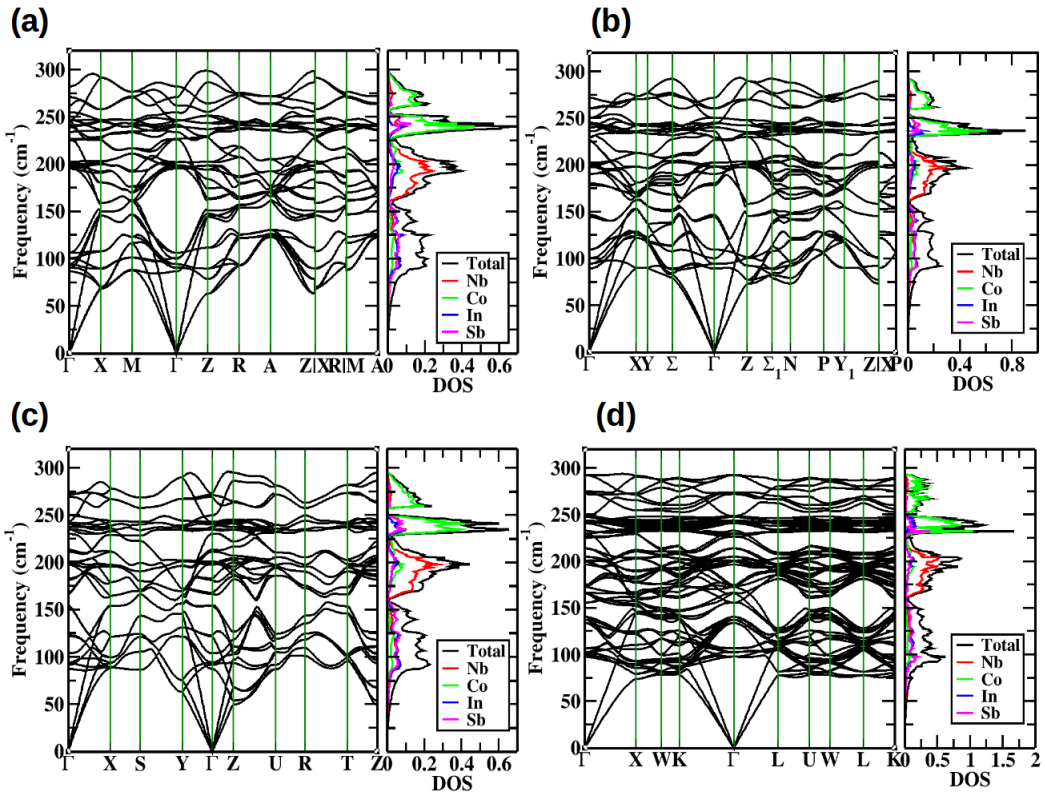

Figure 4.10: Phonon dispersions and phonon DOS of different structures of Nb_2Co_2InSb (a) OS1 (b) OS2 (c) SQS1 (d) SQS2.

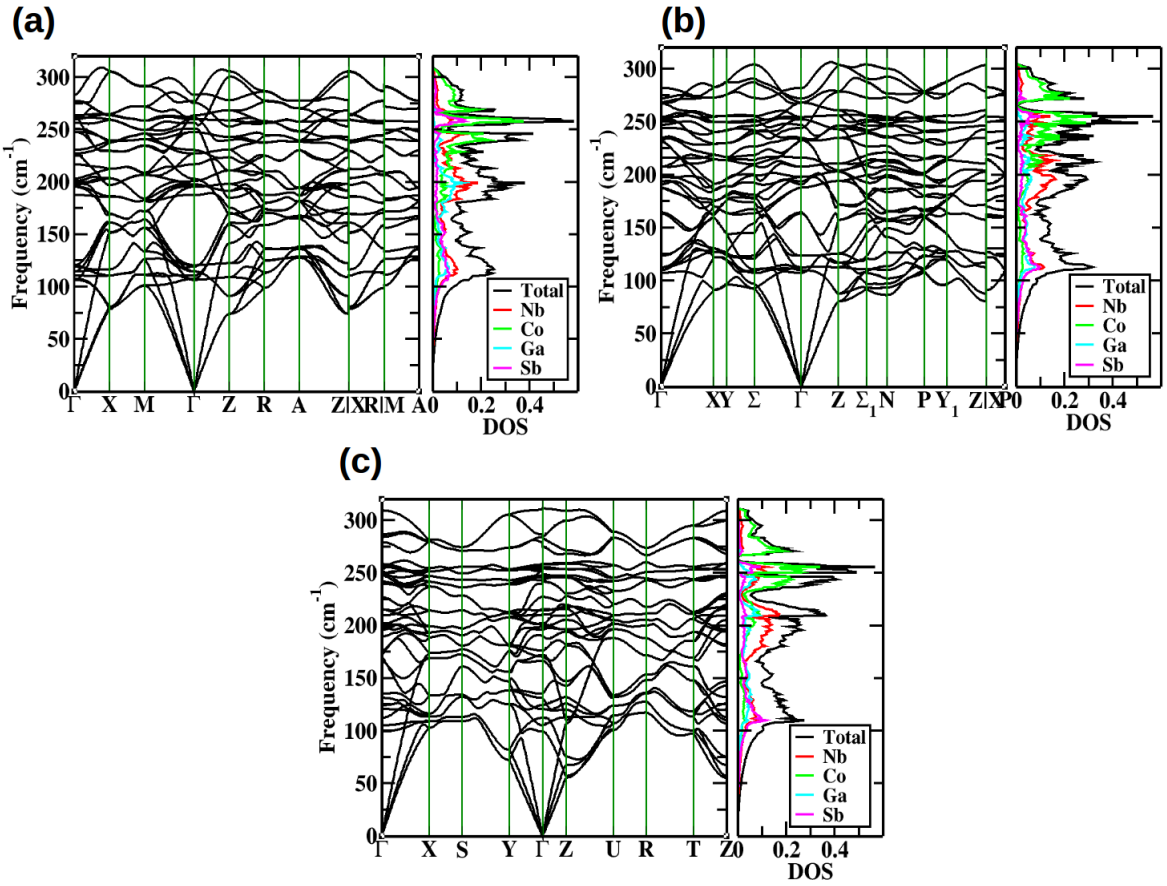

Figure 4.11: Phonon dispersions and phonon DOS of different structures of Nb_2Co_2GaSb (a) OS1 (b) OS2 (c) SQS1.

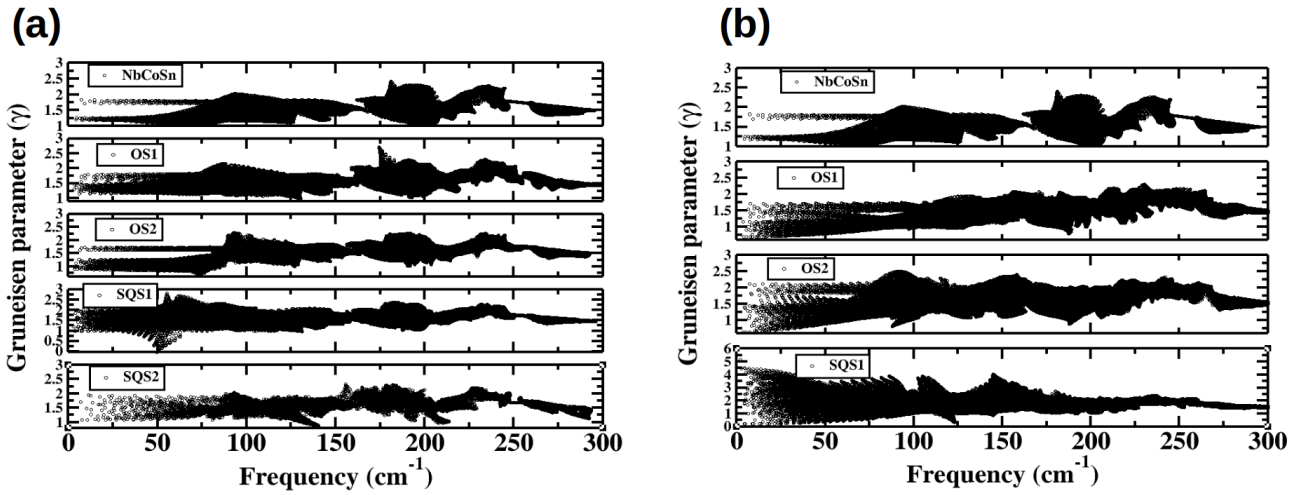

Figure 4.12: Mode resolved Gruneisen parameters for different structures of (a) Nb_2Co_2InSb and (b) Nb_2Co_2GaSb.

$$\frac{1}{\tau^C_{DHH,i}} = \frac{1}{\tau^N_i} + \frac{1}{\tau^U_i} + \frac{1}{\tau^M_i} + \frac{1}{\tau^S_i} \tag{4.3}$$

The parameters used to compute k_L are summarized in Table 4.5.

Table 4.5: The longitudinal velocity, transverse velocities, mode-resolved Debye temperature (θ_i), mode-resolved Gruneisen parameters (γ_i), and the total Gruneisen parameter (γ) for NbCoSn and the different structures of Nb_2Co_2InSb (Nb_2Co_2GaSb) are listed below.

System	Longitudinal velocity (v_{LA}) (m/sec)	Transverse velocity (v_{TA}, $v_{TA'}$) (m/sec)	Debye temperatures θ_{LA}, θ_{TA}, $\theta_{TA'}$ (K)	mode Gruneisen parameters $\gamma_{LA}, \gamma_{TA}, \gamma_{TA'}$	Total Gruneisen parameter (γ)
NbCoSn	5852	2912, 2912	242, 182, 184	1.71, 1.52, 1.46	1.67
OS1	6109 (6315)	2842, 2902 (3150, 3265)	179, 176, 178 (185, 183, 184)	1.57, 1.33, 1.35 (1.30, 1.05, 1.09)	1.67 (1.61)
OS2	5788 (6087)	2869, 3038 (3038, 3399)	176, 153, 155 (176, 155, 160)	1.58, 1.24, 1.37 (1.55, 1.46, 1.45)	1.68 (1.71)
SQS1	5470 (5382)	2713, 3403 (2570, 3848)	161, 146, 147 (183, 168, 168)	1.67, 1.64, 1.64 (1.70, 1.91, 1.54)	1.70 (1.75)
SQS2	5290	3223, 3223	135, 113, 121	1.53, 1.31, 1.48	1.68

Figure 4.13 illustrates the lattice thermal conductivity of various structures for both systems. As evident from the plots, the lattice thermal conductivity at a given temperature decreases with increasing disorder in the system. For Nb_2Co_2InSb at 300 K, the ordered structure

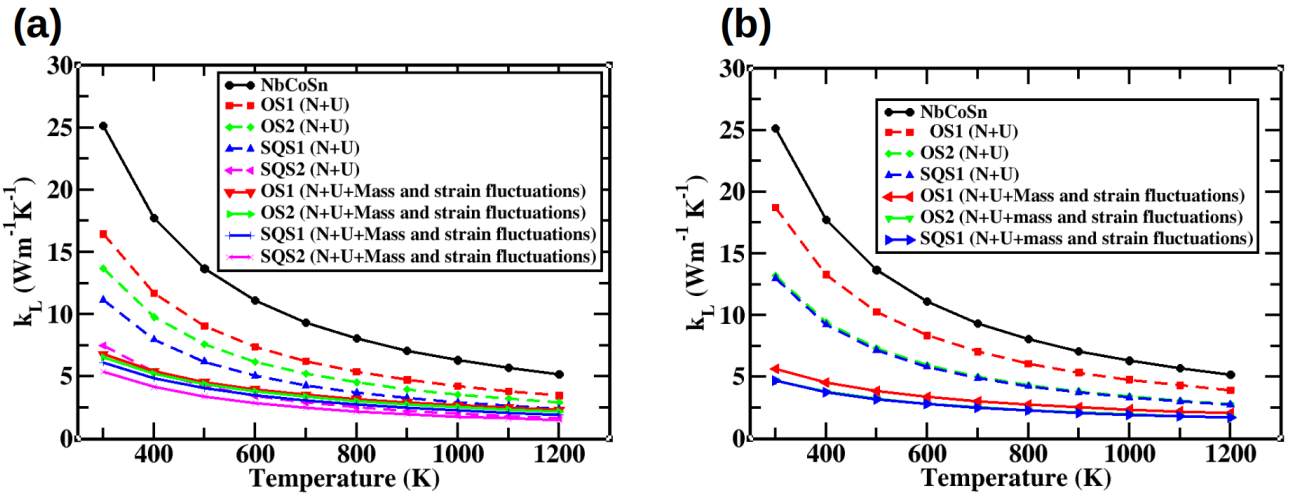

Figure 4.13: Lattice thermal conductivity as a function of temperature for different structural phases of (a) Nb_2Co_2InSb and (b) Nb_2Co_2GaSb.

OS1 exhibits the highest lattice thermal conductivity of 16.45 (6.78) $Wm^{-1}K^{-1}$ without (with) mass and strain fluctuation scattering, while the disordered structure SQS2 shows the lowest values of 7.49 (5.40) $Wm^{-1}K^{-1}$ without (with) mass and strain field fluctuation scattering. Similarly, for Nb_2Co_2GaSb at 300 K, OS1 has the highest lattice thermal conductivity of 18.71 (5.66) $Wm^{-1}K^{-1}$ without (with) mass and strain field fluctuation scattering, whereas SQS1 has the lowest values of 12.99 (4.70) $Wm^{-1}K^{-1}$ without(with) mass and strain field fluctuation scattering. Notably, the lattice thermal conductivity of these double half-Heusler compounds is approximately one-fifth that of the corresponding ternary half-Heusler compound, NbCoSn.

4.3.5 Limitations of Deformation potential theory and Debye-Callaway model

In addition to deformation potential theory, another important electron scattering mechanism in half-Heusler systems is polar optical phonon scattering. In these materials, lattice vibrations can influence charge carriers through multiple channels. Besides modifying the electronic band edges via the deformation potential, lattice vibrations can also induce an electric polarization. In the case of optical phonons, the relative out-of-phase motion of positively and negatively charged ions generates a time-dependent dipole moment. This oscillating dipole produces an electric field that interacts with charge carriers, thereby

introducing an additional scattering mechanism associated with polar optical phonons. Half-Heusler compounds are moderately polar in nature, and therefore polar optical phonon scattering can contribute to a reduction in the electronic relaxation time.
Apart from scattering by acoustic and optical phonon modes, the electrons can also be scattered by ionised impurities, which limit the mobility of charge carriers in doped semiconductors and thermoelectric materials. When a semiconductor is doped, some atoms donate or accept electrons and become ionized impurities (charged centers). These charged impurities create long-range Coulomb potentials that interact with conduction electrons (or holes). As charge carriers move through the crystal, they are deflected by these electrostatic fields, resulting in scattering. This process reduces the carrier mobility and therefore affects the electrical conductivity. The strength of ionized impurity scattering depends strongly on the concentration of dopants and the temperature. At low temperatures and high doping concentrations, this mechanism often dominates carrier scattering because phonon populations are relatively small. As temperature increases, phonon scattering gradually becomes more important and may dominate transport. In theoretical treatments, this mechanism is commonly described using the Brooks–Herring [121] and Conwell–Weisskopf [122] models, which account for screening of the impurity potential by free carriers in the material. However, the overall impact of these scattering mechanisms on the thermoelectric figure of merit ZT is expected to be limited. This is because a reduction in relaxation time affects both the electrical conductivity and the electronic contribution to the thermal conductivity in a similar manner, leading to a partial cancellation of their effects on ZT.
Furthermore, for all parent compounds considered in this work, the lattice thermal conductivity is overestimated compared to calculations that explicitly include three-phonon scattering processes. In addition, experimentally reported lattice thermal conductivity values are generally lower than the present theoretical results [93, 123]. This overestimation of lattice thermal conductivity in the present calculations tends to reduce the predicted value of ZT. Consequently, the combined effects of an overestimated electronic relaxation time and lattice thermal conductivity are expected to have a negligible net influence on the calculated thermoelectric figure of merit.

4.3.6 Figure of merit

The electronic transport properties were combined with lattice thermal conductivity to compute the dimensionless figure of merit (zT) as a function of carrier concentration at different temperatures. Figure 4.14 presents the zT values for both electron and hole doping

at 1000 K. As shown in the figure, the highest zT for Nb_2Co_2InSb is achieved for the SQS2 structure, while for Nb_2Co_2GaSb, the OS2 structure exhibits the best performance. For NbCoSn, the maximum zT value in the n-type case is 0.25 at a carrier concentration of 1.88×10^{21} cm^{-3}, whereas in the p-type case, it reaches 0.10 at 4.35×10^{21} cm^{-3}. In Nb_2Co_2InSb (n-type), the peak zT values for OS1, OS2, SQS1, and SQS2 are 0.98, 0.99, 1.05, and 1.55 at carrier concentrations of 1.19×10^{21}, 8.36×10^{20}, 7.72×10^{20}, and 9.32×10^{20} cm^{-3}, respectively. For the p-type case, the corresponding peak values are 0.79, 1.44, 0.35, and 2.36 at 1.57×10^{21}, 2.56×10^{20}, 1.20×10^{21}, and 6.64×10^{20} cm^{-3}. In the case of Nb_2Co_2GaSb (n-type), OS1, OS2, and SQS1 show maximum zT values of 1.85, 2.35, and 2.01 at carrier concentrations of 6.54×10^{20}, 2.95×10^{20}, and 4.87×10^{20} cm^{-3}, respectively. For the p-type case, the highest zT values are 1.08, 2.09, and 0.54 for OS1, OS2, and SQS1 at carrier concentrations of 7.23×10^{20}, 4.30×10^{20}, and 1.21×10^{21} cm^{-3}, respectively.

Figure 4.15 presents the peak zT values as a function of temperature. Among the different structures of Nb_2Co_2InSb, SQS2 exhibits the highest thermoelectric performance. In contrast, for Nb_2Co_2GaSb, the OS2 configuration outperforms the other structures. As shown in Figure 4.15, at 1200 K, the peak zT values for SQS2 of Nb_2Co_2InSb are 1.73 for n-type and 2.34 for p-type doping. For OS2 of Nb_2Co_2GaSb, the corresponding values at the same temperature are 2.61 (electrons) and 2.31 (holes). These are notably higher than those for NbCoSn, which reaches a maximum zT of only 0.32 for n-type and 0.12 for p-type carriers at 1200 K.

4.3.7 Conclusion

Apart from SQS2 of Nb_2Co_2InSb, all the structures of both the systems are dynamically stable. The lattice thermal conductivity of these structures is approximately one-fifth that of the ternary half-Heusler compound NbCoSn. This reduction is attributed to mass and strain field fluctuation scattering, which has a more pronounced impact on the ordered structures compared to the disordered ones.

A high figure of merit (zT) was observed for these materials, with values of 1.73 (2.34) for electrons (holes) in the SQS2 structure of Nb_2Co_2InSb, and 2.61 (2.31) for electrons (holes) in the OS2 structure of Nb_2Co_2GaSb at 1200 K. These zT values are significantly higher than the corresponding values for NbCoSn, which are 0.32 (0.12) for electrons (holes) at the same temperature.

Due to the high zT values for both electrons and holes, these materials are suitable for

use as both n-type and p-type legs in thermoelectric devices.

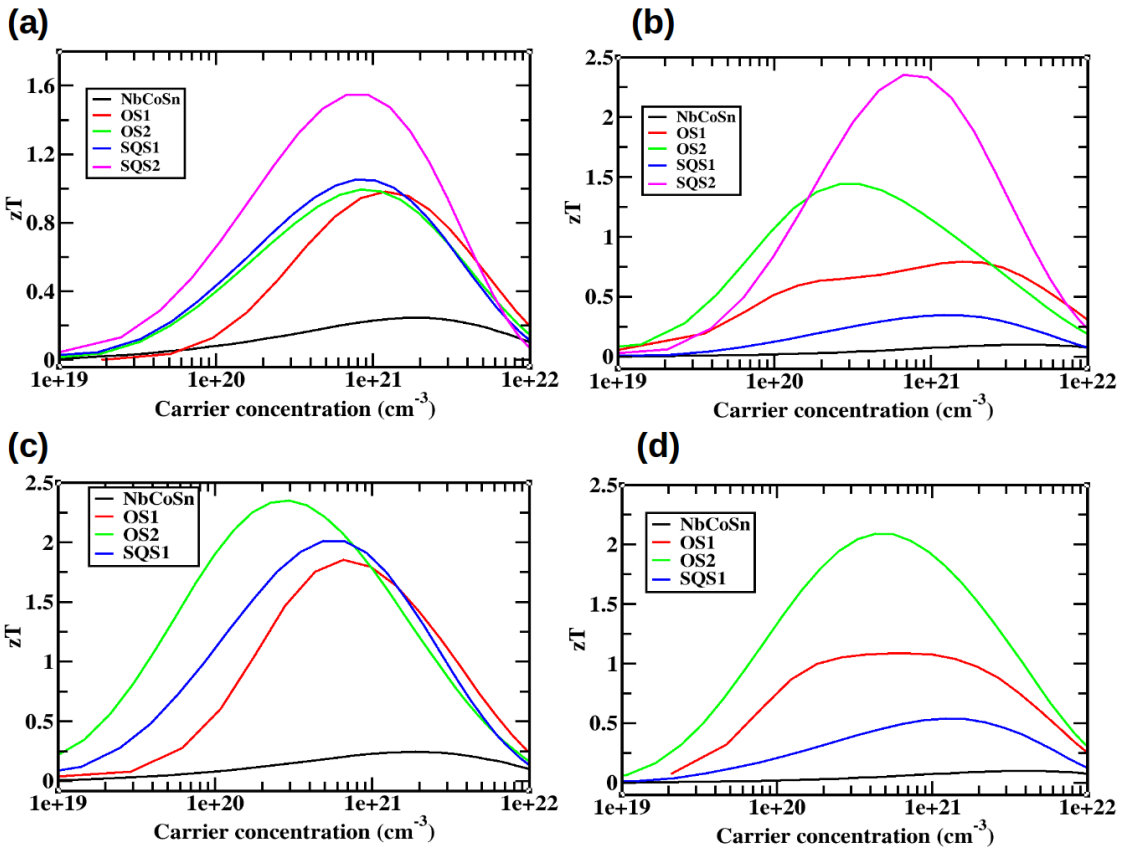

Figure 4.14: Figure pf merit zT at 1000 K as a function of carrier concentration for (a) n-type Nb_2Co_2InSb, (b) p-type Nb_2Co_2InSb , (c) n-type Nb_2Co_2GaSb, and (d) p-type Nb_2Co_2GaSb.

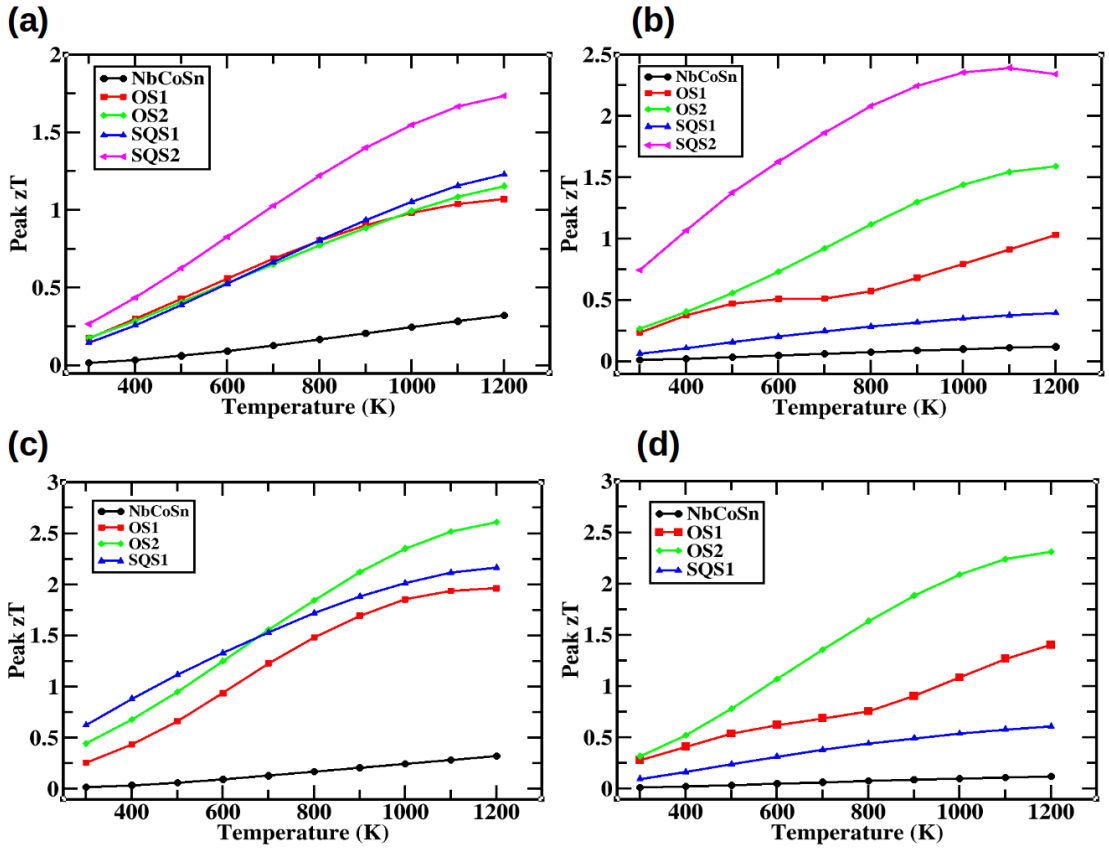

Figure 4.15: Peak value of figure of merit as a function of temperature of (a) n-type Nb_2Co_2InSb, (b) p-type Nb_2Co_2InSb , (c) n-type Nb_2Co_2GaSb, and (d) p-type Nb_2Co_2GaSb.

Chapter 5

Summary and outlook

This thesis comprises two projects, each focused on the computational design and analysis of thermoelectric materials based on half-Heusler and double half-Heusler compounds. The motivation for both studies stems from the need to recover waste heat from various sources, automobile exhausts, industrial furnaces, and domestic heating systems, through thermoelectric energy conversion. Although half-Heusler alloys are known for being mechanically strong, stable at high temperatures, and having good Seebeck coefficients, their biggest drawback is the high lattice thermal conductivity, which severely reduces their overall thermoelectric efficiency. This thesis tackles this challenge using two different strategies, entropy stabilization in the first project and double half-Heusler engineering in the second. The first project, discussed in Chapter 3, explores a novel entropy-stabilized half-Heusler alloy, ZrHfCoNiSnSb. This compound was proposed as a mixed system derived from the parent VEC 18 half-Heuslers ZrNiSn/HfNiSn and HfCoSb/ZrCoSb. The idea of mixing these systems is based on the concept of configurational entropy, which helps stabilize materials that might otherwise be unstable or made of multiple phases—especially at high temperatures. The goal was to see if the resulting high-entropy alloy (HEA) could not only remain thermodynamically and dynamically stable but also have lower lattice thermal conductivity, while still maintaining decent electronic transport properties. Through density functional theory (DFT) and phonon calculations, ZrHfCoNiSnSb was shown to be dynamically stable, as confirmed by the absence of imaginary frequencies in the phonon dispersion spectrum. The compound has a semiconducting band gap of 0.61 eV and exhibits a remarkable reduction in lattice thermal conductivity. Specifically, the computed k_L at 300 K is 5.40 $Wm^{-1}K^{-1}$—a substantial reduction compared to the parent compounds, where parent systems exhibit k_L values exceeding 20 $Wm^{-1}K^{-1}$. This reduction is attributed to the combined effects of mass disorder and bond anharmonicity introduced

through alloying. Using the Debye–Callaway model, it was shown that this reduction primarily arises from enhanced scattering of acoustic phonons. The presence of mass fluctuations further amplifies this effect. Notably, the power factor of ZrHfCoNiSnSb for n-type doping was found to lie intermediate to that of the parent compounds, leading to an enhanced thermoelectric figure of merit. At 1100 K, the zT reaches a value of 1.00, which is approximately 27% higher than the best-performing parent alloy. The work convincingly demonstrates that entropy-driven stabilization and mass disorder are effective strategies to design half-Heusler systems with low thermal conductivity and promising thermoelectric performance.

The second project, presented in Chapter 4, investigates into the theoretical investigation of two double half-Heusler (DHH) systems: Nb_2Co_2InSb and Nb_2Co_2GaSb. These materials were designed by starting from the known half-Heusler compound NbCoSn and applying the concept of valence electron count (VEC) tuning. By replacing Sn with an equal mixture of In and Sb, new quaternary compounds with an overall VEC of 18 were obtained, preserving electronic stability while introducing mass disorder. The motivation here was not just to lower lattice thermal conductivity but to examine how different structural configurations, ordered and disordered, affect thermoelectric performance.

To this end, two ordered structures (OS1 and OS2) and two disordered Special Quasirandom Structures (SQS1 and SQS2) were modeled for each compound, and their vibrational and electronic properties were systematically analyzed. The results show that, with the exception of SQS2 of Nb_2Co_2GaSb, all other phases are dynamically stable. Interestingly, all structures showed much lower lattice thermal conductivity than NbCoSn confirming the effectiveness of phonon scattering induced by mass and strain field fluctuations. At 300 K, the k_L of the SQS2 phase of Nb_2Co_2InSb was found to be as low as 5.40 $Wm^{-1}K^{-1}$, a reduction of nearly 70% compared to NbCoSn. Similar reductions were observed in Nb_2Co_2GaSb, with the lowest k_L around 4.70 $Wm^{-1}K^{-1}$. In terms of electronic transport, ordered structures exhibited superior power factors owing to higher carrier mobilities and more favorable band structures. For Nb_2Co_2GaSb, the OS2 structure yielded the highest zT values of 2.61 for electrons and 2.31 for holes at 1200 K. For Nb_2Co_2InSb, the SQS2 phase exhibited a zT of 1.73 (electrons) and 2.34 (holes) at 1200 K, significantly outperforming the parent NbCoSn compound, which has a maximum zT of only 0.32 at this temperatures. These results highlight that double half-Heusler engineering not only enables drastic reduction in k_L but can also preserve or even improve electronic transport properties, offering a new class of thermoelectric materials with high performance and

phase tunability.

The insights gained from both projects open several promising directions for future research and development in the domain of thermoelectric materials. First and foremost, the theoretical predictions made in this work call for experimental validation. The synthesis of entropy-stabilized ZrHfCoNiSnSb and double half-Heuslers like Nb_2Co_2InSb and Nb_2Co_2GaSb, particularly under high-temperature will test the robustness of the computational results and offer insights into practical processability.

In addition, disorder—whether it comes from the arrangement of elements or the structure itself—plays a key role in controlling how phonons scatter, which in turn affects the lattice thermal conductivity. This insight paves the way for deeper investigation into high-entropy and quaternary systems where disorder can be intentionally tuned using advanced modeling tools like cluster expansion and machine learning-based high-throughput methods. Furthermore, a detailed investigation into how bonding influences the lattice thermal conductivity across various structural phases of double half-Heuslers (DHH) could provide deeper insights into how disorder can be effectively tuned to lower the lattice thermal conductivity.

As the compounds investigated in this work contain transition metal elements with partially filled d orbitals, a systematic study of the influence of Hubbard U interactions on their electronic structure, effective masses, and electronic transport properties would be an interesting direction for future research.

Another promising direction for future work involves solving the full Boltzmann Transport Equation (BTE) by accounting for both three-phonon and four-phonon scattering processes, while also incorporating realistic microstructural features such as grain boundaries and nanostructuring. This comprehensive approach would enable more accurate predictions of thermal conductivity.

From a practical point of view, the fact that these materials show high ZT values for both electrons and holes means they can work as both n-type and p-type parts in a thermoelectric device. This kind of symmetry makes it easier to design efficient and well-matched thermoelectric modules, especially if both parts come from the same type of structure, which also helps simplify the manufacturing process.

Finally, given the environmental importance of sustainable energy, these materials could contribute significantly to waste-heat recovery systems if scalability and long-term thermal stability are demonstrated. Future studies could also explore the oxidation resistance, thermal cycling durability, and interface behavior of these compounds when embedded

into device structures.

In conclusion, this thesis establishes a systematic methodology for designing next-generation thermoelectric materials through entropy stabilization and VEC-guided quaternary engineering. The computational strategies employed herein can serve as a blueprint for discovering and optimizing other complex materials aimed at addressing the global challenge of energy sustainability.

Appendix A

Supplementary Information for Chapter 3

A.1 Crystal structures of the generated SQSs before geometric optimization.

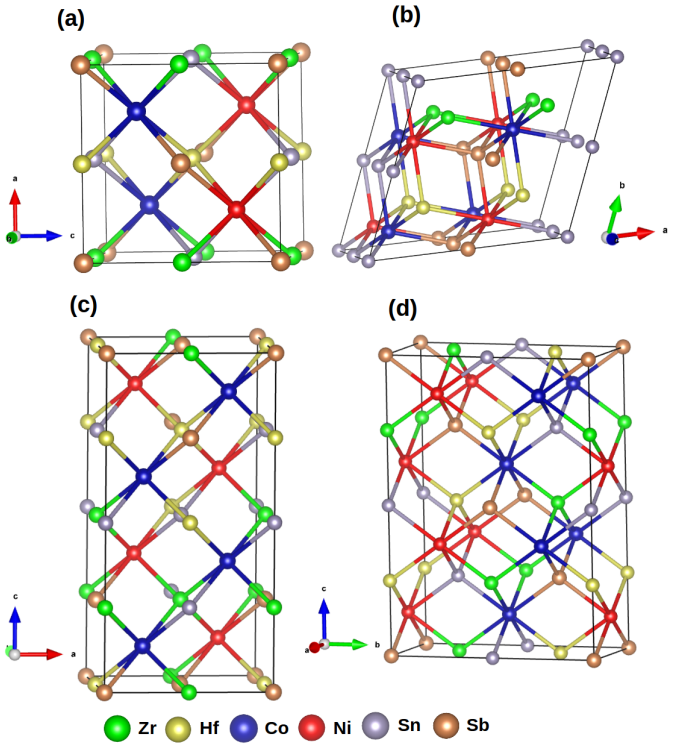

Figure A.1: Crystal structure of the generated SQSs before optimization (a) Conventional unit cell (b) $2 \times 2 \times 2$ supercell (c) Double conventional unit cell (d) unconstrained SQS with 24 atoms

A.2 Comparison of lattice thermal conductivity of the parent compounds

For all the reported ternary parent compounds, the lattice thermal conductivity obtained using the Debye-Callaway model in the present work is systematically higher than the values calculated from three-phonon scattering as well as those measured experimentally. Nevertheless, the overall trend in lattice thermal conductivity remains consistent across all approaches, experimental measurements, three-phonon calculations, and the Debye-Callaway model. Specifically, the ordering of lattice thermal conductivity for the ternary parent systems follows

$$\kappa_L^{\mathrm{ZrCoSb}} > \kappa_L^{\mathrm{HfCoSb}} > \kappa_L^{\mathrm{ZrNiSn}} > \kappa_L^{\mathrm{HfNiSn}}.$$

Irrespective of the method employed, the relative trend is preserved. A comparison of the lattice thermal conductivity values at 300 K is presented in the table below. As evident

Table A.1: Comparison of the lattice thermal conductivity κ_L of the parent compounds at 300 K

	ZrNiSn	HfNiSn	ZrCoSb	HfCoSb
κ_L of the present calculation (Using Debye-Callway model) ($\mathrm{Wm^{-1}K^{-1}}$)	21.51	20.37	28.65	23.84
Reported values (Theoretical) (By solving linearized Boltzmann transport equation) ($\mathrm{Wm^{-1}K^{-1}}$) [7, 107, 124, 125]	19.6, 17.5 15.8	19.5, 15.8 14.6	23.5	19.7
Reported values (experimental) ($\mathrm{Wm^{-1}K^{-1}}$) [126, 127]	6.8	6.3	21.5	14.5

from the table above, the experimentally measured lattice thermal conductivity values for all systems are lower than those obtained from three-phonon scattering calculations, which in turn are lower than the values predicted by the Debye-Callaway model. One important reason for the reduced experimental values is the presence of antisite disorder and other point defects in these half-Heusler compounds [128–130]. Such defects introduce additional phonon-scattering channels, thereby suppressing the lattice thermal conductivity. These defect-induced scattering mechanisms are not explicitly included in the three-phonon or Debye-Callaway calculations, leading to an overestimation of κ_L.

A.3 Band structure comparison of HEA for SOC and without SOC calculations

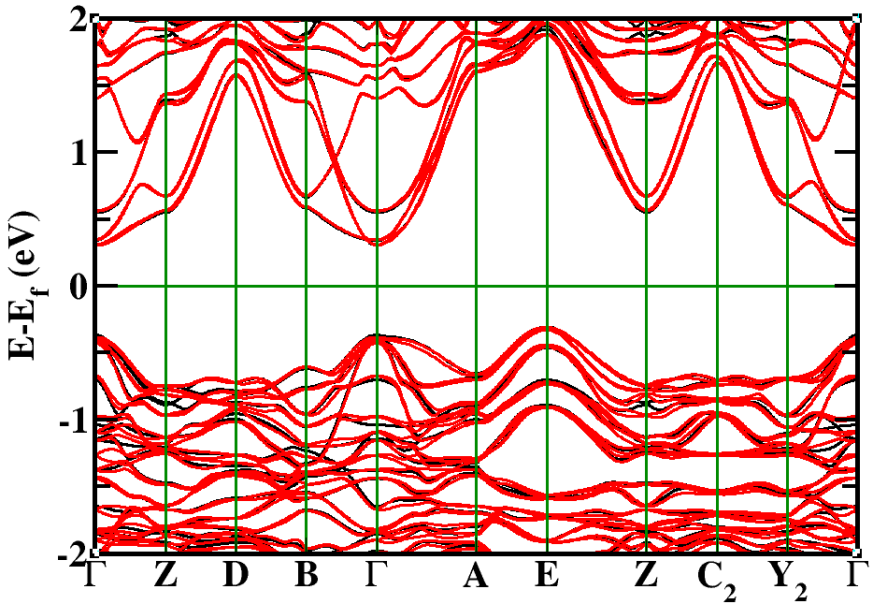

Figure A.2: Band structure comparison of the HEA, showing calculations without spin-orbit coupling (black) and with spin-orbit coupling (red)

A.4 Orbital contributions of different elements

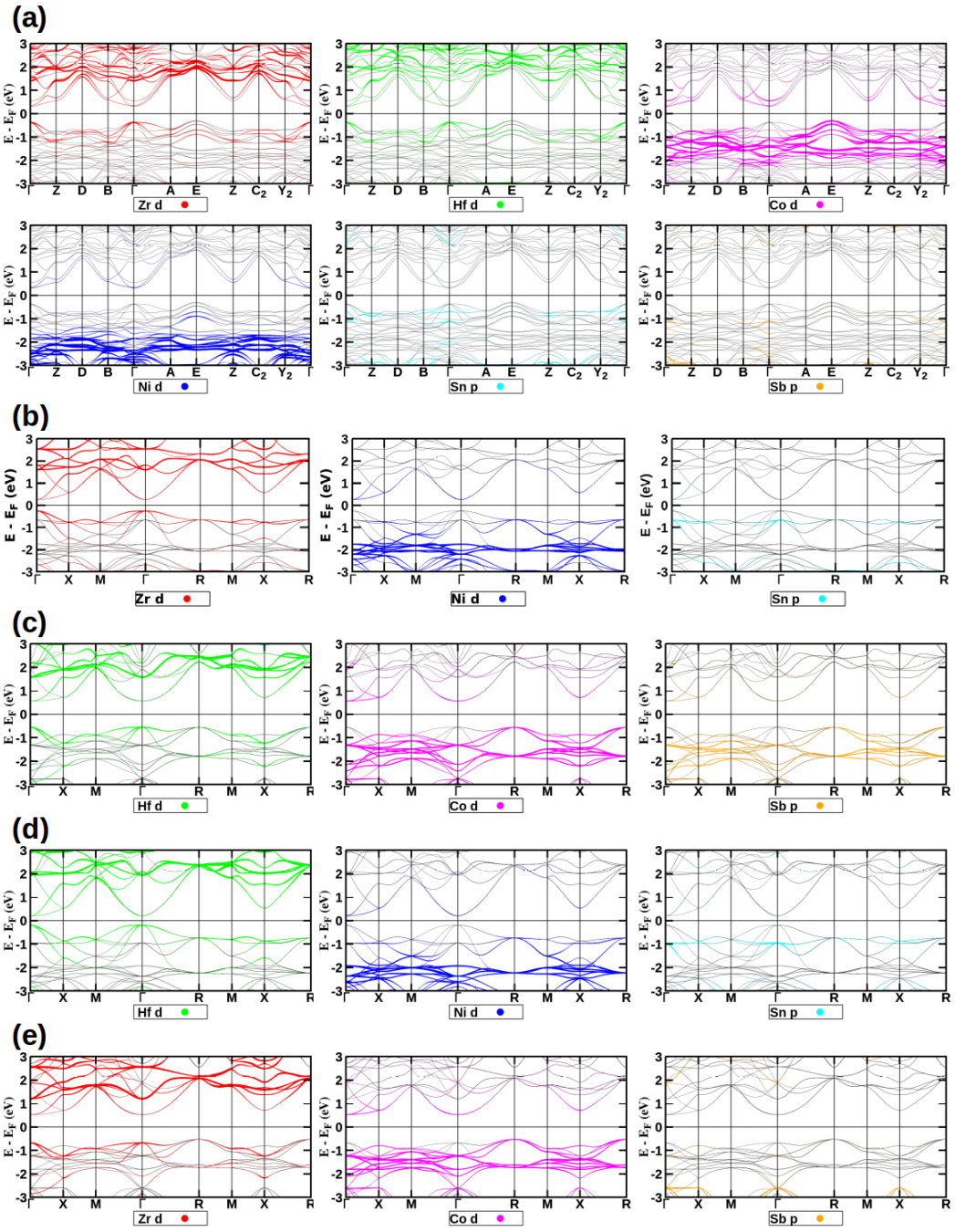

Figure A.3: Atomic orbital contributions to the band structure for (a) ZrHfCoNiSnSb, (b) ZrNiSn, (c) HfCoSb, (d) HfNiSn and (e) ZrCoSb

A.5 Charge density differences of the parent compounds

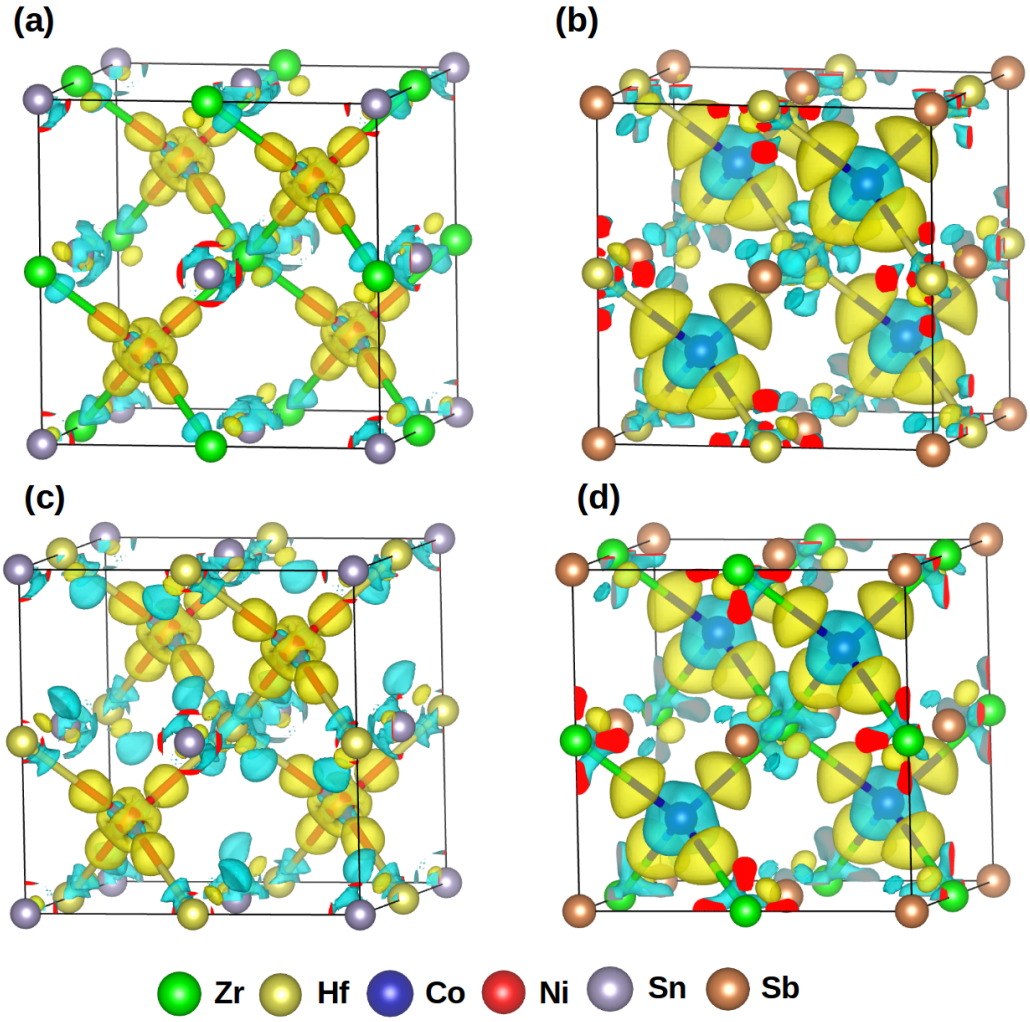

Figure A.4: Isosurfaces of charge density difference ($\Delta\rho$) between the electron density of the parent compounds and that obtained from the superposition of the atomic densities. Yellow (Turquoise) isosurfaces denote accumulation (depletion) of charge density (a) ZrNiSn (b) HfCoSb (c) HfNiSn, and (d) ZrCoSb. The isosurfaces correspond to an isovalue of 0.009 e Bohr^{-3}

A.6 Effective masses of different bands

The conduction band minimum (CBM) of all the parent compounds is located at the Γ point and exhibits triple degeneracy. Among these three bands, two have light and equal effective masses, while the third has a heavy effective mass. In the case of the HEA, both the CBM and a conduction band extremum (CBE) are present, with the CBE positioned 37 meV above the CBM. The corresponding density-of-states and conductivity effective masses are listed in Tables A.13 and A.3.

Table A.2: Dos and conductive effective masses of conduction band minima (CBM) of the parent compounds

Effective masses	ZrNiSn	HfNiSn	ZrCoSb	HfCoSb
m_D^* (Heavy band)	3.33	3.28	5.56	6.96
m_D^* (two light band)	0.42	0.38	1.27	1.09
m_σ^* (Heavy band)	3.33	3.28	5.56	6.96
m_σ^* (two light band)	0.42	0.38	1.27	1.09

Table A.3: Dos and conductive effective masses of conduction band minima (CBM) of ZrHfCoNiSnSb

Band	m_D^*	m_σ^*
CBM	1.04	0.91
CBE	1.19	0.96

ZrNiSn and HfNiSn have their valence band maxima (VBM) at the Γ point, and do not exhibit a valence band extremum (VBE) elsewhere. Three bands contribute to the VBM in both cases: two heavy bands with equal effective masses and one light band. In HfCoSb also, the VBM is located at the Γ point, with three bands contributing to it. Additionally, eight bands contribute to the VBE at the R point. For ZrCoSb, the VBM is located at the R point, with eight bands contributing to it. In the case of ZrHfCoNiSnSb, there are four bands at the E point, among which one corresponds to the VBM and the others to the VBE. Furthermore, three bands at the Γ point are band extrema. The valley degeneracy at the R and E points is 8, which has been considered in calculating the DOS effective masses for the bands at these points. For HfCoSb, the VBE lies 0.005 eV below the VBM. Band indices for different structures are shown in Figure B.5, and the corresponding effective masses are provided in Tables A.4, A.5, A.6, and B.8.

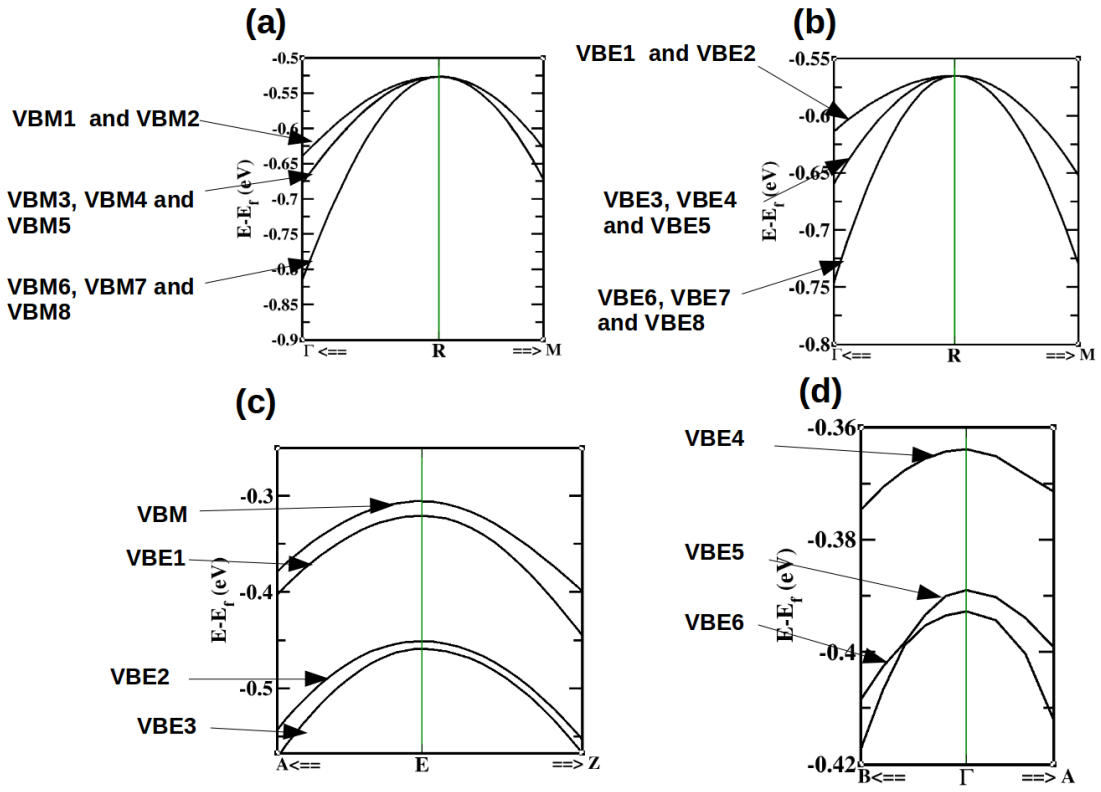

Figure A.5: (a) VBM of ZrCoSb at R point, (b) VBE of HfCoSb at R point, (c) VBM/VBE of ZrHfCoNiSnSb at E point, and (d) VBE of ZrHfCoNiSnSb at Γ point

Table A.4: Dos and conductive effective masses of valence band maxima (VBM) of ZrNiSn and HfNiSn

Effective masses	ZrNiSn	HfNiSn
m_D^* (Two heavy band)	0.87	0.69
m_D^* (Light band)	0.40	0.37
m_σ^* (Two heavy band)	0.87	0.69
m_σ^* (Light band)	0.40	0.37

Table A.5: Dos and conductive effective masses of valence band maxima (VBM) of ZrCoSb

Band	m_D^*	m_σ^*
VBM1	8.65	2.16
VBM2	8.65	2.16
VBM3	6.20	1.55
VBM4	6.20	1.55
VBM5	5.65	1.41
VBM6	4.46	1.11
VBM7	3.33	0.83
VBM8	3.33	0.83

Table A.6: Dos and conductive effective masses of VBM (at Γ point) and VBE (at R point) of HfCoSb

Band	m_D^*	m_σ^*
VBM(Two heavy bands)	0.62	0.62
VBM(One light bands)	0.37	0.37
VBE1	9.56	2.36
VBE2	9.56	2.36
VBE3	6.00	1.50
VBE4	6.00	1.50
VBE5	6.00	1.50
VBE6	4.79	1.14
VBE7	2.98	0.74
VBE8	2.89	0.74

Table A.7: Dos and conductive effective masses of valence band maxima (VBM) at E point and VBE at E point and Γ point of ZrHfCoNiSnSb

Band	m_D^*	m_σ^*	ΔE
VBM	5.40	1.34	0
VBE1	4.62	1.15	0.015
VBE2	5.64	1.33	0.145
VBE3	4.23	1.06	0.153
VBE4	0.66	0.62	0.059
Vis	0.69	0.61	0.084
VBE6	0.52	0.50	0.088

A.7 Transport properties comparison at 900 K

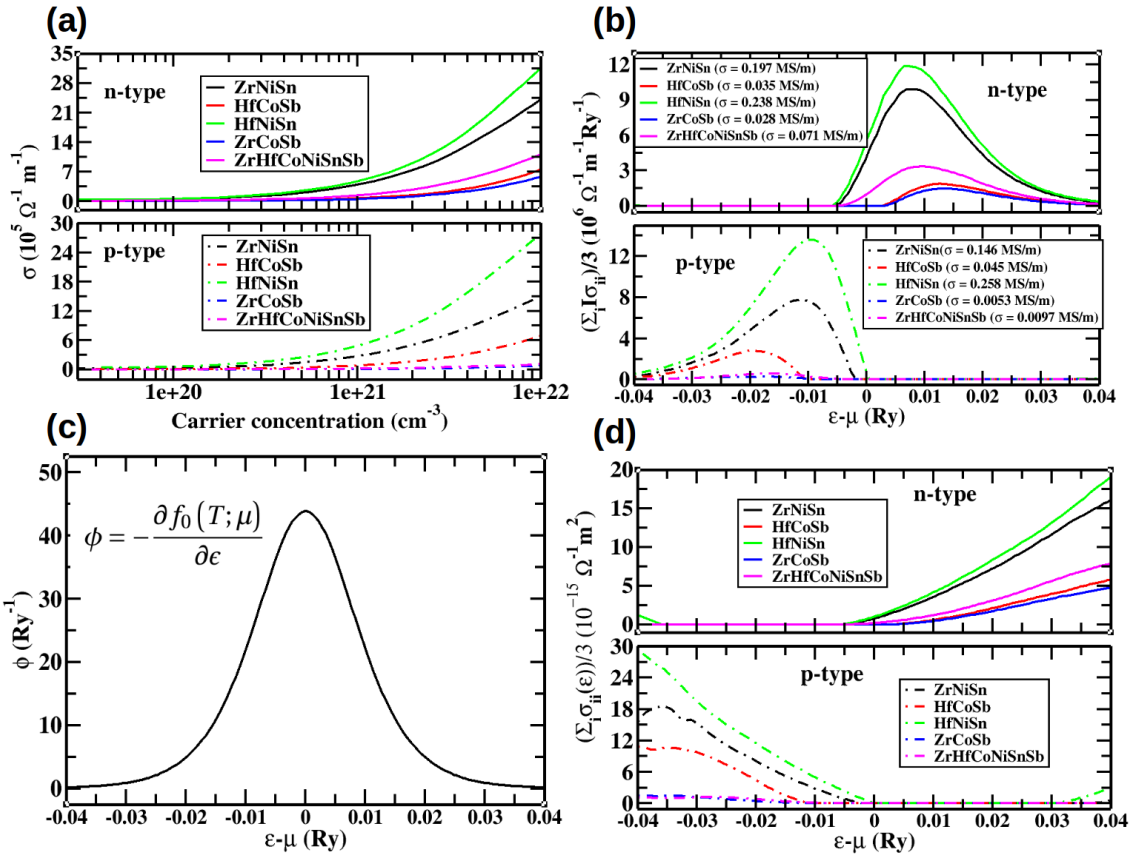

Figure A.6: (a) Electrical conductivity as a function of carrier concentration, (b) average of integrand of electrical conductivity expression as a function of ϵ - μ, (c) selection function ϕ as a function of ϵ - μ, and (d) Average of projected conductivity tensor as a function of ϵ - μ

Figure A.6 (a) presents the variation in electrical conductivity with carrier concentration at 900 K for both the parent compounds and HEA. In the case of n-type conductivity, HfNiSn exhibits the highest electrical conductivity across all carrier concentrations, followed by ZrNiSn, ZrHfCoNiSnSb, HfCoSb, and ZrCoSb in descending order. For the p-type case, a similar trend is observed, with HfNiSn showing the highest conductivity, followed by ZrNiSn, HfCoSb, ZrHfCoNiSnSb, and ZrCoSb.

This trend in electrical conductivity can be understood by analyzing the integrand of the expression of electrical conductivity $\sigma_{ij}(T;\mu)$ (Equation 2.55 of Chapter 2) for different values of the chemical potential μ. Figure A.6(b) illustrates the integrand of the averaged electrical conductivity tensor $\mathrm{I}\sigma_{ii}(T;\mu)$ as a function of ϵ -μ, where μ

corresponds to a carrier concentration of 5×10^{20} cm^{-3}. The total electrical conductivity is determined by the integral of these curves, representing the area under them. This specific carrier concentration is chosen because the figure of merit for ZrHfCoNiSnSb reaches its maximum around this value for the n-type case at 900K, making it an interesting point for investigating transport properties. Similar analyses can be conducted for other carrier concentrations. For the n-type case, the chemical potential for this carrier concentration is 81 meV above CBM for ZrNiSn, 90 meV above CBM for HfNiSn, and 80 meV above CBM for ZrHfCoNiSnSb, while for HfCoSb and ZrCoSb, it lies 30 meV and 35 meV below CBM, respectively, within the bandgap. Similarly, for the p-type case, it is 3 meV below VBM for HfNiSn, whereas for ZrNiSn, HfCoSb, ZrCoSb, and ZrHfCoNiSnSb, it is positioned 25 meV, 140 meV, 115 meV, and 40 meV above VBM, respectively, within the bandgap.

The electrical conductivity integrand, I$\sigma_{ii}\,(T;\mu)$, consists of the projected conductivity $\sigma_{ii}(\epsilon)$, shown in Figure A.6 (d), weighted by the selection function ϕ, which is plotted in Figure A.6(c). The projected conductivity at different energy values is calculated using the BoltzTraP1 code [67]. Since the selection function decreases to approximately 99% of its peak value around ± 0.04 Ry from the chemical potential, the most significant contribution of the projected conductivity tensor to electrical conductivity arises within this energy range.

As depicted in Figure A.6(d), for the n-type case, the projected conductivity within this energy window is highest for HfNiSn, followed by ZrNiSn, ZrHfCoNiSnSb, HfCoSb, and ZrCoSb. For the p-type case, HfNiSn again exhibits the highest projected conductivity, followed by ZrNiSn, HfCoSb, ZrHfCoNiSnSb, and ZrCoSb. Consequently, across the entire relevant energy range around the chemical potential, the trend in projected conductivity aligns with the trend observed in electrical conductivity (Figure A.6(a)). Thus, for both the n-type and p-type cases, the order of electrical conductivity follows from the corresponding projected conductivity, reinforcing the observed hierarchy among the compounds.

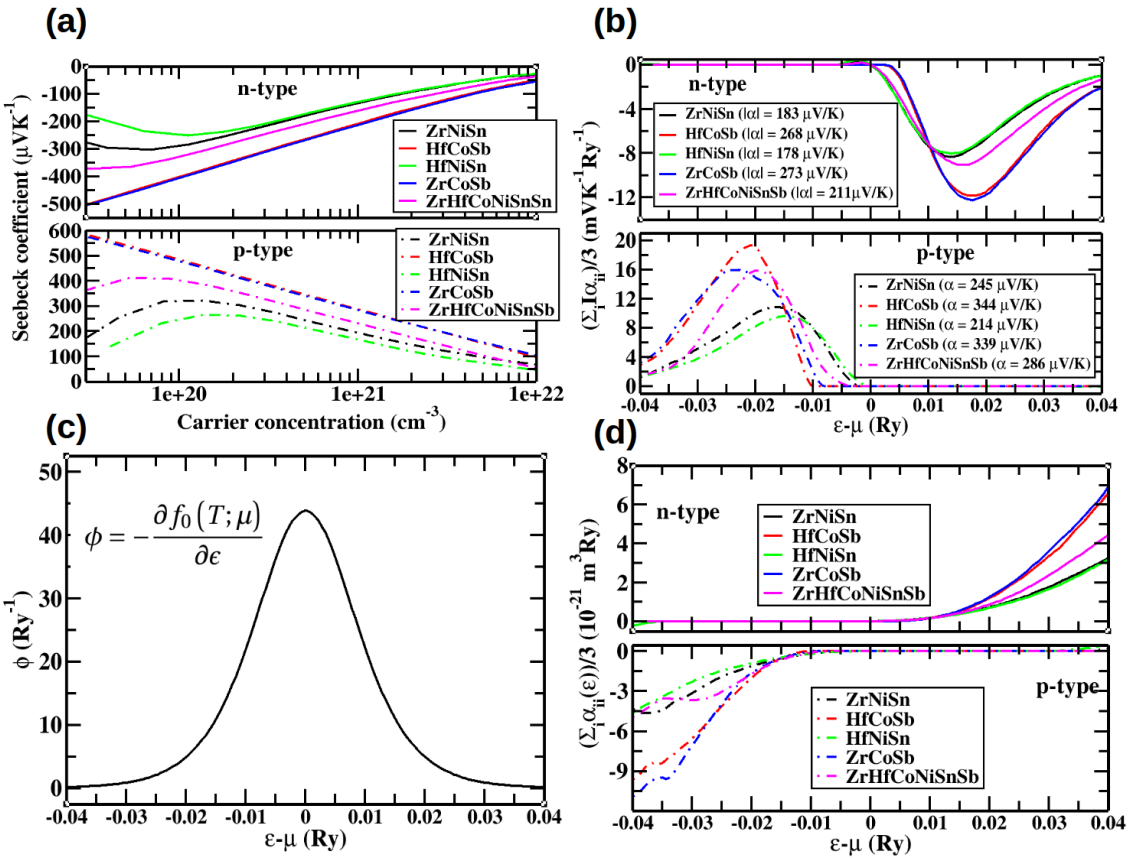

Figure A.7: (a) Seebeck coefficient as a function of carrier concentration, (b) average of integrand of Seebeck coefficient expression as a function of ϵ - μ, (c) selection function ϕ as a function of ϵ - μ, and (d) Average of projected Seebeck tensor as a function of ϵ -μ

Figure A.7 (a) presents the Seebeck coefficient as a function of carrier concentration at 900 K for different structures. From the plot, it is evident that for the n-type case, ZrCoSb exhibits the highest Seebeck coefficient, followed by HfCoSb, ZrHfCoNiSnSb, ZrNiSn, and finally HfNiSn. For the p-type case, HfCoSb has the highest Seebeck coefficient, followed by ZrCoSb, ZrHfCoNiSnSb, ZrNiSn, and HfNiSn.

Similar to the previous case, the integrand of the expression for the Seebeck coefficient, I$\alpha_{ii}\,(T;\mu)$ (Equation 2.57 of Chapter 2), is plotted in Figure A.7(b) as a function of ϵ - μ for the chemical potential corresponding to a carrier concentration of 5×10^{20} cm^{-3}. The Seebeck coefficient is determined by the area under these curves. This integrand primarily consists of the projected Seebeck tensor $\alpha_{ii}(\epsilon)$, weighted by the selection function. The projected Seebeck tensor is defined as:

$$\alpha_{ii}(\epsilon) = \sum_{k} \sigma_{ik}^{-1}(T;\mu)\,(\epsilon\text{-}\mu)\,\sigma_{ki}(\epsilon) \tag{A.1}$$

Figure A.7 (d) illustrates the plot of the average projected Seebeck tensor as a function of ϵ -μ for different structures. As observed from the plot, for the n-type case, the average projected Seebeck tensor attains its maximum value within the relevant energy range (-0.04 to 0.04 Ry around μ) for ZrCoSb, followed by HfCoSb, ZrHfCoNiSnSb, ZrNiSn, and HfNiSn. This trend in the projected Seebeck tensor directly explains the ordering of the Seebeck coefficient for the n-type case, as shown in Figure A.7(a).

For the p-type case, although there are fluctuations in the projected Seebeck tensor values between ZrCoSb and HfCoSb, as well as between ZrHfCoNiSnSb and ZrNiSn, the dominant energy region where the selection function has significant weight (-0.02 to 0 Ry around μ) shows HfCoSb having the highest projected Seebeck tensor value, followed closely by ZrCoSb. This indicates that the Seebeck coefficient of HfCoSb is slightly higher than that of ZrCoSb.

Although ZrHfCoNiSnSb has a projected Seebeck tensor value close to that of ZrCoSb in the energy range between -0.02 and 0 Ry, for energies lower than -0.02 Ry, about μ, the projected Seebeck tensor for ZrCoSb exceeds that of ZrHfCoNiSnSb. This explains why ZrCoSb has a higher Seebeck coefficient than ZrHfCoNiSnSb in the p-type case. Similarly, within the -0.02 to 0 Ry energy range around μ, the projected Seebeck tensor for ZrHfCoNiSnSb is greater than that of ZrNiSn, followed by HfNiSn, explaining the observed trend among these structures.

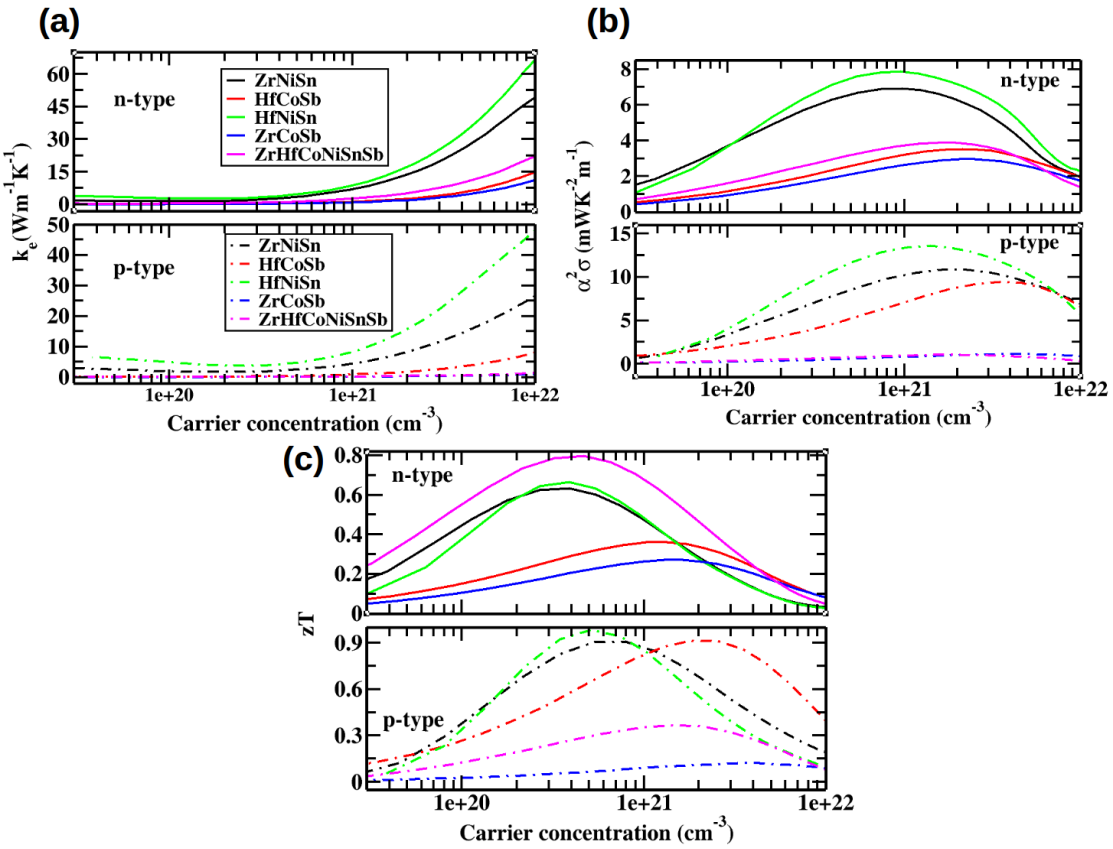

Figure A.8: (a) Electronic thermal conductivity, (b) Power factor and (c) Figure of merit as a function of carrier concentration at 900 K

A.8 Carrier concentration for peak value of figure of merit

Table A.8: Carrier concentration for n-type case for the peak value of the figure of merit (in the unit of 10^{20} cm^{-3})

Temperature	ZrNiSn	HfCoSb	HfNiSn	ZrCoSb	ZrHfCoNiSnSb
300 K	1.16	5.68	1.14	5.82	1.68
900 K	3.87	13.4	3.88	12.8	4.66

Table A.9: Carrier concentration for the p-type case for the peak value of figure of merit (in the unit of 10^{20} cm^{-3})

Temperature	ZrNiSn	HfCoSb	HfNiSn	ZrCoSb	ZrHfCoNiSnSb
300 K	2.02	10.5	1.60	57.2	11.1
900 K	7.92	18.2	5.14	43.1	14.1

A.9 Transformation matrices for McSQSs and conditions for calculating E_f

Transformation matrix for best McSQS obtained using ATAT software and used in the calculations :

$$\text{Type I} : \begin{pmatrix} 1 & 0 & 0 \\ 0 & 1 & 0 \\ 0 & 0 & 1 \end{pmatrix} \quad \text{(A.2)} \qquad \text{Type II} : \begin{pmatrix} 1 & 0 & 0 \\ 0 & 1 & 0 \\ 0 & 0 & 2 \end{pmatrix} \quad \text{(A.3)}$$

$$\text{Type III} : \begin{pmatrix} 1 & 0 & 1 \\ 0 & 1 & 1 \\ 1 & 1 & 0 \end{pmatrix} \quad \text{(A.4)} \qquad \text{Type IV} : \begin{pmatrix} 0.5 & -0.5 & 0 \\ -1 & -1 & 0 \\ 0 & 0 & -2 \end{pmatrix} \quad \text{(A.5)}$$

The energy E_f in Equation (7) represents the total energy difference between HEA and the constituent elements in their most stable standard states at 0 K as obtained from first-principles calculations. Specifically:

- **Zr**: Hexagonal close-packed (hcp) structure
- **Hf**: Hexagonal close-packed (hcp) structure

- **Co**: Hexagonal close-packed (hcp) structure
- **Ni**: Face-centered cubic (fcc) structure
- **Sn**: FCC structure (space group $Fd\bar{3}m$)
- **Sb**: Rhombohedral structure (space group: $R\bar{3}m$)

All elemental reference energies were computed using density functional theory (DFT) within the GGA-PBE exchange-correlation functional approximation. The electron-ion interactions were described using ultrasoft pseudopotentials. The calculations were performed at 0 K without zero-point energy corrections. A sufficiently dense k-point mesh and energy cutoff (as shown in the Table A.10) were used to ensure convergence of total energies to within 1 meV per formula unit.

Table A.10: k-mesh, kinetic energy cutoff for wave function and charge density used for the bulk constituent elements in the calculations.

Parameters	Zr	Hf	Co	Ni	Sn	Sb
k-mesh	10 × 10× 7	10 × 10× 7	10 × 10× 7	14 × 14× 14	14 × 14× 14	10 × 10× 10
Kinetic energy cutoff for wave function (Ry)	45	50	35	50	60	40
Kinetic energy cutoff for charge density (Ry)	360	400	280	400	480	320

For the HEA ZrHfCoNiSnSb, the above conditions are mentioned in the main text.

A.10 Convergence analysis with 96-atom SQS structures

To assess whether a 12-atom cell is sufficient to capture the extensive configurational disorder, we performed a convergence analysis using larger supercells. Specifically, we generated 10 Special Quasirandom Structures (SQSs) each comprising 96 atoms, constructed as $2 \times 2 \times 2$ supercells of the conventional unit cell of ZrHfCoNiSnSb. All 96-atom structures were fully relaxed (lattice parameters and atomic positions were optimized), and we computed the average bond lengths and bond orders between various atomic pairs for each of the SQSs. Bond orders were obtained using the Chargemol software, employing the DDEC method [131]. The averaging was performed over all

neighboring atom pairs with interatomic distances less than 3 Å , regardless of whether the atoms were within the same unit cell. Subsequently, these bond length and bond order values were averaged over all 10 SQS configurations. For comparison, we also generated ten 12-atom SQS structures similar to Type I. The lattice parameters and atomic positions of these structures were fully optimized. We found that these 12-atom SQSs were energetically equivalent, with energy differences of the order of 1 meV across the different configurations. Moreover, the variations in the corresponding lattice parameters and the angles between them across the structures were negligible (on the order of 10^{-3}Å and 10^{-3} degrees). we repeated the same analysis for these energetically equivalent 12-atom structures. The Fig. A.9 below presents a comparative plot of the averaged bond lengths and bond orders between different atomic pairs for both the 12-atom and 96-atom SQS ensembles.

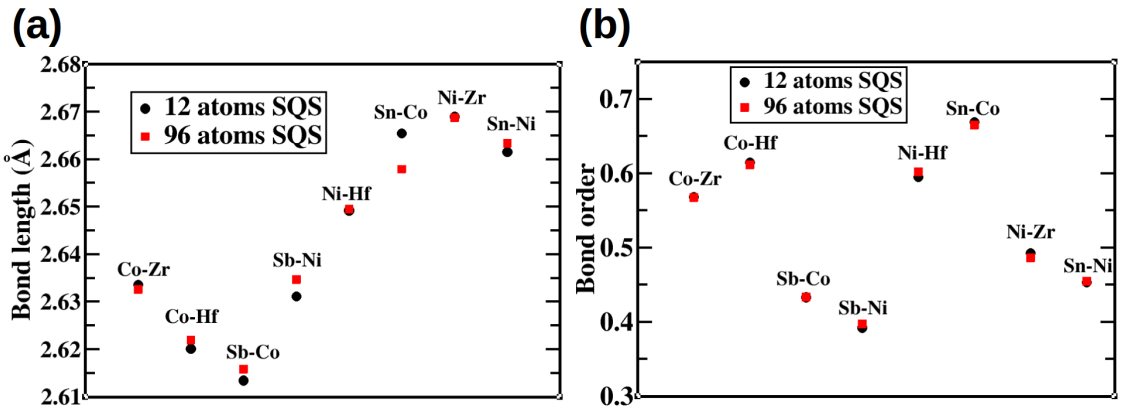

Figure A.9: Comparison of the average of the (a) bond length of 12 atoms SQSs with 96 atoms SQSs (b)bond order of 12 atoms SQSs with 96 atoms SQSs

As evident from the plots, the bond lengths and bond orders—which reflect how charge is shared between atoms and thus partially characterize the local chemical environment—show excellent agreement between the 12-atom and 96-atom SQS structures. This indicates that the 12-atom SQS effectively captures the essential features of the extensive configurational disorder present in the larger 96-atom systems.

A.11 Segregation kinetics and possibility of secondary phases

The high-entropy alloy ZrHfCoNiSnSb can be considered as a configurational mixture derived from eight constituent half-Heusler (HH) phases: four **VEC = 18** systems (ZrNiSn, HfCoSb, HfNiSn, ZrCoSb), two **VEC = 17** systems (ZrCoSn, HfCoSn), and two **VEC = 19** systems (ZrNiSb, HfNiSb). Based on this, the configurational entropy is calculated using the relation

$$\Delta S_{\text{config}} = k_B \ln \Omega$$

Since $\Omega = 8$, the resulting entropy is

$$\Delta S_{\text{config}} = 2.079\, k_B.$$

This configurational entropy is the same as given in Equation 11 of the main manuscript (only computed by taking into account constituent configurations). Given that the VEC 17 and VEC 19 half-Heusler compounds are thermodynamically unstable due to their low formation energies, it is sufficient to assess the stability of ZrHfCoNiSnSb relative to the VEC 18 constituents. These VEC 18 half-Heuslers (ZrNiSn, HfCoSb, HfNiSn, and ZrCoSb) are already known to be stable with respect to both their elemental constituents and relevant binary phases.

Additionally, data from the Open Quantum Materials Database (OQMD) suggests that the only notable competing phases for this system are ZrNiSn and HfCoSb. Furthermore, the calculated formation energy of the HEA, ZrHfCoNiSnSb from bulk atoms, is significantly negative ($\Delta H_f =$ - 0.75 eV per atom as mentioned in the main manuscript), confirming its thermodynamic stability against decomposition into elemental solids. This makes the likelihood of secondary phase segregation into elemental constituents quite low.

Therefore, the relevant competing phases to consider in the phase segregation analysis are the stable VEC 18 half-Heuslers: ZrNiSn, HfCoSb, HfNiSn, and ZrCoSb. The chemical reaction corresponding to their potential segregation can thus be written as:

$$\text{ZrHfCoNiSnSb} \longrightarrow 0.5\,(\text{ZrNiSn} + \text{HfCoSb} + \text{HfNiSn} + \text{ZrCoSb}) \tag{A.6}$$

The corresponding mixing enthalpy is given by:

$$\Delta H_{mix} = \sum_i x^i E_i^{\text{config}} \text{ - } E^{\text{ZrHfCoNiSnSb}} \tag{A.7}$$

Here, x^i and E_i^{config} denote the fractional contribution and configurational energy of the i-th configuration, respectively. For the current case, all configurations contribute equally with $x^i = 0.5$. The term $E^{\text{ZrHfCoNiSnSb}}$ refers to the total energy of the high-entropy alloy (HEA) ZrHfCoNiSnSb.
Similarly, the corresponding changes in vibrational energy (ΔH_p) and vibrational entropy (ΔS_p)—also referred to as phonon energy and phonon entropy in chapter 3—associated with the reaction A.6 are given by:

$$\Delta H_p = \sum_i x^i H_{p,i}^{\text{config}} \text{ - } H_p^{\text{ZrHfCoNiSnSb}} \tag{A.8}$$

and

$$\Delta S_p = \sum_i x^i S_{p,i}^{\text{config}} \text{ - } S_p^{\text{ZrHfCoNiSnSb}} \tag{A.9}$$

Where corresponding phonon energy (or vibrational energy) $H_{p,i}$ and phonon entropy (or vibrational entropy) $S_{p,i}$ of each of the constituent configurations and HEA is given by equations 3.9 and 3.10 of Chapter 3.

Using the above equations, the total change in the Gibbs free energy $\Delta G(T)$ as a function of temperature T is given by :

$$\Delta G(T) = [\Delta H_{mix} + \Delta H_p \text{ - } T\,(\Delta S_p + \Delta S_{config})] \tag{A.10}$$

In the above equation, the contribution of phonons to the total Gibbs free energy (ΔG_p) is given by :

$$\Delta G_p = \Delta H_p \text{ - } T\Delta S_p \tag{A.11}$$

This $\Delta G(T)$ was calculated and plotted as shown in the Fig. A.10:

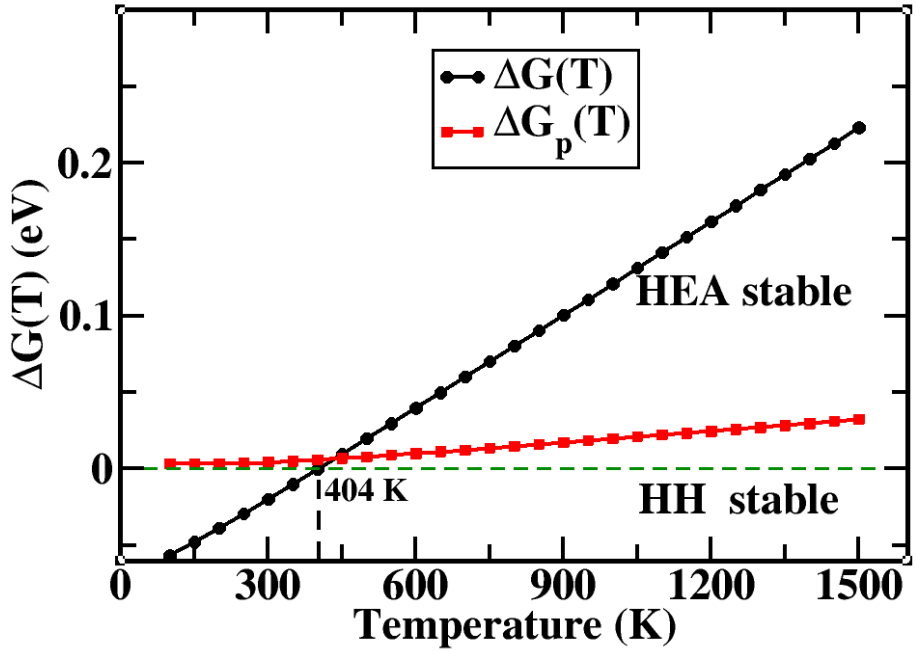

Figure A.10: $\Delta G(\mathrm{T})$ as a function of temperature

As illustrated in the plot above, the contributions of vibrational energy and vibrational entropy to the total Gibbs free energy are negligible. The primary contributions arise from the mixing enthalpy ΔH_{mix} and configurational entropy ΔS_{config}. From the plot, it is evident that ΔG becomes positive above 404 K, indicating that the HEA is thermodynamically stable against phase segregation into the constituent half-Heuslers at temperatures exceeding this value. This transition temperature lies approximately midway between the temperatures reported in Chapter 3.

This observation aligns with the fact that the ΔH_{mix} used here corresponds to the average of ΔH_e values from Reaction 8 and Reaction 9 in the main text. Since the typical synthesis temperature of these materials is around 1500 K, the HEA ZrHfCoNiSnSb can be readily synthesized at such high temperatures, where it is more stable than its constituent half-Heuslers. Moreover, its stability at lower temperatures can be preserved via quenching—a rapid cooling technique. Quenching inhibits atomic diffusion required for phase transformation, thereby locking in the high-temperature phase. This technique effectively prevents the transition to lower-energy phases by suppressing the kinetics of phase segregation during cooling.

Possibility of other secondary phases:

Since the aforementioned half-Heusler compounds are more stable than the high-entropy alloy (HEA) at low temperatures, there exists a possibility of phase segregation into these half-Heuslers under such conditions. Additionally, during the synthesis of these half-Heuslers, other secondary phases have been observed—for example, Ni_3Sn_4, $ZrNi_2Sn$, and $HfNi_2Sn$ under Ni-rich conditions [132], as well as $HfCo_2Sb$ and HfSb (according to OQMD), and Co and ZrSb (also from OQMD). Therefore, a subset of these secondary phases may potentially be present in the HEA as well.

A.12 Phonon band structure comparison with and without LO–TO splitting

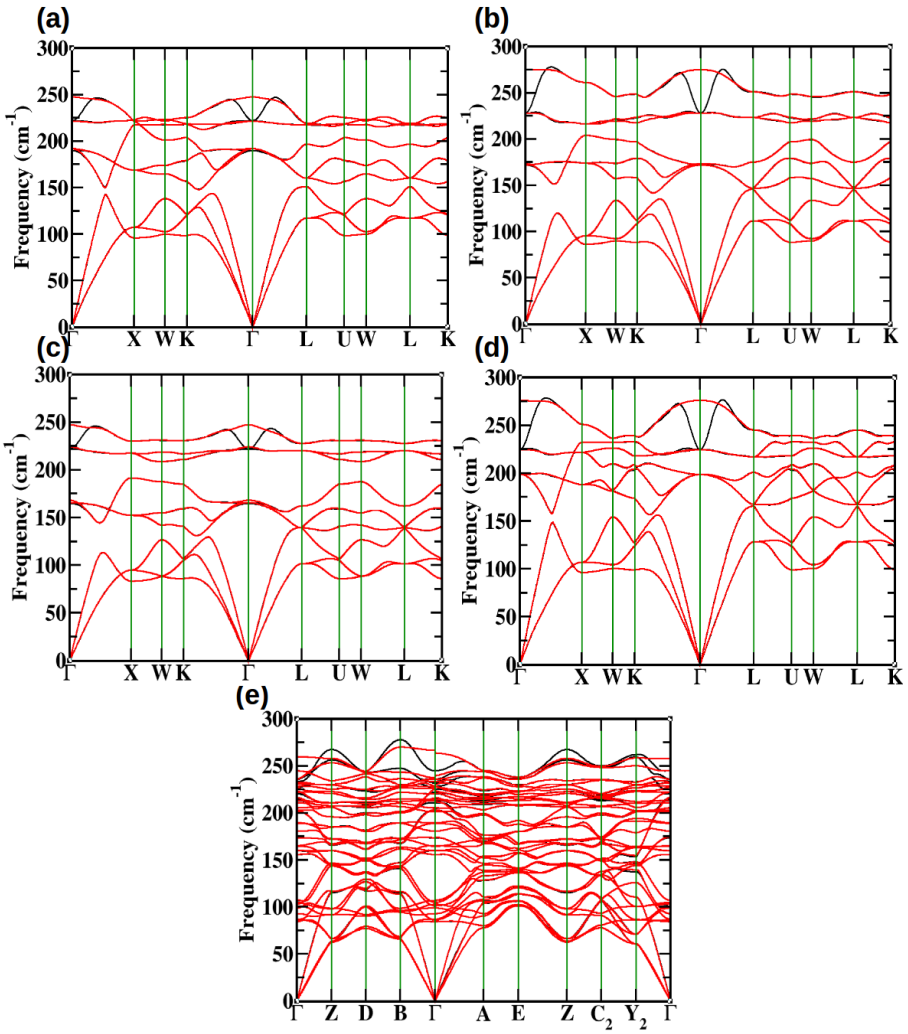

Figure A.11: comparison of phonon band structure for Lo-To splitting calculations (Black : without Lo-To splitting correction, Red: with Lo-To splitting correction) for (a) ZrNiSn (b) HfCoSb (c) HfNiSn (d) ZrCoSb (e)ZrHfCoNiSnSb

Table A.11: High frequency dielectric tensor and born effective charges (in electrons) of the parent compounds. The bracketed values are from the references [6, 7]

Properties	ZrNiSn	HfCoSb	HfNiSn	ZrCoSb
Dielectric tensor ($\epsilon^{\infty}_{xx} = \epsilon^{\infty}_{yy} = \epsilon^{\infty}_{zz}$)	21.6 [21.98]	17.7 [17.6]	20.6 [20.82]	18.6 [18.5]
$Z_x{}^*$	2.67 [2.61]	2.97 [2.96]	2.73 [2.74]	3.06 [3.10]
$Z_y{}^*$	-3.66 [-3.63]	-4.88 [-4.85]	-3.66 [-3.66]	-5.00 [-4.99]
$Z_z{}^*$	0.99 [1.02]	1.91 [1.89]	0.93 [0.92]	1.94 [1.89]

Table A.12: High frequency dielectric tensor and born effective charges (in electrons) of ZrHfCoNiSnSb

Dilectric tensor	Z^*_{Zr}	Z^*_{Hf}	Z^*_{Co}	Z^*_{Ni}	Z^*_{Sn}	Z^*_{Sb}
$\epsilon^{\infty}_{xx} = 19.78, \epsilon^{\infty}_{yy} = 19.77, \epsilon^{\infty}_{zz} = 19.54,$	2.67	2.96	-5.03	-3.55	1.31	1.64

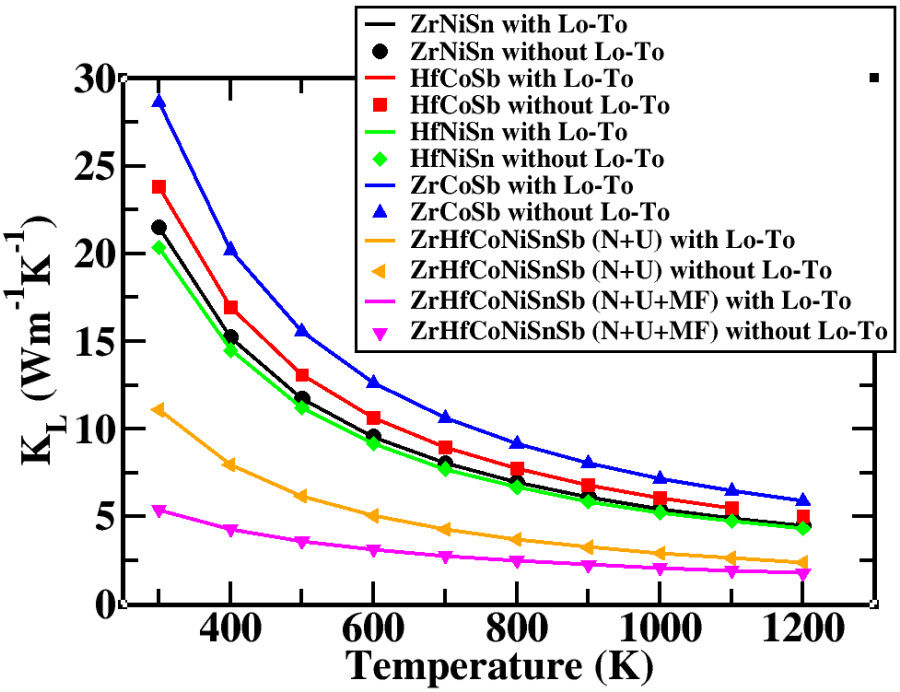

Figure A.12: Comparison of lattice thermal conductivity for different structures with and without LO-TO corrections.

A.13 Unfolding of bands and true band characteristics

The parent compounds—ZrNiSn, HfCoSb, HfNiSn, and ZrCoSb—are based on an FCC lattice with a basis and crystallize in a cubic conventional unit cell. However, their corresponding primitive unit cells adopt a rhombohedral geometry due to the nature of the FCC

lattice. To capture the true electronic structure and symmetry-resolved features, the band structures of the conventional (cubic) unit cells were unfolded onto the primitive Brillouin zone (PBZ) using the Unfold-X tool implemented in Quantum Espresso software. This approach allows for a more accurate representation of the underlying band characteristics. For completeness and comparison, the band structures of the primitive unit cells were also calculated and plotted alongside their unfolded counterparts. These comparisons are shown in Fig. A.13 for ZrNiSn and HfCoSb and Fig. A.14 for HfNiSn and ZrCoSb. The transformation between the primitive and supercell (conventional) Brillouin zones of FCC lattice is governed by the following transformation matrix M, which maps a wave vector $\vec{k}$ from the PBZ to the wave vector $\vec{K}$ supercell Brillouin zone by the relation :

$$\vec{K} = M.\vec{k} \tag{A.12}$$

where,

$$M = \begin{pmatrix} \text{-1} & 1 & \text{-1} \\ \text{-1} & 1 & 1 \\ 1 & 1 & \text{-1} \end{pmatrix} \tag{A.13}$$

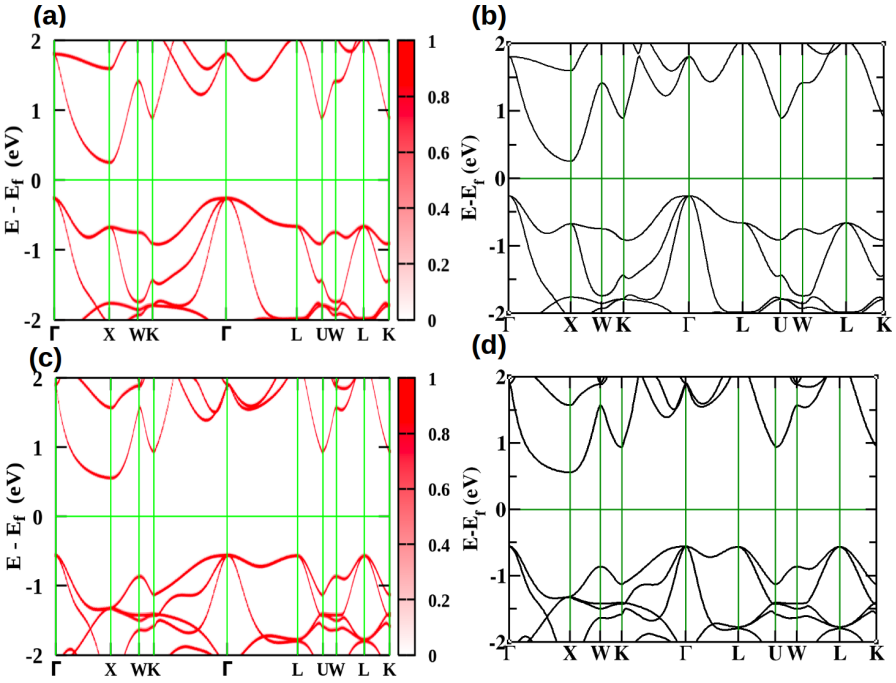

Figure A.13: (a) Unfolded band structure of ZrNiSn (b) True band structure (calculated directly from DFT) of primitive unit cell of ZrNiSn (c) Unfolded band structure of HfCoSb (d) True band structure (calculated directly from DFT) of the primitive unit cell of HfCoSb

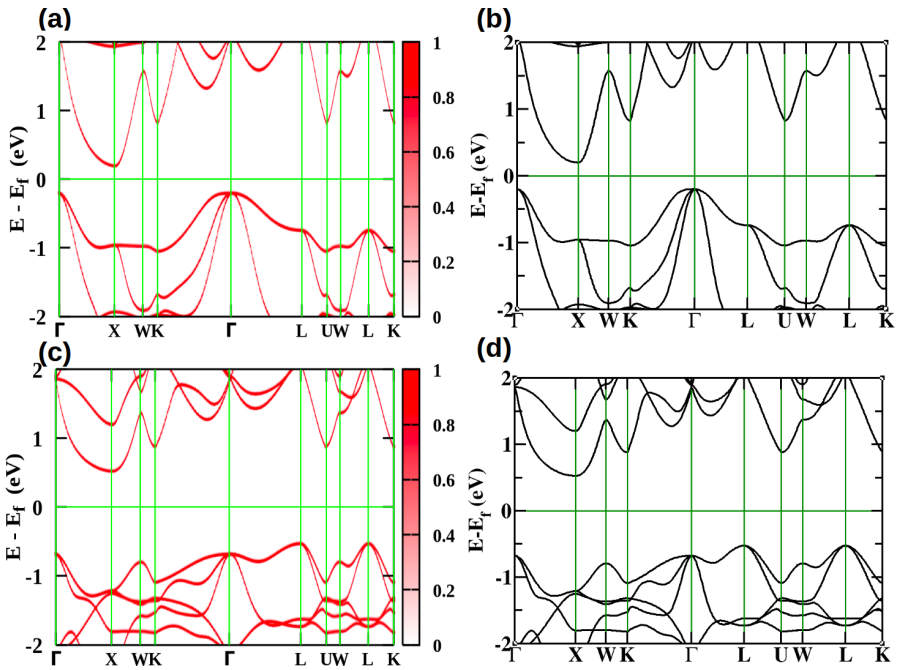

Figure A.14: (a) Unfolded band structure of HfNiSn (b) True band structure (calculated directly from DFT) of primitive unit cell of HfNiSn (c) Unfolded band structure of ZrCoSb (d) True band structure (calculated directly from DFT) of the primitive unit cell of ZrCoSb

As evident from the plots above, the key features of the original band structures are accurately reproduced in the unfolded band structures across all systems studied. In all cases, the conduction band minimum (CBM) is located at the X point of the primitive Brillouin zone of the FCC lattice. By applying the transformation matrix M, we observe that the X point in the primitive Brillouin zone maps onto the Γ point of the conventional Brillouin zone corresponding to a cubic structure. Likewise, the L point in the primitive Brillouin zone maps to the R point in the conventional Brillouin zone. This mapping implies that the CBM, initially at the X point in the primitive unit cell, appears at the Γ point in the conventional unit cell. Concerning the valence band maximum (VBM): for both ZrNiSn and HfNiSn, the VBM is located at Γ; in the case of HfCoSb, the VBM is present at both Γ and L points; and for ZrCoSb, the VBM is at the L point, with a secondary valence band edge (VBE) at Γ that lies approximately 130 meV below the VBM. Given the transformation from L in the primitive Brillouin zone to R in the conventional Brillouin zone, the same features are observed at the R point in the conventional band structures: a second VBM for HfCoSb and the true VBM for ZrCoSb. Thus, the conventional unit cell of HfCoSb exhibits an additional VBM consistent with that in the primitive unit cell, while for

ZrCoSb, the energy difference of around 130 meV between the VBM at L and the VBE at Γ is retained. Our band structure results for the primitive unit cells are in full agreement with previously reported results in the literature [6, 7]. As a result, ZrNiSn and HfNiSn, which exhibit indirect band gaps in the primitive unit cell, appear as direct band gap materials in the conventional unit cell. HfCoSb maintains a direct band gap in both representations, with an additional VBM at L (primitive) and R (conventional). ZrCoSb remains an indirect band gap material in both unit cells, with its VBM consistently located at L (primitive) or R (conventional). Furthermore, the band gap values obtained for the primitive and conventional unit cells are identical. This consistency is also supported by comparison with previously published data [6, 7]. The absence of band gap variation is expected, since in an ideal (undistorted and undoped) system, the spectral function $A(\vec{k}_i, E)$, defined below and in Reference [109], captures the projection of the supercell wavefunction $|\vec{K}m\rangle$ (from the m^{th} band of the supercell) onto the primitive cell wavefunction $|\vec{k}n\rangle$ (from the n^{th} band), provided the energies match, i.e., $E_m = E_n$. Therefore, any energy window devoid of eigenstates in the supercell will likewise lack eigenstates in the primitive cell. The spectral function is defined as:

$$A(\vec{k}_i, E) = \sum_m P_{\vec{K}m}(\vec{k}_i)\delta(E_m \text{ - } E) \tag{A.14}$$

where,

$$P_{\vec{K}m}(\vec{k}_i) = \sum_n |\langle \vec{K}m|\vec{k}_i n\rangle|^2 \tag{A.15}$$

For the high entropy alloy (HEA) ZrHfCoNiSnSb, 50% substitution has been performed at each atomic site, resulting in a structure that deviates from the conventional cubic unit cell of FCC primitive unit cell. When structural optimization is carried out under the constraint of maintaining cubic symmetry, the system fails to converge to a stable configuration. However, when the symmetry constraint is lifted, the structure relaxes into a slightly distorted monoclinic phase. Since there is no corresponding FCC primitive unit cell for this relaxed structure—and even tools like Seek-path identify the monoclinic cell as the smallest repeating unit—there is no meaningful lower-symmetry reference cell to which the band structure can be unfolded. As a result, band unfolding for this HEA system is not feasible.

Table A.13: Comparison of the bandgap of the parent compounds

Bandgap	ZrNiSn	HfNiSn	ZrCoSb	HfCoSb
Bandgap of the conventional unit cell (eV)	0.51	0.40	1.05	1.12
Bandgap of the primitive unit cell (eV)	0.51	0.40	1.05	1.12
Reported values (Theoretical) (eV) [6, 7]	0.49	0.36	1.06	1.13
Reported values (experimental) (eV) [93, 128]	0.19	0.22	0.14	0.07

Appendix B

Supplementary Information for Chapter 4

B.1 Effective masses of different bands

B.1.1 Effective masses of different bands of OS1

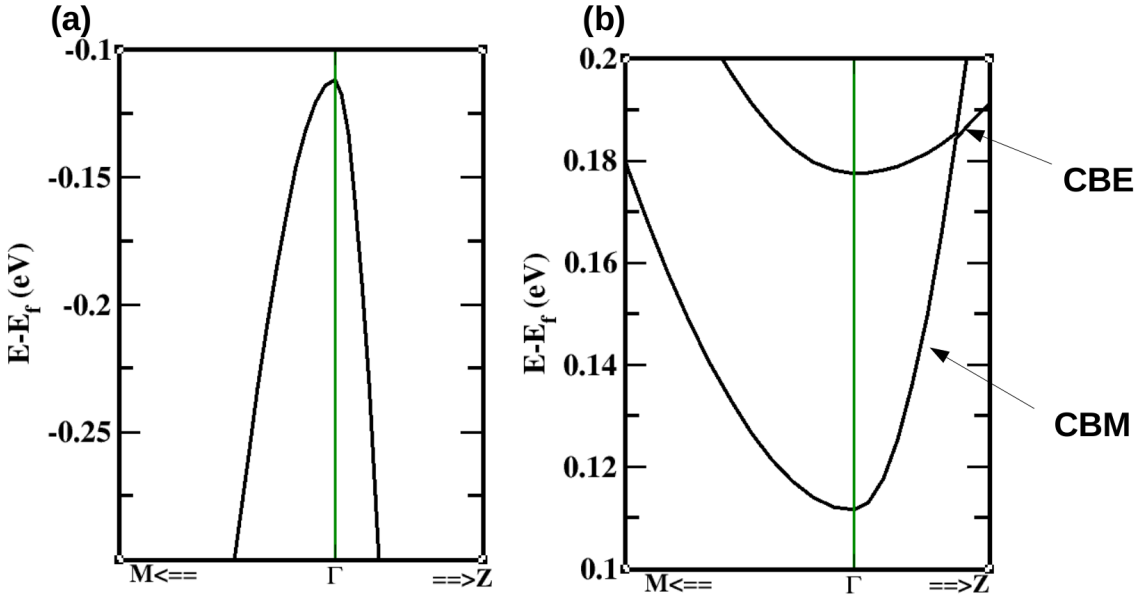

Figure B.1: (a) VBM of OS1 of Nb_2Co_2InSb (Nb_2Co_2GaSb) (b) CBM/CBE of OS1 of Nb_2Co_2InSb (Nb_2Co_2GaSb)

Table B.1: Dos and conductive effective masses of Valence band (VBM/VBE) of OS1 of Nb_2Co_2InSb (Nb_2Co_2GaSb). $\Delta E$is difference in energy between VBE and VBM

Band	m_D^*	m_σ^*	ΔE (eV)
VBM	0.23 (0.32)	0.17 (0.20)	0 (0)

Table B.2: Dos and conductive effective masses of conduction band (CBM/CBE) of OS1 of Nb_2Co_2InSb (Nb_2Co_2GaSb). $\Delta E$is difference in energy between CBE and CBM

Band	m_D^*	m_σ^*	ΔE (eV)
CBM	0.81 (0.34)	0.59 (0.33)	0 (0)
CBE	1.79 (0.39)	1.73 (0.29)	0.063 (0.13)

B.1.2 Effective masses of different bands of OS2

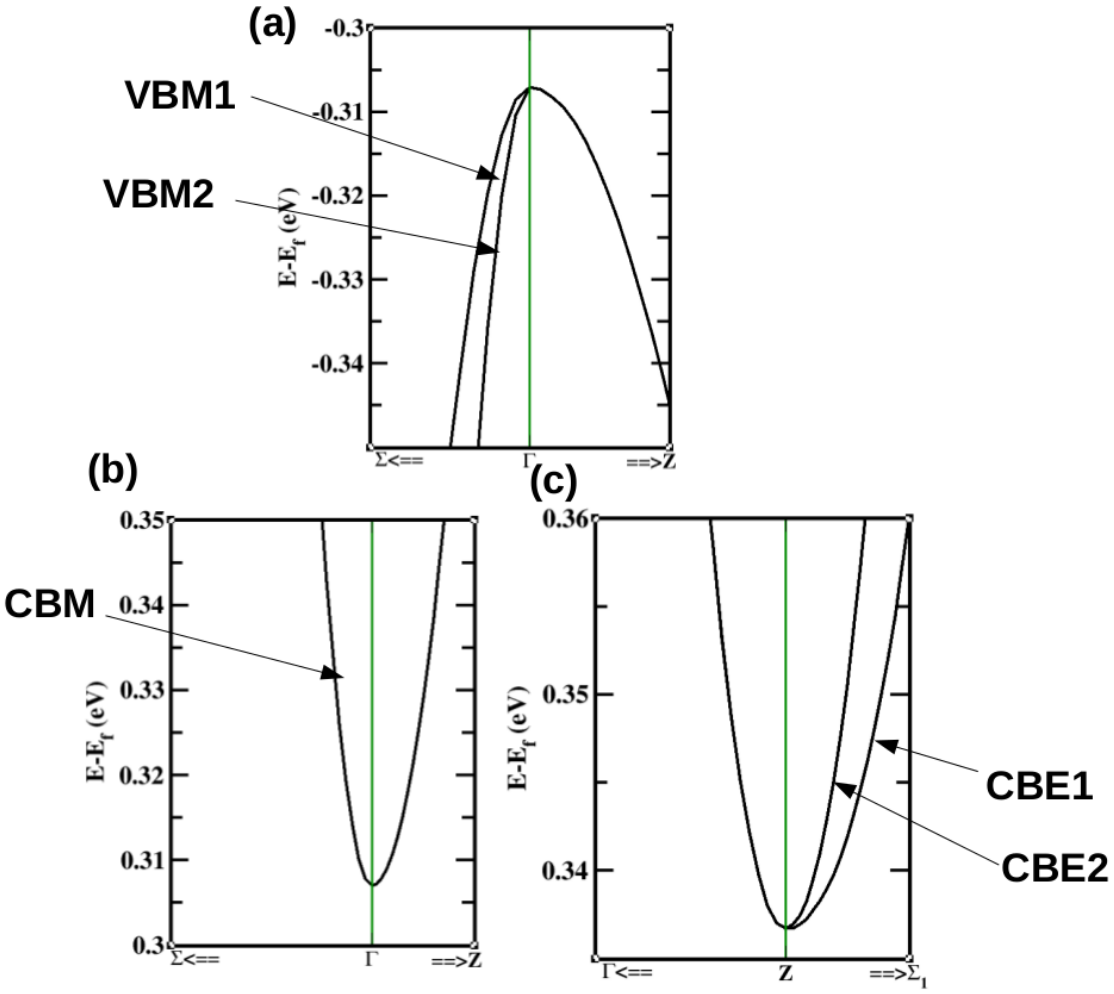

Figure B.2: (a) VBM of OS2 of Nb_2Co_2InSb (Nb_2Co_2GaSb) (b) CBM of OS2 of Nb_2Co_2InSb (Nb_2Co_2GaSb) (c) CBE of OS2 of Nb_2Co_2InSb (Nb_2Co_2GaSb)

Table B.3: Dos and conductive effective masses of Valence band (VBM/VBE) of OS2 of Nb_2Co_2InSb (Nb_2Co_2GaSb) . $\Delta E$is difference in energy between VBE and VBM

Band	m_D^*	m_σ^*	ΔE (eV)
VBM1	0.75 (0.85)	0.66 (0.78)	0 (0)
VBM2	0.44 (0.54)	0.31 (0.43)	0 (0)

Table B.4: Dos and conductive effective masses of conduction band (CBM/CBE) of OS2 of Nb_2Co_2InSb (Nb_2Co_2GaSb). $\Delta E$is difference in energy between CBE and CBM

Band	m_D^*	m_σ^*	ΔE (eV)
CBM	1.10 (0.38)	1.03 (0.28)	0 (0)
CBE1	4.07 (1.11)	2.22 (0.54)	0.027 (0.028)
CBE2	2.14 (0.35)	1.34 (0.22)	0.027 (0.039)

B.1.3 Effective masses of different bands of SQS1

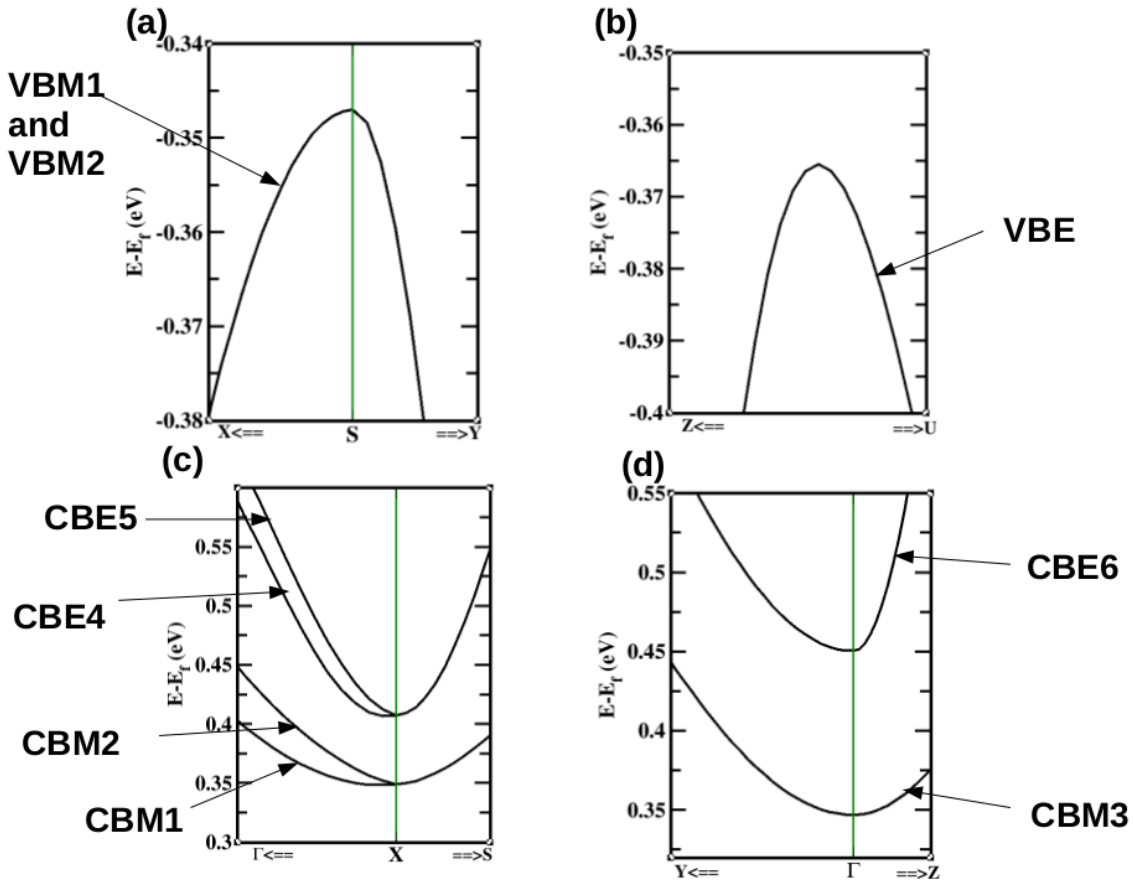

Figure B.3: (a) VBM of SQS1 of Nb_2Co_2InSb (Nb_2Co_2GaSb) (b) VBE of SQS1 of Nb_2Co_2InSb (Nb_2Co_2GaSb) (c) CBM/CBE of SQS1 of Nb_2Co_2InSb (Nb_2Co_2GaSb) (d) CBM/CBE of SQS1 of Nb_2Co_2InSb (Nb_2Co_2GaSb)

Table B.5: Dos and conductive effective masses of Valence band (VBM/VBE) of SQS1 of Nb_2Co_2InSb (Nb_2Co_2GaSb) . $\Delta E$is difference in energy between VBE and VBM

Band	m_D^*	m_σ^*	ΔE (eV)
VBM1	2.64 (2.30)	0.89 (0.80)	0 (0)
VBM2	2.65 (2.31)	0.89 (0.80)	0 (0)
VBE	1.83 (1.71)	0.69 (0.67)	0.018 (0.06)

Table B.6: Dos and conductive effective masses of conduction band (CBM/CBE) of SQS1 of Nb_2Co_2InSb (Nb_2Co_2GaSb). $\Delta E$is difference in energy between CBE and CBM

Band	m_D^*	m_σ^*	ΔE (eV)
CBM1	1.67 (0.52)	1.01 (0.31)	0.001 (0)
CBM2	1.51 (0.50)	0.93 (0.30)	0.002 (0)
CBM3	1.46 (1.60)	1.43 (0.94)	0 (0.053)
CBE4	0.59 (1.33)	0.36 (0.82)	0.06 (0.055)
CBE5	0.57 (1.57)	0.35 (1.54)	0.061 (0.055)
CBE6	0.40 (0.38)	0.29 (0.29)	0.103 (0.055)

B.1.4 Effective masses of different bands of SQS2

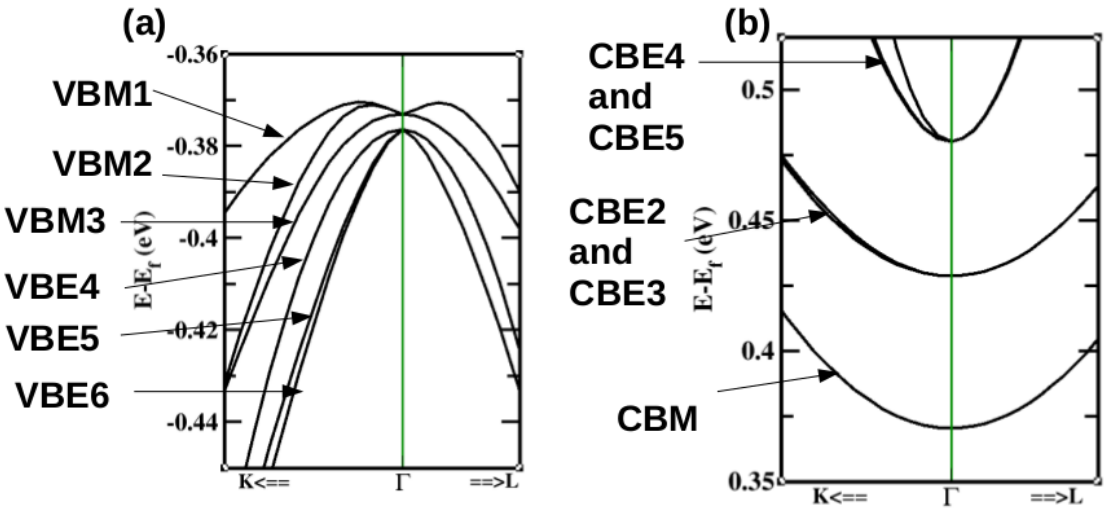

Figure B.4: (a) VBM/VBE of SQS2 of Nb_2Co_2InSb (b) CBM/CBE of SQS2 of Nb_2Co_2InSb

Table B.7: Dos and conductive effective masses of Valence band (VBM/VBE) of SQS2 Nb_2Co_2InSb. $\Delta E$is difference in energy between VBE and VBM

Band	m_D^*	m_σ^*	ΔE (eV)
VBM1	0.65	0.65	0
VBM2	0.65	0.65	0
VBM3	3.20	3.20	0
VBE4	2.88	2.88	0.005
VBE5	0.21	0.21	0.005
VBE6	0.20	0.20	0.005

Table B.8: Dos and conductive effective masses of conduction band (CBM/CBE) of SQS2 of Nb_2Co_2InSb . $\Delta E$is difference in energy between CBE and CBM

Band	m_D^*	m_σ^*	ΔE (eV)
CBM	0.88	0.61	0
CBE2	1.72	1.72	0.058
CBE3	1.45	1.45	0.058
CBE4	1.53	1.53	0.110
CBE5	0.22	0.22	0.110

B.2 Phonon dispersion relation of SQS2 of Nb_2Co_2GaSb

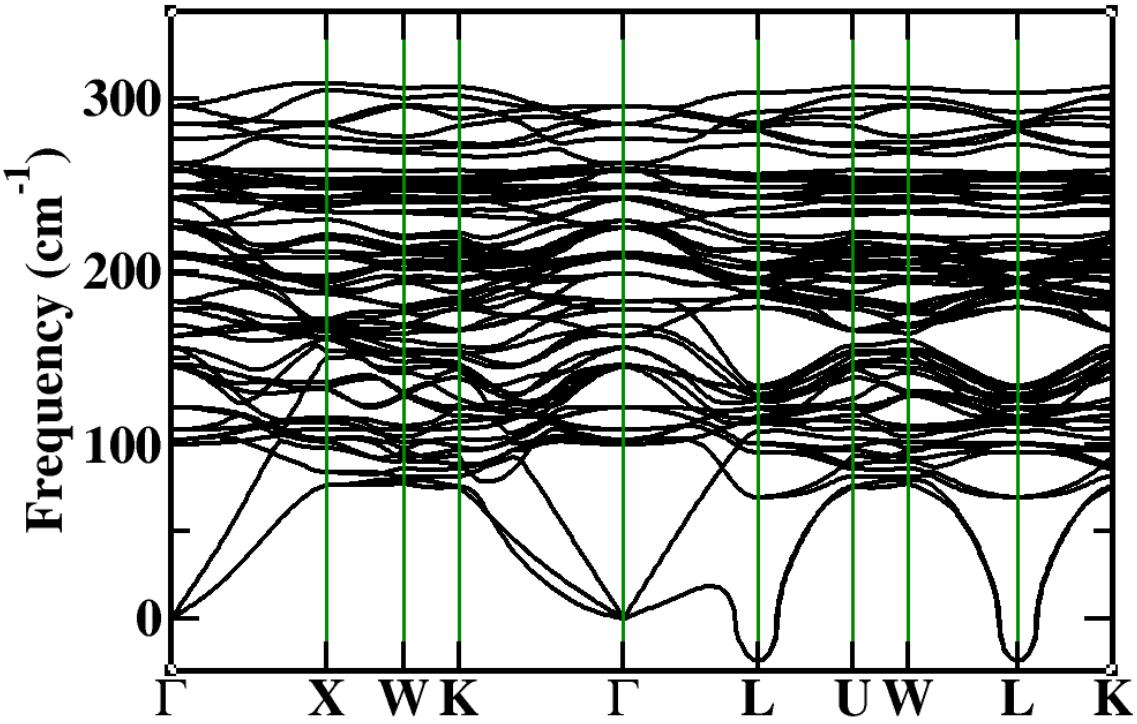

Figure B.5: Phonon dispersion curve of the SQS2 of Nb_2Co_2GaSb

Bibliography

[1] H Julian Goldsmid et al., *Introduction to thermoelectricity* volume 121, Springer (2010). v, 3, 4

[2] Rajeev Ranjan, "Entropy-stabilized zrhfconisnsb half-heusler alloy for thermoelectric applications: a theoretical prediction", *Phys. Chem. Chem. Phys.* **27**, pp. 15622–15634 (2025). vi, 51

[3] G Jeffrey Snyder and Eric S Toberer, "Complex thermoelectric materials", *Nature materials* **7**(2), pp. 105–114 (2008). xiv, 1, 3, 7, 12

[4] Mike C Payne, Michael P Teter, Douglas C Allan, TA Arias, and ad JD Joannopoulos, "Iterative minimization techniques for ab initio total-energy calculations: molecular dynamics and conjugate gradients", *Reviews of modern physics* **64**(4), pp. 1045 (1992). xiv, 30

[5] Bhawna Sahni and Aftab Alam, "Double half-heusler alloys x _2 ni _2 insb (x= zr/hf) with promising thermoelectric performance: Role of varying structural phases", *arXiv preprint arXiv:2301.00598* (2023). xviii, 65

[6] Appala Naidu Gandi and Udo Schwingenschlögl, "Electron dominated thermoelectric response in mnisn (m: Ti, zr, hf) half-heusler alloys", *Physical Chemistry Chemical Physics* **18**(20), pp. 14017–14022 (2016). xix, 9, 51, 53, 61, 66, 67, 75, 123, 127, 128

[7] Appala Naidu Gandi and Udo Schwingenschlögl, *physica status solidi (b)* **254**(11), pp. 1700419 (2017). xix, 51, 61, 66, 67, 103, 123, 127, 128

[8] Oersted, "Notiz von neuen electrisch-magnetischen versuchen des herrn seebeck in berlin", *Annalen der Physik* **73**(4), pp. 430–432 (1823). 1

[9] P JCA, “Nouvelle experiences sur la caloricité des courants électriques”, In *Annales de chimie et physique* volume 42 , pp. 371–387 (1834). 2

[10] William Thomson, “4. on a mechanical theory of thermo-electric currents”, *Proceedings of the Royal society of Edinburgh* **3**, pp. 91–98 (1857). 2

[11] M Cutler, JF Leavy, and RL Fitzpatrick, “Electronic transport in semimetallic cerium sulfide”, *Physical Review* **133**(4A), pp. A1143 (1964). 6

[12] GV Chester and A Thellung, “The law of wiedemann and franz”, *Proceedings of the Physical Society* **77**(5), pp. 1005 (1961). 6

[13] Marta Rull-Bravo, Alberto Moure, JF Fernández, and Marisol Martín-González, “Skutterudites as thermoelectric materials: revisited”, *Rsc Advances* **5**(52), pp. 41653–41667 (2015). 7, 8

[14] DT Morelli, T Caillat, J-P Fleurial, A Borshchevsky, J Vandersande, B Chen, and C Uher, “Low-temperature transport properties of p-type cosb 3”, *Physical Review B* **51**(15), pp. 9622 (1995). 8

[15] L Bertini, K Biliquist, M Christensen, C Gatti, L Holmgren, B Iversen, E Mueller, M Muhammed, G Noriega, A Palmqvist, et al., “Grain size dependence of transport properties of nano-engineered thermoelectric cosb/sub 3”, In *Proceedings ICT’03. 22nd International Conference on Thermoelectrics (IEEE Cat. No. 03TH8726)* , pp. 93–96. IEEE (2003). 8

[16] J Yang, W Zhang, SQ Bai, Z Mei, and LD Chen, “Dual-frequency resonant phonon scattering in baxryco4sb12 (r= la, ce, and sr)”, *Applied Physics Letters* **90**(19) (2007). 8

[17] YZ Pei, SQ Bai, XY Zhao, W Zhang, and LD Chen, “Thermoelectric properties of euyco4sb12 filled skutterudites”, *Solid state sciences* **10**(10), pp. 1422–1428 (2008). 8

[18] YZ Pei, Jiong Yang, LD Chen, W Zhang, JR Salvador, and Jihui Yang, “Improving thermoelectric performance of caged compounds through light-element filling”, *Applied physics letters* **95**(4) (2009). 8

[19] YZ Pei, LD Chen, W Zhang, X Shi, SQ Bai, XY Zhao, ZG Mei, and XY Li, "Synthesis and thermoelectric properties of kyco4sb12", *Applied Physics Letters* **89**(22) (2006). 8

[20] Jianjun Zhang, Bo Xu, Li-Min Wang, Dongli Yu, Jianqing Yang, Fengrong Yu, Zhongyuan Liu, Julong He, Bin Wen, and Yongjun Tian, "High-pressure synthesis of phonon-glass electron-crystal featured thermoelectric lixco4sb12", *Acta materialia* **60**(3), pp. 1246–1251 (2012). 8

[21] LD Chen, T Kawahara, XF Tang, Takashi Goto, Toshio Hirai, Jeffrey S Dyck, Wei Chen, and Ctirad Uher, "Anomalous barium filling fraction and n-type thermoelectric performance of ba y co 4 sb 12", *Journal of Applied Physics* **90**(4), pp. 1864–1868 (2001). 8

[22] M Puyet, Bertrand Lenoir, A Dauscher, M Dehmas, C Stiewe, and E Müller, "High temperature transport properties of partially filled ca x co 4 sb 12 skutterudites", *Journal of applied physics* **95**(9), pp. 4852–4855 (2004). 8

[23] XY Zhao, X Shi, LD Chen, WQ Zhang, SQ Bai, YZ Pei, XY Li, and T Goto, "Synthesis of ybyco4sb12/ yb2o3 composites and their thermoelectric properties", *Applied physics letters* **89**(9) (2006). 8

[24] Aaron D LaLonde, Yanzhong Pei, and G Jeffrey Snyder, "Reevaluation of pbte 1- x i x as high performance n-type thermoelectric material", *Energy & Environmental Science* **4**(6), pp. 2090–2096 (2011). 8, 9

[25] Yanzhong Pei, Aaron LaLonde, Shiho Iwanaga, and G Jeffrey Snyder, "High thermoelectric figure of merit in heavy hole dominated pbte", *Energy & Environmental Science* **4**(6), pp. 2085–2089 (2011). 8

[26] Kanishka Biswas, Jiaqing He, Ivan D Blum, Chun-I Wu, Timothy P Hogan, David N Seidman, Vinayak P Dravid, and Mercouri G Kanatzidis, "High-performance bulk thermoelectrics with all-scale hierarchical architectures", *Nature* **489**(7416), pp. 414–418 (2012). 8

[27] Anita Bugalia, Vivek Gupta, and Nagesh Thakur, "Strategies to enhance the performance of thermoelectric materials: A review", *Journal of Renewable and Sustainable Energy* **15**(3) (2023). 8

[28] Manasa R Shankar and AN Prabhu, "A review on structural characteristics and thermoelectric properties of mid-temperature range chalcogenide-based thermoelectric materials", *Journal of Materials Science* **58**(43), pp. 16591–16633 (2023). 8

[29] Juan Cui, Meimei Wang, Xiao Xu, Yue Chen, and Jiaqing He, "Understanding the effects of iodine doping on the thermoelectric performance of n-type pbte ingot materials", *Journal of Applied Physics* **126**(2) (2019). 9

[30] Wei Wang, Cong Xian, Yun Ou, Zhijian He, and Shuhong Xie, "Thermoelectric properties of pbs doped with bi2s3 and cu2s prepared by hydrothermal synthesis and spark plasma sintering", *Crystals* **13**(5), pp. 764 (2023). 9

[31] Chenguang Fu, Tiejun Zhu, Yintu Liu, Hanhui Xie, and Xinbing Zhao, "Band engineering of high performance p-type fenbsb based half-heusler thermoelectric materials for figure of merit zt¿ 1", *Energy & Environmental Science* **8**(1), pp. 216–220 (2015). 9

[32] Hangtian Zhu, Jun Mao, Yuwei Li, Jifeng Sun, Yumei Wang, Qing Zhu, Guannan Li, Qichen Song, Jiawei Zhou, Yuhao Fu, et al., "Discovery of tafesb-based half-heuslers with high thermoelectric performance", *Nature Communications* **10**(1), pp. 270 (2019). 9, 75

[33] Kaiyang Xia, Yintu Liu, Shashwat Anand, G Jeffrey Snyder, Jiazhan Xin, Junjie Yu, Xinbing Zhao, and Tiejun Zhu, "Enhanced thermoelectric performance in 18-electron nb0. 8cosb half-heusler compound with intrinsic nb vacancies", *Advanced Functional Materials* **28**(9), pp. 1705845 (2018). 9

[34] Shashwat Anand, Max Birchwood Wood, Yi Xia, Chris Wolverton, and G.J̃effrey Snyder, "Double half-heuslers", *Joule* **3**(5), pp. 1226–1238 (2019). 9

[35] Kan Chen, Ruizhi Zhang, Jan-Willem G Bos, and Michael J Reece, "Synthesis and thermoelectric properties of high-entropy half-heusler mfe1- xcoxsb (m= equimolar ti, zr, hf, v, nb, ta)", *Journal of Alloys and Compounds* **892**, pp. 162045 (2022). 10, 52, 57

[36] Wenjie Li, Subrata Ghosh, Na Liu, and Bed Poudel, "Half-heusler thermoelectrics: Advances from materials fundamental to device engineering", *Joule* **8**(5), pp. 1274–1311 (2024). 10, 11

[37] M N Touzelbaev, P Zhou, R Venkatasubramanian, and KE Goodson, "Thermal characterization of bi 2 te 3/sb 2 te 3 superlattices", *Journal of Applied Physics* **90**(2), pp. 763–767 (2001). 12

[38] J C Caylor, K Coonley, J Stuart, T Colpitts, and R Venkatasubramanian, "Enhanced thermoelectric performance in pbte-based superlattice structures from reduction of lattice thermal conductivity", *Applied physics letters* **87**(2) (2005). 12

[39] H Beyer, J Nurnus, H Böttner, A Lambrecht, E Wagner, and G Bauer, "High thermoelectric figure of merit zt in pbte and bi2te3-based superlattices by a reduction of the thermal conductivity", *Physica E: Low-dimensional Systems and Nanostructures* **13**(2-4), pp. 965–968 (2002). 12

[40] Erwin Schrödinger, "Quantisierung als eigenwertproblem", *Annalen der physik* **386**(18), pp. 109–139 (1926). 15

[41] Max Born and J Franck, "Quantentheorie und molekelbildung", *Zeitschrift für Physik* **31**(1), pp. 411–429 (1925). 16

[42] M. Born and R. Oppenheimer, "Zur quantentheorie der molekeln", *Annalen der Physik* **389**(20), pp. 457–484 (1927). 16

[43] Richard M Martin, *Electronic structure: basic theory and practical methods*, Cambridge university press (2020). 19, 22, 26

[44] N David Mermin, "Thermal properties of the inhomogeneous electron gas", *Physical Review* **137**(5A), pp. A1441 (1965). 19, 21

[45] Pierre Hohenberg and Walter Kohn, "Inhomogeneous electron gas", *Physical review* **136**(3B), pp. B864 (1964). 20

[46] Walter Kohn and Lu Jeu Sham, "Self-consistent equations including exchange and correlation effects", *Physical review* **140**(4A), pp. A1133 (1965). 20, 21, 22

[47] Robert G Parr, "Density functional theory of atoms and molecules", In *Horizons of Quantum Chemistry: Proceedings of the Third International Congress of Quantum Chemistry Held at Kyoto, Japan, October 29-November 3, 1979* , pp. 5–15. Springer (1989). 25

[48] Christopher J Cramer, FM Bickelhaupt, et al., "Essentials of computational chemistry", *ANGEWANDTE CHEMIE-INTERNATIONAL EDITION IN ENGLISH-* **42**(4), pp. 381–381 (2003). 25

[49] John P Perdew and Alex Zunger, "Self-interaction correction to density-functional approximations for many-electron systems", *Physical review B* **23**(10), pp. 5048 (1981). 26

[50] John P Perdew, Kieron Burke, and Matthias Ernzerhof, "Generalized gradient approximation made simple", *Physical review letters* **77**(18), pp. 3865 (1996). 26, 53, 78

[51] Matthias Ernzerhof and Gustavo E Scuseria, "Assessment of the perdew–burke–ernzerhof exchange-correlation functional", *The Journal of chemical physics* **110**(11), pp. 5029–5036 (1999). 26

[52] Richard M. Martin, *Electronic Structure: Basic Theory and Practical Methods*, Cambridge University Press Cambridge (2004). 28, 31

[53] Hendrik J Monkhorst and James D Pack, "Special points for brillouin-zone integrations", *Physical review B* **13**(12), pp. 5188 (1976). 29

[54] Neil W. Ashcroft and N. David Mermin, *Solid State Physics*, Holt, Rinehart and Winston New York (1976). 29, 37, 47

[55] DR Hamann, M Schlüter, and C Chiang, "Norm-conserving pseudopotentials", *Physical review letters* **43**(20), pp. 1494 (1979). 30

[56] David Vanderbilt, "Soft self-consistent pseudopotentials in a generalized eigenvalue formalism", *Physical review B* **41**(11), pp. 7892 (1990). 30

[57] Hans Hellmann, *Einführung in die Quantenchemie*, Deuticke Leipzig (1937). 31

[58] R. P. Feynman, "Forces in molecules", *Physical Review* **56**(4), pp. 340–343 (1939). 31

[59] OH Nielsen and Richard M Martin, "Quantum-mechanical theory of stress and force", *Physical Review B* **32**(6), pp. 3780 (1985). 31

[60] Richard M Martin, "Relation between elastic tensors of wurtzite and zinc-blende structure materials", *Physical Review B* **6**(12), pp. 4546 (1972). 31

[61] Max Born, *Atomic Physics*, Blackie & Son Limited London 7th edition (1954). 33

[62] P. Hohenberg and W. Kohn, "Inhomogeneous electron gas", *Physical Review* **136**(3B), pp. B864–B871 (1964). 33

[63] W. Kohn and L. J. Sham, "Self-consistent equations including exchange and correlation effects", *Physical Review* **140**(4A), pp. A1133–A1138 (1965). 33

[64] Stefano Baroni, Stefano De Gironcoli, Andrea Dal Corso, and Paolo Giannozzi, "Phonons and related crystal properties from density-functional perturbation theory", *Reviews of modern Physics* **73**(2), pp. 515 (2001). 33, 34, 35, 53, 78

[65] Xavier Gonze, "First-principles responses of solids to atomic displacements and homogeneous electric fields: Implementation of a conjugate-gradient algorithm", *Physical Review B* **55**(16), pp. 10337–10354 (1997). 33

[66] John M Ziman, *Electrons and phonons: the theory of transport phenomena in solids*, Oxford university press (2001). 36, 42

[67] Georg KH Madsen and David J Singh, "Boltztrap. a code for calculating band-structure dependent quantities", *Computer Physics Communications* **175**(1), pp. 67–71 (2006). 38, 111

[68] Georg KH Madsen, Jesús Carrete, and Matthieu J Verstraete, "Boltztrap2, a program for interpolating band structures and calculating semi-classical transport coefficients", *Computer Physics Communications* **231**, pp. 140–145 (2018). 38, 54, 78

[69] Zhigang Shuai, Linjun Wang, and Chenchen Song, *Theory of charge transport in carbon electronic materials*, Springer Science & Business Media (2012). 39, 40

[70] Mark Lundstrom, "Fundamentals of carrier transport, 2nd edn", *Measurement Science and Technology* **13**(2), pp. 230–230 (2002). 39

[71] Jian Liu, Qiao-Yu Jiang, Shi-Da Zhang, and Heng Zhang, "Carrier mobility and relaxation time in bicuseo", *Physics Letters A* **383**(34), pp. 125990 (2019). 41, 42

[72] Wu Li, Jesús Carrete, Nebil A Katcho, and Natalio Mingo, "Shengbte: A solver of the boltzmann transport equation for phonons", *Computer Physics Communications* **185**(6), pp. 1747–1758 (2014). 42

[73] Rudolf Ernst Peierls, *Zur kinetischen theorie der wärmeleitung in kristallen*, JA Barth (1929). 42

[74] DA Broido, A Ward, and N Mingo, "Lattice thermal conductivity of silicon from empirical interatomic potentials", *Physical Review B—Condensed Matter and Materials Physics* **72**(1), pp. 014308 (2005). 43

[75] Aleksandr Chernatynskiy and Simon R Phillpot, "Evaluation of computational techniques for solving the boltzmann transport equation for lattice thermal conductivity calculations", *Physical Review B—Condensed Matter and Materials Physics* **82**(13), pp. 134301 (2010). 43, 44

[76] Jinlong Ma, Wu Li, and Xiaobing Luo, "Examining the callaway model for lattice thermal conductivity", *Physical Review B* **90**(3), pp. 035203 (2014). 43, 44, 46

[77] Philip B Allen, "Improved callaway model for lattice thermal conductivity", *Physical Review B—Condensed Matter and Materials Physics* **88**(14), pp. 144302 (2013). 44, 45

[78] Joseph Callaway, "Model for lattice thermal conductivity at low temperatures", *Physical Review* **113**(4), pp. 1046 (1959). 45

[79] Yongsheng Zhang, Eric Skoug, Jeffrey Cain, Vidvuds Ozoliņš, Donald Morelli, and Christopher Wolverton, "First-principles description of anomalously low lattice thermal conductivity in thermoelectric cu-sb-se ternary semiconductors", *Physical Review B—Condensed Matter and Materials Physics* **85**(5), pp. 054306 (2012). 47, 64, 88

[80] DT Morelli, JP Heremans, and GA Slack, "Semiconductors ii: Surfaces, interfaces, microstructures, and related topics-estimation of the isotope effect on the lattice thermal conductivity of group iv and group iii-v semiconductors", *Physical Review-Section B-Condensed Matter* **66**(19), pp. 195304–195304 (2002). 47

[81] M Asen-Palmer, K Bartkowski, E Gmelin, M Cardona, AP Zhernov, AV Inyushkin, A Taldenkov, VI Ozhogin, Kohei M Itoh, and EE Haller, "Thermal conductivity of

germanium crystals with different isotopic compositions", *Physical review B* **56**(15), pp. 9431 (1997). 47, 64, 88

[82] Yongsheng Zhang, "First-principles debye–callaway approach to lattice thermal conductivity", *Journal of Materiomics* **2**(3), pp. 237–247 (2016). 47

[83] Tao Fan and Artem R Oganov, "Aicon: A program for calculating thermal conductivity quickly and accurately", *Computer Physics Communications* **251**, pp. 107074 (2020). 47, 48, 65

[84] PG Klemens, "Thermal resistance due to point defects at high temperatures", *Physical review* **119**(2), pp. 507 (1960). 48

[85] CL Wan, W Pan, Q Xu, YX Qin, JD Wang, ZX Qu, and MH Fang, "Effect of point defects on the thermal transport properties of (la x gd 1- x) 2 zr 2 o 7: Experiment and theoretical model", *Physical Review B—Condensed Matter and Materials Physics* **74**(14), pp. 144109 (2006). 48

[86] C Hu, K Xia, X Chen, X Zhao, and T Zhu, "Transport mechanisms and property optimization of p-type (zr, hf) cosb half-heusler thermoelectric materials", *Materials Today Physics* **7**, pp. 69–76 (2018). 48

[87] Alex Petersen, S Bhattacharya, TM Tritt, and SJ Poon, "Critical analysis of lattice thermal conductivity of half-heusler alloys using variations of callaway model", *Journal of Applied Physics* **117**(3) (2015). 48, 65

[88] A Van de Walle, P Tiwary, M De Jong, DL Olmsted, M Asta, A Dick, D Shin, Yi Wang, L-Q Chen, and Z-K Liu, *Calphad* **42**, pp. 13–18 (2013). 49, 50, 54

[89] Axel Van De Walle, "Multicomponent multisublattice alloys, nonconfigurational entropy and other additions to the alloy theoretic automated toolkit", *Calphad* **33**(2), pp. 266–278 (2009). 49

[90] Wolfgang G Zeier, Jennifer Schmitt, Geoffroy Hautier, Umut Aydemir, Zachary M Gibbs, Claudia Felser, and G Jeffrey Snyder, "Engineering half-heusler thermoelectric materials using zintl chemistry", *Nature Reviews Materials* **1**(6), pp. 1–10 (2016). 51, 76

[91] Hiroaki Muta, Takanori Kanemitsu, Ken Kurosaki, and Shinsuke Yamanaka, *Journal of Alloys and Compounds* **469**(1-2), pp. 50–55 (2009). 51

[92] DF Zou, SH Xie, YY Liu, JG Lin, and JY Li, "Electronic structure and thermoelectric properties of half-heusler zr0. 5hf0. 5nisn by first-principles calculations", *Journal of Applied Physics* **113**(19) (2013). 51, 75

[93] Takeyuki Sekimoto, Ken Kurosaki, Hiroaki Muta, and S Yamasaka, In *ICT 2005. 24th International Conference on Thermoelectrics, 2005.* , pp. 347–350. IEEE (2005). 51, 53, 94, 128

[94] Ruiheng Liu, Hongyi Chen, Kunpeng Zhao, Yuting Qin, Binbin Jiang, Tiansong Zhang, Gang Sha, Xun Shi, Ctirad Uher, Wenqing Zhang, et al., "Entropy as a gene-like performance indicator promoting thermoelectric materials", *Advanced Materials* **29**(38), pp. 1702712 (2017). 52

[95] Rui-Zhi Zhang, Francesco Gucci, Hongyu Zhu, Kan Chen, and Michael J Reece, "Data-driven design of ecofriendly thermoelectric high-entropy sulfides", *Inorganic chemistry* **57**(20), pp. 13027–13033 (2018). 52

[96] Sicong Jiang, Tao Hu, Joshua Gild, Naixie Zhou, Jiuyuan Nie, Mingde Qin, Tyler Harrington, Kenneth Vecchio, and Jian Luo, "A new class of high-entropy perovskite oxides", *Scripta Materialia* **142**, pp. 116–120 (2018). 52

[97] Christina M Rost, Edward Sachet, Trent Borman, Ali Moballegh, Elizabeth C Dickey, Dong Hou, Jacob L Jones, Stefano Curtarolo, and Jon-Paul Maria, "Entropy-stabilized oxides", *Nature communications* **6**(1), pp. 8485 (2015). 52

[98] Rui-Zhi Zhang and Michael J Reece, "Review of high entropy ceramics: design, synthesis, structure and properties", *Journal of Materials Chemistry A* **7**(39), pp. 22148–22162 (2019). 52, 57

[99] Chalchisa Getachew Adamo, Ashutosh Srivastava, Surafel Shiferaw Legese, Yoshihito Kawamura, Ayansa Tolesa Serbesa, Sreeram Punathil Raman, Femi Emmanuel Olu, Chandra Sekhar Tiwary, Abhishek Kumar Singh, and Kamanio Chattopadhyay, "Thermoelectric transport of a novel zr-based half-heusler high-entropy alloy", *Energy Technology* **12**(2), pp. 2301119 (2024). 52

[100] Anirudha Karati, M Nagini, Sanyukta Ghosh, Rajashekhara Shabadi, KG Pradeep, Ramesh Chandra Mallik, BS Murty, and UV Varadaraju, *Scientific reports* **9**(1), pp. 5331 (2019). 52

[101] Paolo Giannozzi, Stefano Baroni, Nicola Bonini, Matteo Calandra, Roberto Car, Carlo Cavazzoni, Davide Ceresoli, Guido L Chiarotti, Matteo Cococcioni, Ismaila Dabo, et al., *Journal of physics: Condensed matter* **21**(39), pp. 395502 (2009). 53, 78

[102] P Giannozzi, O Andreussi, T Brumme, O Bunau, M Buongiorno Nardelli, M Calandra, R Car, C Cavazzoni, D Ceresoli, M Cococcioni, N Colonna, I Carnimeo, A Dal Corso, S de Gironcoli, P Delugas, R A DiStasio, A Ferretti, A Floris, G Fratesi, G Fugallo, R Gebauer, U Gerstmann, F Giustino, T Gorni, J Jia, M Kawamura, H-Y Ko, A Kokalj, E Küçükbenli, M Lazzeri, M Marsili, N Marzari, F Mauri, N L Nguyen, H-V Nguyen, A Otero de-la Roza, L Paulatto, S Poncé, D Rocca, R Sabatini, B Santra, M Schlipf, A P Seitsonen, A Smogunov, I Timrov, T Thonhauser, P Umari, N Vast, X Wu, and S Baroni, "Advanced capabilities for materials modelling with quantum espresso", *Journal of Physics: Condensed Matter* **29**(46), pp. 465901 (2017). 53

[103] J Bardeen and WJPR Shockley, *Physical review* **80**(1), pp. 72 (1950). 54, 68, 79, 82

[104] F Aguilera-Granja, Rodrigo Humberto Aguilera-del Toro, and José Luis Morán-López, "A first principles systematic study of the structural, electronic, and magnetic properties of heusler x2mnz with x= fe, co, ni, cu, ru, rh, pd, ag, pt, au and z= al, si, ga, ge, in and sn", *Materials Research Express* **6**(10), pp. 106118 (2019). 56

[105] Ashutosh Giri, Brian F Donovan, and Patrick E Hopkins, "Localization of vibrational modes leads to reduced thermal conductivity of amorphous heterostructures", *Physical Review Materials* **2**(5), pp. 056002 (2018). 62

[106] DT Morelli, JP Heremans, and GA Slack, "Estimation of the isotope effect on the lattice thermal conductivity of group iv and group iii-v semiconductors", *Physical Review B* **66**(19), pp. 195304 (2002). 64, 88

[107] Jesús Carrete, Wu Li, Natalio Mingo, Shidong Wang, and Stefano Curtarolo, "Finding unprecedentedly low-thermal-conductivity half-heusler semiconductors via high-throughput materials modeling", *Physical Review X* **4**(1), pp. 011019 (2014). 66, 103

[108] Shashwat Anand, Max Wood, Yi Xia, Chris Wolverton, and G Jeffrey Snyder, "Double half-heuslers", *Joule* **3**(5), pp. 1226–1238 (2019). 66, 76

[109] Voicu Popescu and Alex Zunger, "Extracting e versus k effective band structure from supercell calculations on alloys and impurities", *Physical Review B—Condensed Matter and Materials Physics* **85**(8), pp. 085201 (2012). 67, 127

[110] S Sakurada and NJAPL Shutoh, "Effect of ti substitution on the thermoelectric properties of (zr, hf) nisn half-heusler compounds", *Applied Physics Letters* **86**(8) (2005).

[111] Genadi Antonov Naydenov, Philip James Hasnip, VK Lazarov, and MIJ Probert, *Journal of physics: Materials* **2**(3), pp. 035002 (2019). 75

[112] Hangtian Zhu, Ran He, Jun Mao, Qing Zhu, Chunhua Li, Jifeng Sun, Wuyang Ren, Yumei Wang, Zihang Liu, Zhongjia Tang, et al., "Discovery of zrcobi based half heuslers with high thermoelectric conversion efficiency", *Nature Communications* **9**(1), pp. 2497 (2018). 75

[113] Y Xiao and LD Zhao, "Charge and phonon transport in pbte-based thermoelectric materials. npj quantum mater. 2018, 3, 55". 75

[114] Raza Moshwan, Lei Yang, Jin Zou, and Zhi-Gang Chen, "Eco-friendly snte thermoelectric materials: progress and future challenges", *Advanced Functional Materials* **27**(43), pp. 1703278 (2017). 75

[115] Gus LW Hart and Rodney W Forcade, "Algorithm for generating derivative structures", *Physical Review B—Condensed Matter and Materials Physics* **77**(22), pp. 224115 (2008). 76

[116] Bhawna Sahni and Aftab Alam, "Double half-heusler alloys x 2 ni 2 insb (x= zr, hf) with promising thermoelectric performance: The role of varying structural phases", *Physical Review Applied* **22**(3), pp. 034034 (2024). 76

[117] Job W Wafula, John W Makokha, and George S Manyali, "First-principles calculations to investigate structural, elastic, electronic and thermodynamic properties of nbcosn and vrhsn half-heusler compounds", *Results in Physics* **43**, pp. 106132 (2022). 76

[118] Ruijuan Yan, Ruiwen Xie, Wenjie Xie, Chen Shen, Wei Li, Benjamin Balke, Songhak Yoon, Hongbin Zhang, and Anke Weidenkaff, "Effects of doping ni on the microstructures and thermoelectric properties of co-excessive nbcosn half-heusler

compounds", *ACS Applied Materials & Interfaces* **13**(29), pp. 34533–34542 (2021). 76

[119] Xianfeng Ye, Zhenzhen Feng, Yazhu Xu, Miaomiao Jian, Yuli Yan, Yongsheng Zhang, and Gaofeng Zhao, "A theoretical study on the thermal conductivity and thermoelectric properties of conbsi and conbsn", *The Journal of Physical Chemistry C* **125**(18), pp. 10068–10076 (2021). 76

[120] Paolo Giannozzi, Oliviero Andreussi, Thomas Brumme, Oana Bunau, M Buongiorno Nardelli, Matteo Calandra, Roberto Car, Carlo Cavazzoni, Davide Ceresoli, Matteo Cococcioni, et al., "Advanced capabilities for materials modelling with quantum espresso", *Journal of physics: Condensed matter* **29**(46), pp. 465901 (2017). 78

[121] Harvey Brooks, "Scattering by ionized impurities in semiconductors", In *Physical Review* volume 83 , pp. 879–879. AMERICAN PHYSICAL SOC ONE PHYSICS ELLIPSE, COLLEGE PK, MD 20740-3844 USA (1951). 94

[122] E Conwell and VF Weisskopf, "Theory of impurity scattering in semiconductors", *Physical review* **77**(3), pp. 388 (1950). 94

[123] Cui Yu, Tie-Jun Zhu, Kai Xiao, Jun-Jie Shen, Sheng-Hui Yang, and Xin-Bing Zhao, "Reduced grain size and improved thermoelectric properties of melt spun (hf, zr) nisn half-heusler alloys", *Journal of electronic materials* **39**(9), pp. 2008–2012 (2010). 94

[124] Luc Andrea, Gilles Hug, and Laurent Chaput, "Ab initio phonon properties of half-heusler nitisn, nizrsn and nihfsn", *Journal of Physics: Condensed Matter* **27**(42), pp. 425401 (2015). 103

[125] Simen NH Eliassen, Ankita Katre, Georg KH Madsen, Clas Persson, Ole Martin Løvvik, and Kristian Berland, "Lattice thermal conductivity of ti x zr y hf 1- x- y nisn half-heusler alloys calculated from first principles: Key role of nature of phonon modes", *Physical Review B* **95**(4), pp. 045202 (2017). 103

[126] Yintu Liu, Hanhui Xie, Chenguang Fu, G Jeffrey Snyder, Xinbing Zhao, and Tiejun Zhu, "Demonstration of a phonon-glass electron-crystal strategy in (hf, zr) nisn half-heusler thermoelectric materials by alloying", *Journal of Materials Chemistry A* **3**(45), pp. 22716–22722 (2015). 103

[127] Takeyuki Sekimoto, Ken Kurosaki, Hiroaki Muta, and Shinsuke Yamanaka, "Thermoelectric and thermophysical properties of ticosb-zrcosb-hfcosb pseudo ternary system prepared by spark plasma sintering", *Materials transactions* **47**(6), pp. 1445–1448 (2006). 103

[128] Teng Fang, Xinbing Zhao, and Tiejun Zhu, "Band structures and transport properties of high-performance half-heusler thermoelectric materials by first principles", *Materials* **11**(5), pp. 847 (2018). 103, 128

[129] Han-Hui Xie, Jian-Li Mi, Li-Peng Hu, Nina Lock, Mogens Chirstensen, Chen-Guang Fu, Bo Brummerstedt Iversen, Xin-Bing Zhao, and Tie-Jun Zhu, "Interrelation between atomic switching disorder and thermoelectric properties of zrnisn half-heusler compounds", *CrystEngComm* **14**(13), pp. 4467–4471 (2012). 103

[130] Dat T Do, S D Mahanti, and Jiji J Pulikkoti, "Electronic structure of zr–ni–sn systems: role of clustering and nanostructures in half-heusler and heusler limits", *Journal of Physics: Condensed Matter* **26**(27), pp. 275501 (2014). 103

[131] Thomas A Manz and Nidia Gabaldon Limas, "Introducing ddec6 atomic population analysis: part 1. charge partitioning theory and methodology", *RSC advances* **6**(53), pp. 47771–47801 (2016). 116

[132] Krzysztof Gałazka, Sascha Populoh, Leyre Sagarna, Lassi Karvonen, Wenjie Xie, Alessandra Beni, Patrik Schmutz, Jürg Hulliger, and Anke Weidenkaff, "Phase formation, stability, and oxidation in (ti, zr, hf) nisn half-heusler compounds", *physica status solidi (a)* **211**(6), pp. 1259–1266 (2014). 121